

Current work on novel steels at the Max-Planck-Institut

D. Raabe, D. Ponge, P. Choi, S. Sandlöbes, J. Millan

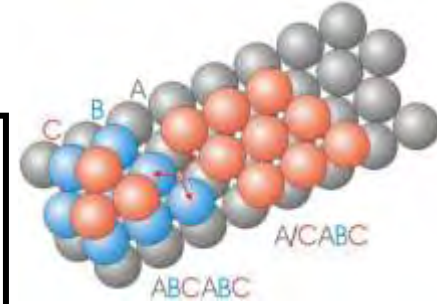
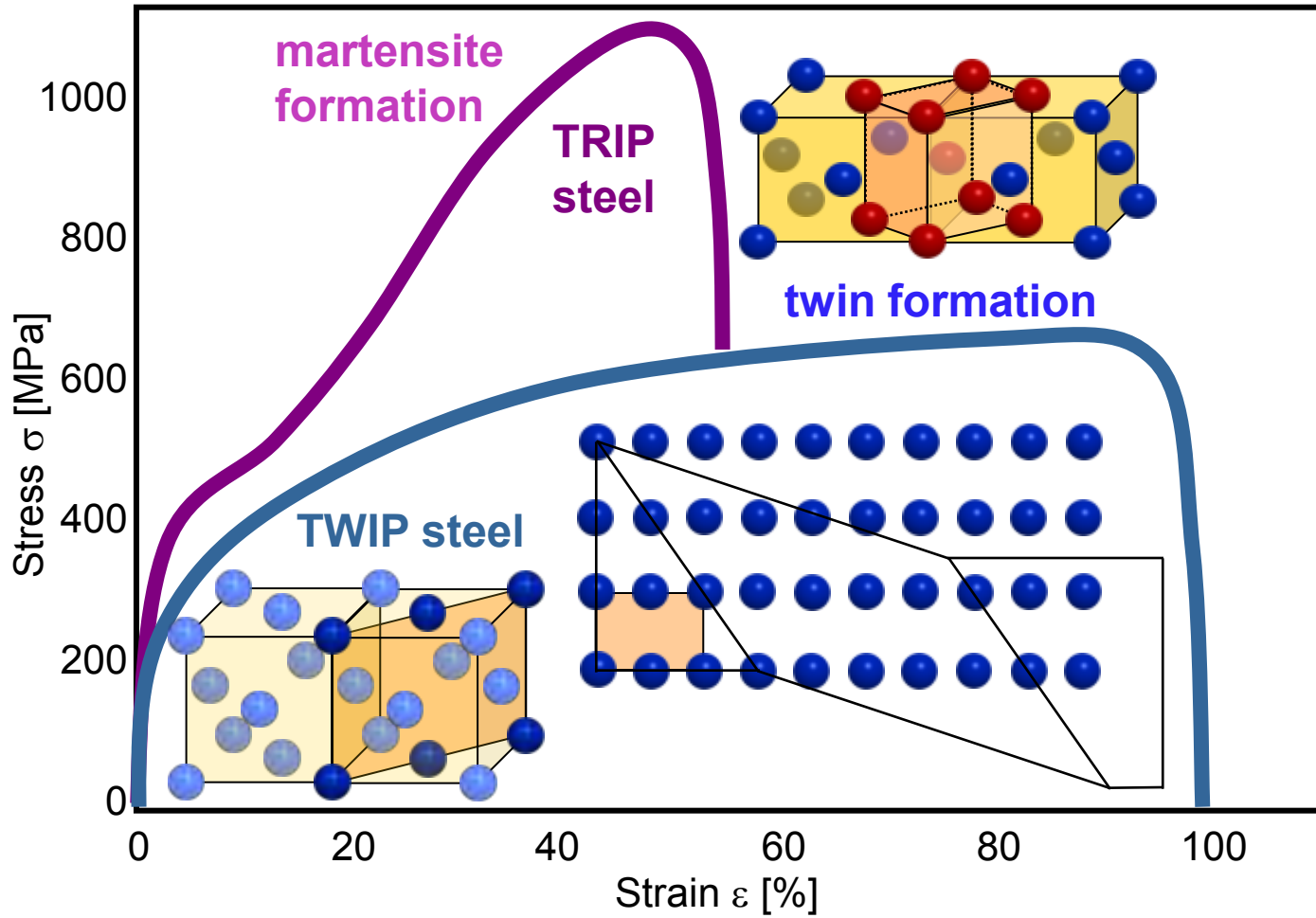


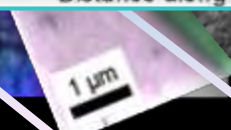
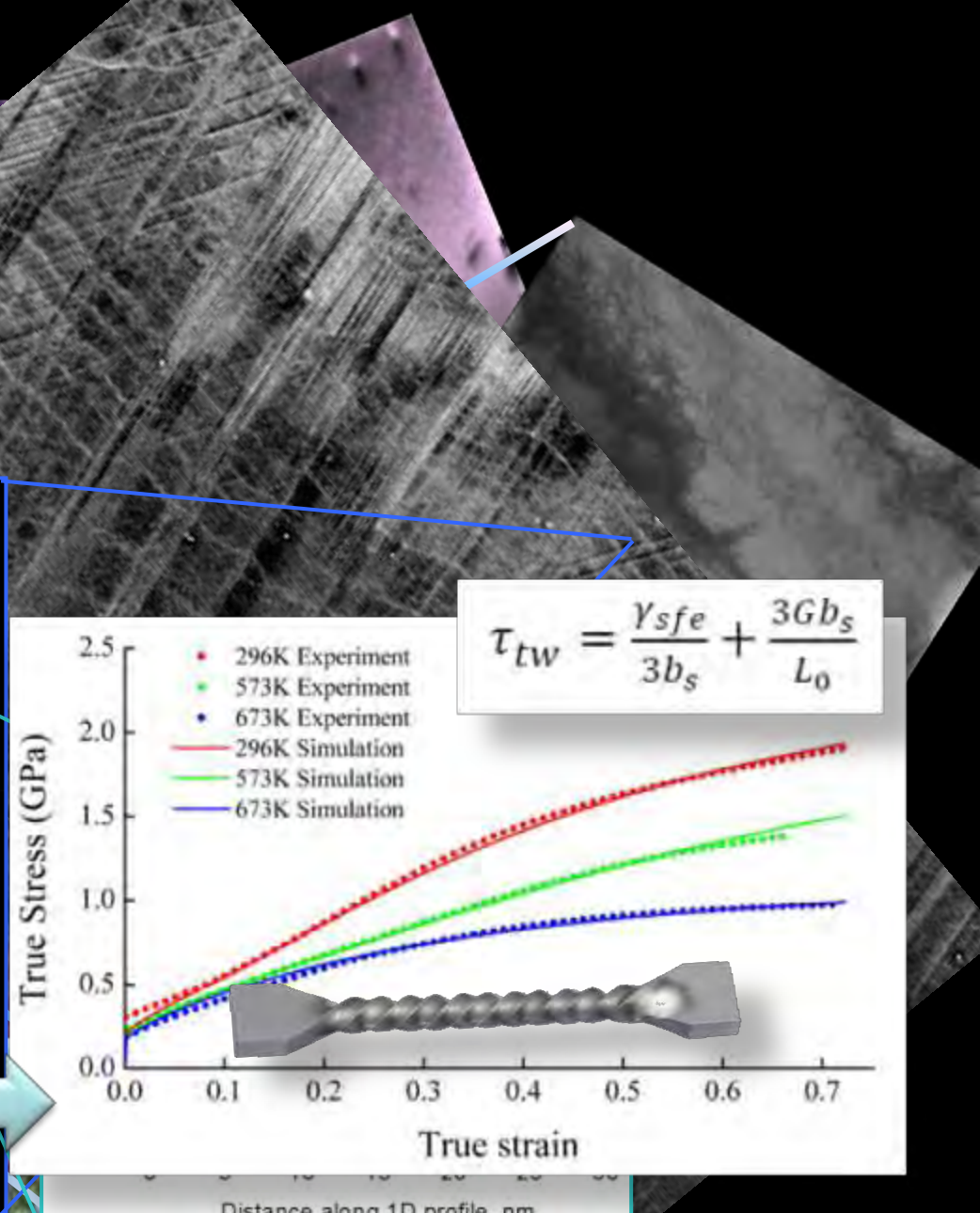
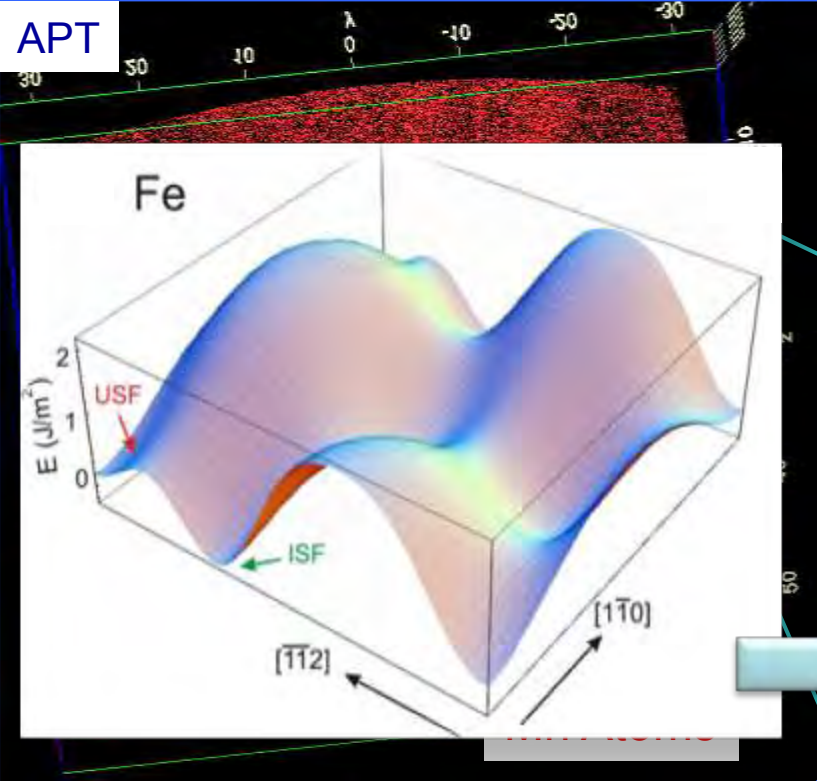
Max-Planck-Institut
für Eisenforschung GmbH
Düsseldorf, Germany

WWW.MPIE.DE
d.raabe@mpie.de

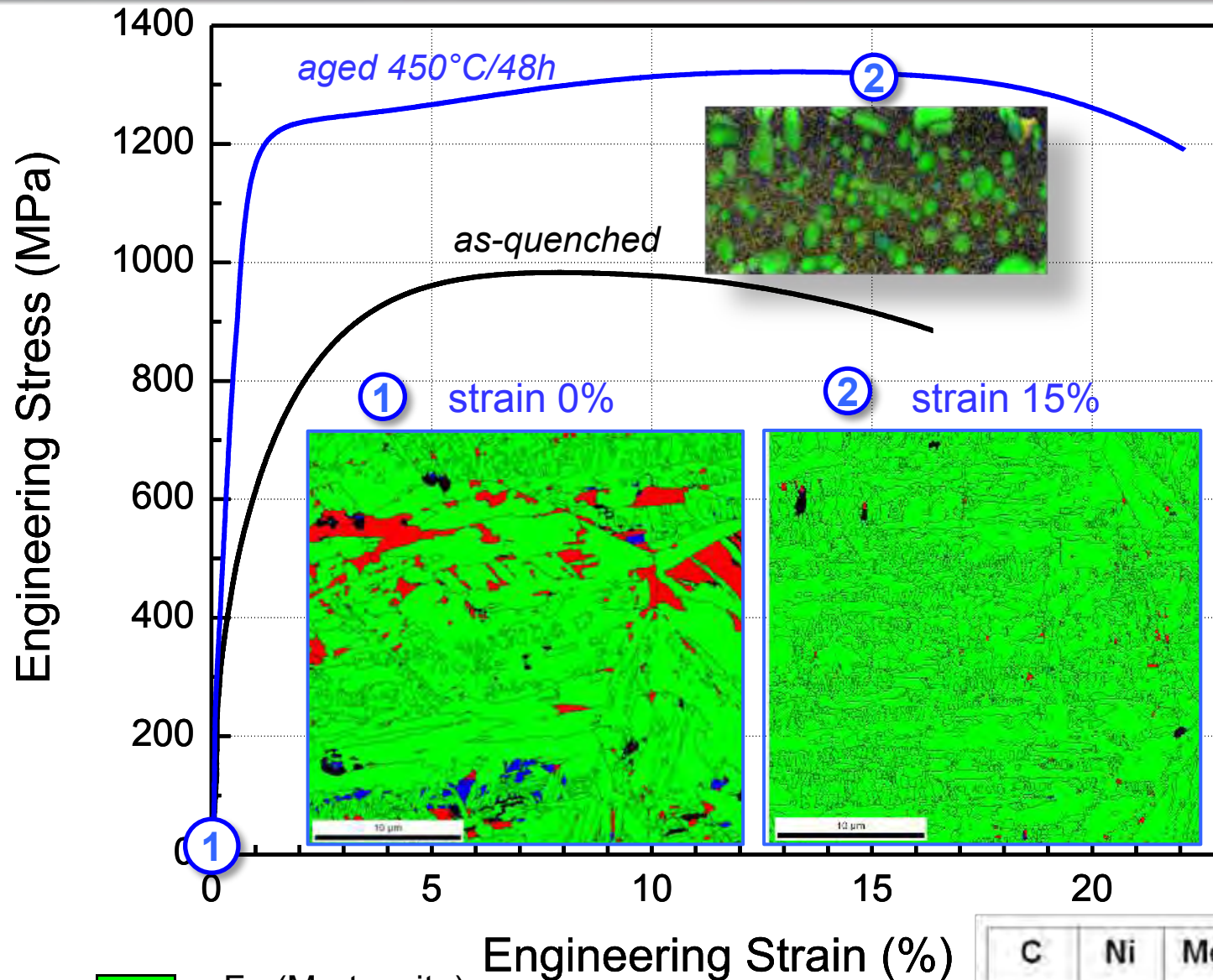


- **Atomistic design of steels**
- **Ultra-high strength Mn steels**
- **Weight-reduced TRIPLEX and SBIP steels**
- **Lean maraging steels**
- **Lean steels with nano-carbides**
- **Maraging TRIP steels**
- **Middle Mn-Steels**
- **Towards the limits of strength: pearlite**
- **Steels for electromobility – high strength Fe-3%Si steels**
- **Amorphous steels – FeSiBCuNb steels**
- **Turbine alloys**
- **Superplastic steels**
- **Shape memory steels**
- **UFG dual phase steels and DP-QP steels**
- **Austenite reversion steels**
- **Rapid steel design**



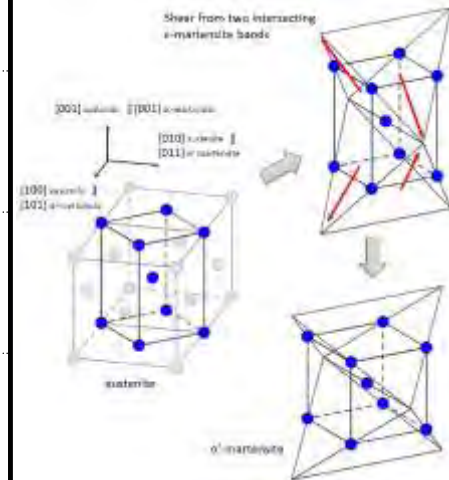


Effect of aging on ductility



Precipitation hardening

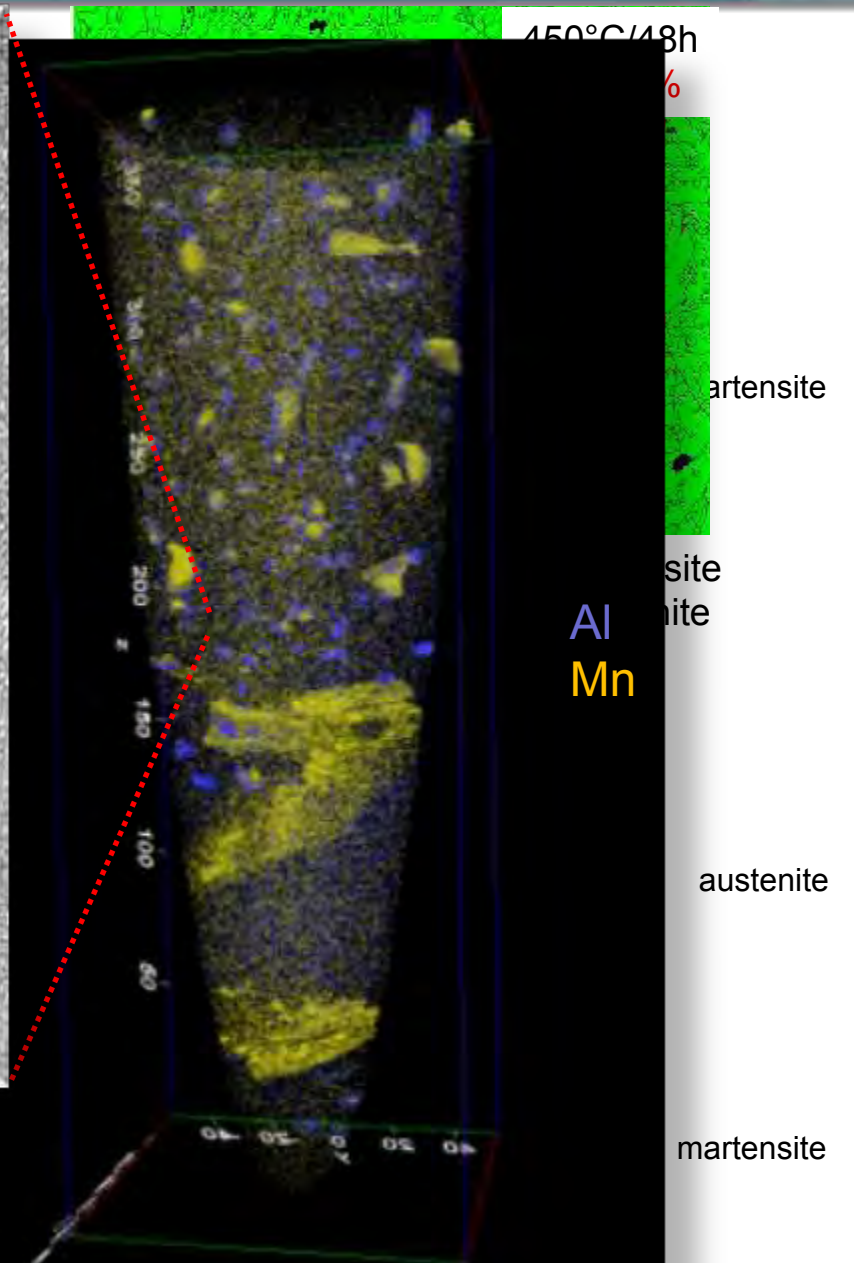
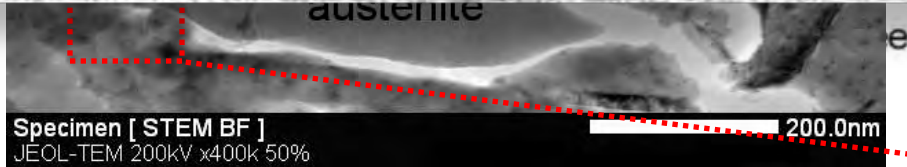
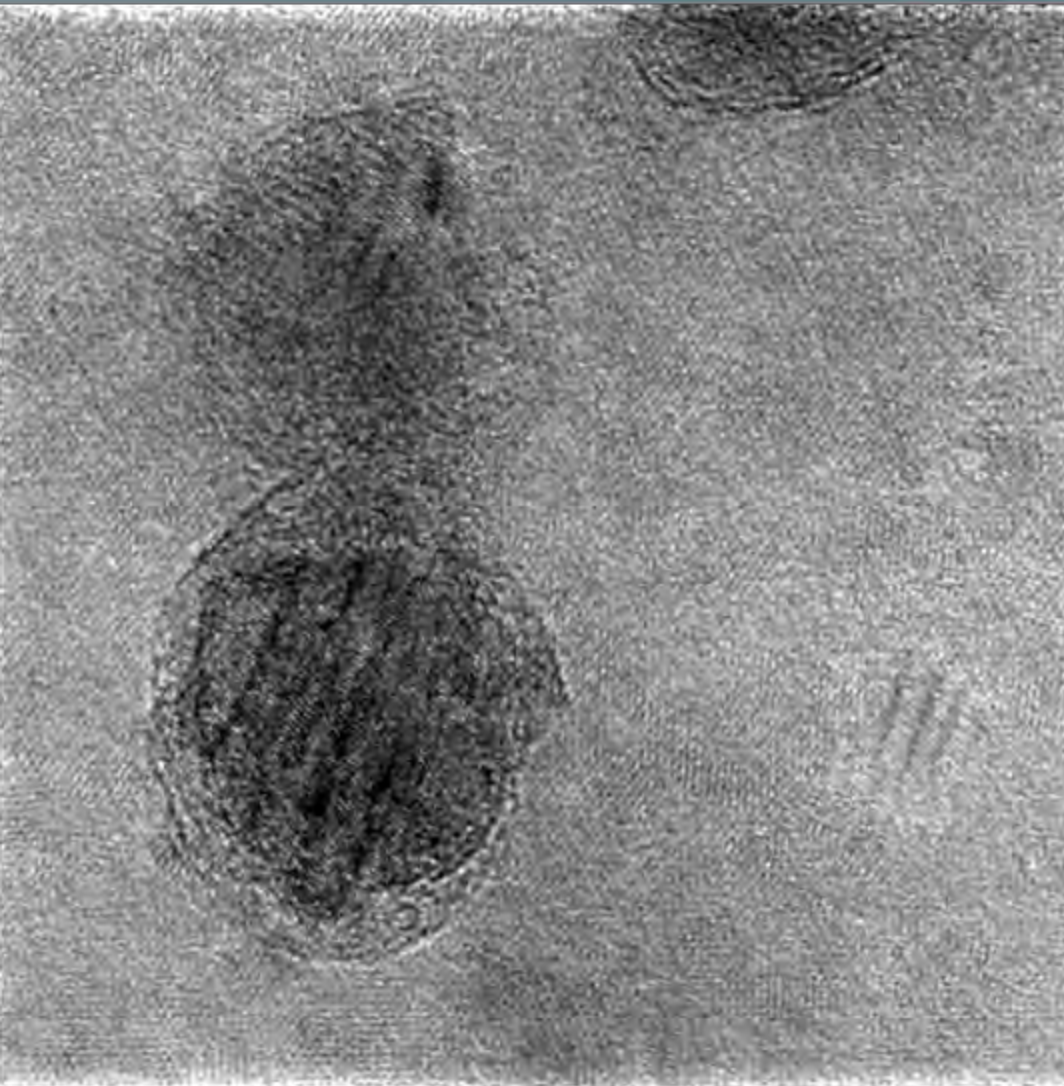
increase of austenite fraction during aging

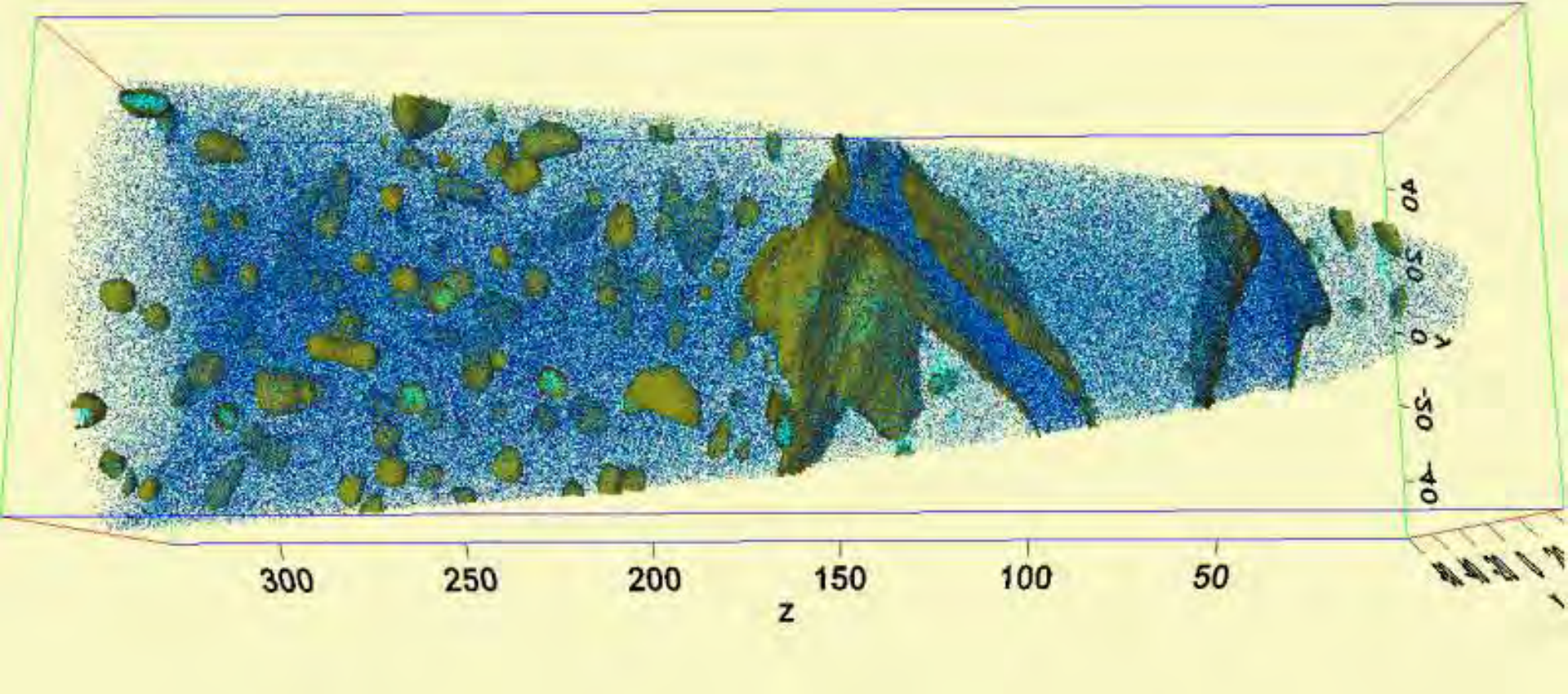


■ α -Fe (Martensite)
■ γ -Fe (Austenite), vol. fraction 15-20%

C	Ni	Mo	Ti	Al	Mn	Fe
0.01	2.0	1.0	1.0	0.15	12	bal.

Hierarchy of maraging TRIP / TWIP steels





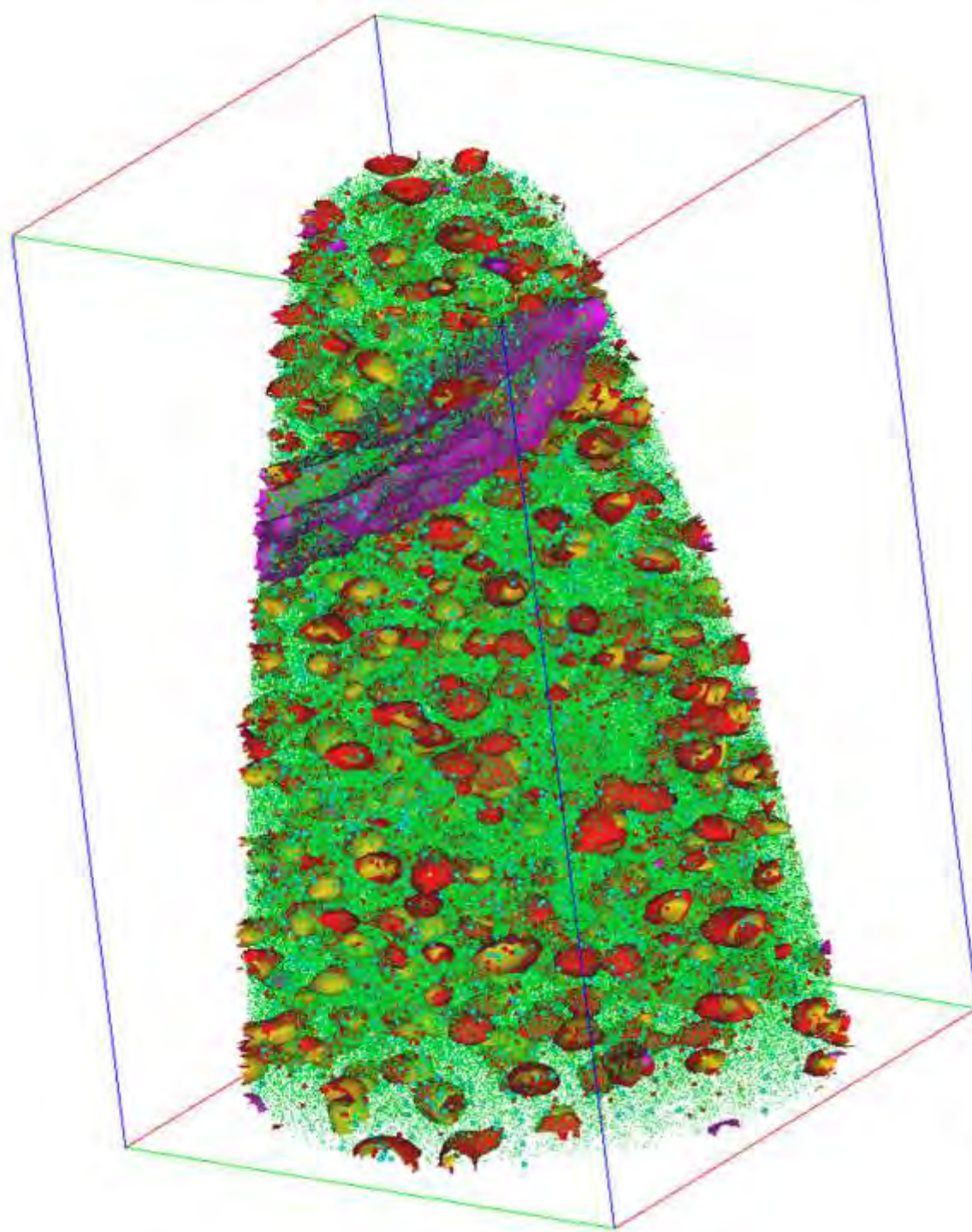
Mn atoms

Ni atoms

Mn iso-concentration: 18 at.%

C	Ni	Mo	Ti	Al	Mn	Fe
0.01	2.0	1.0	1.0	0.15	12	bal.

70 million ions
Laser mode
(0.4nJ, 54K)



● Ni ● Mn
● Al ● Fe

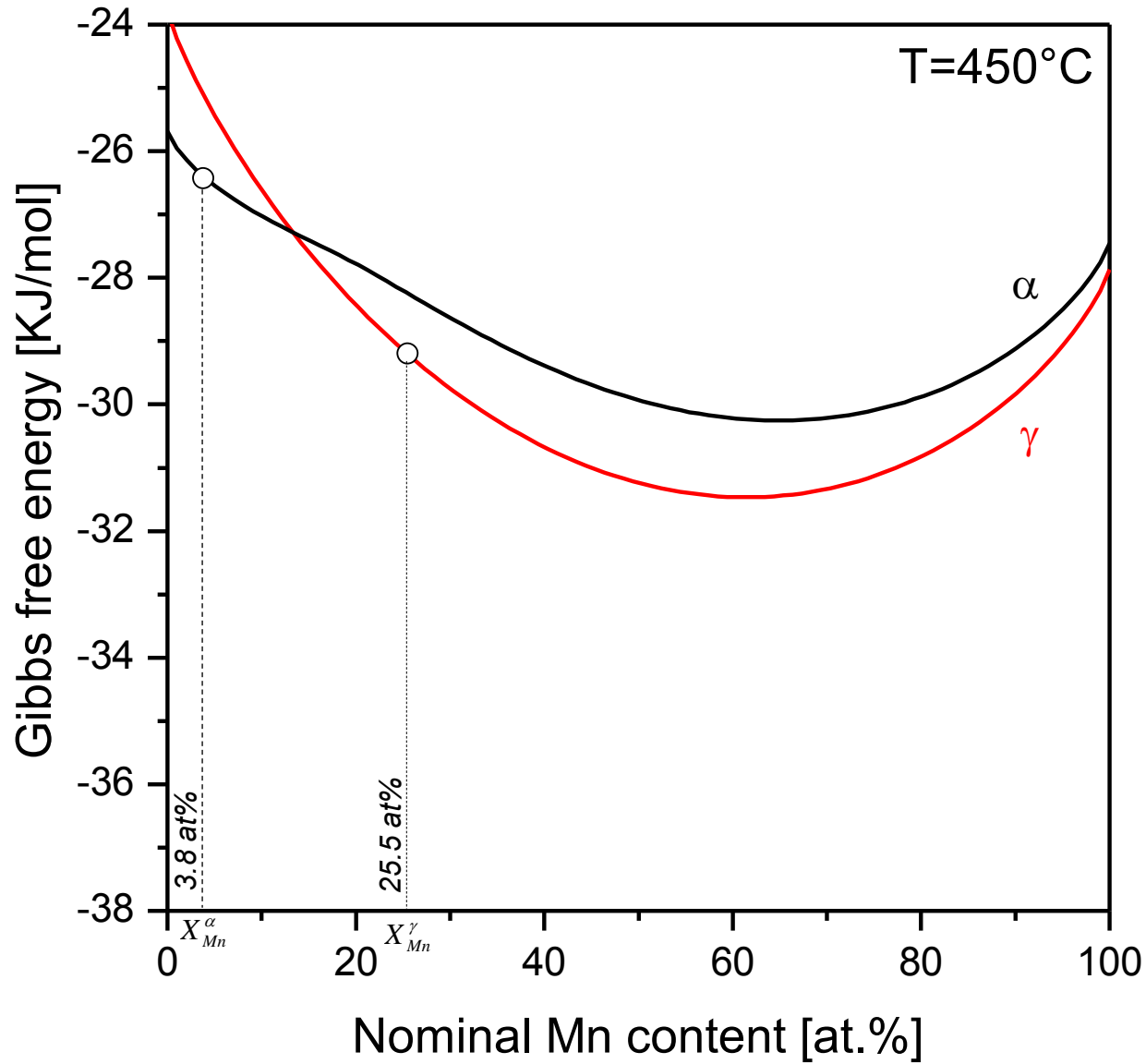
■ Mn surface (16at.%)

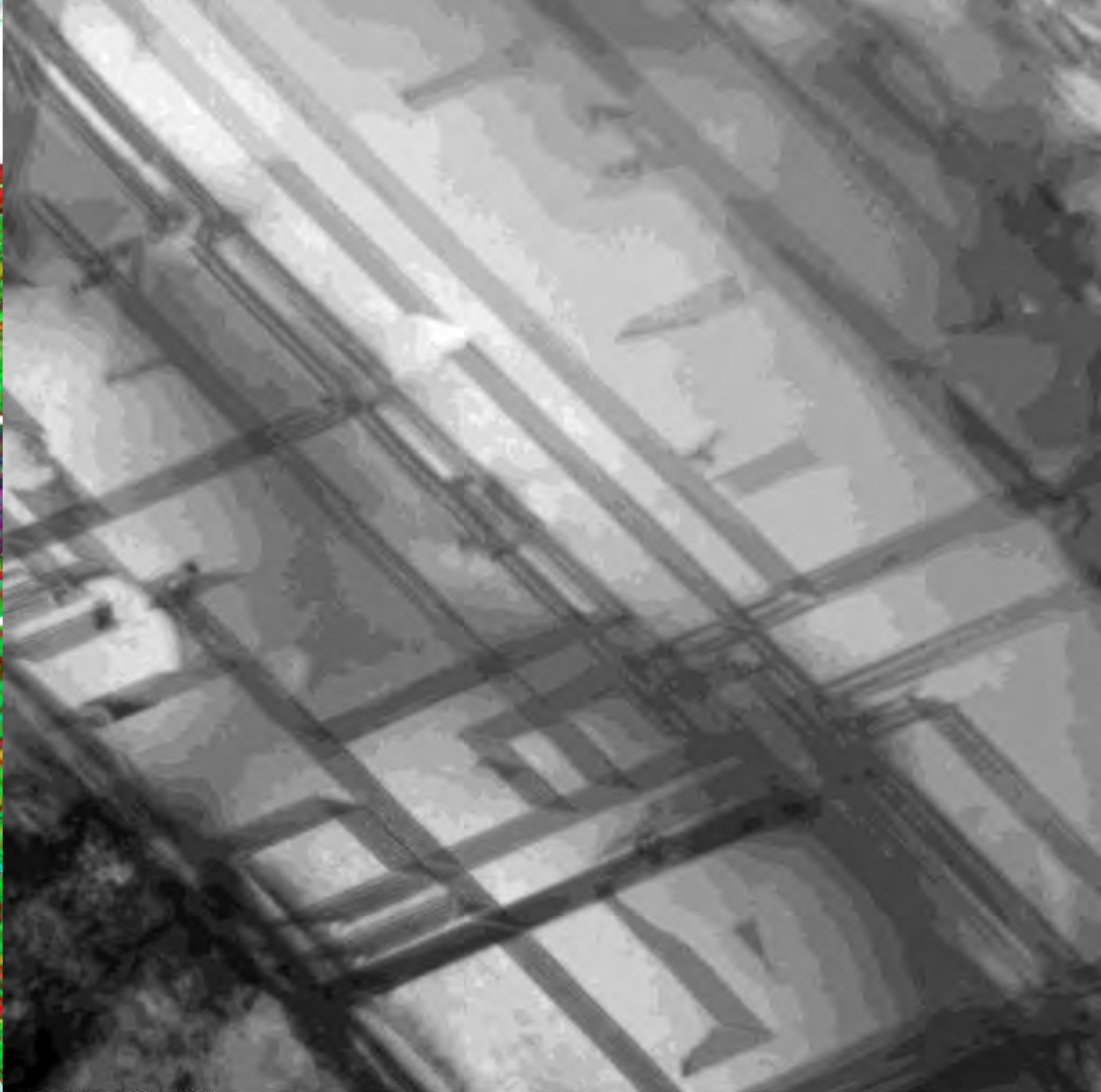
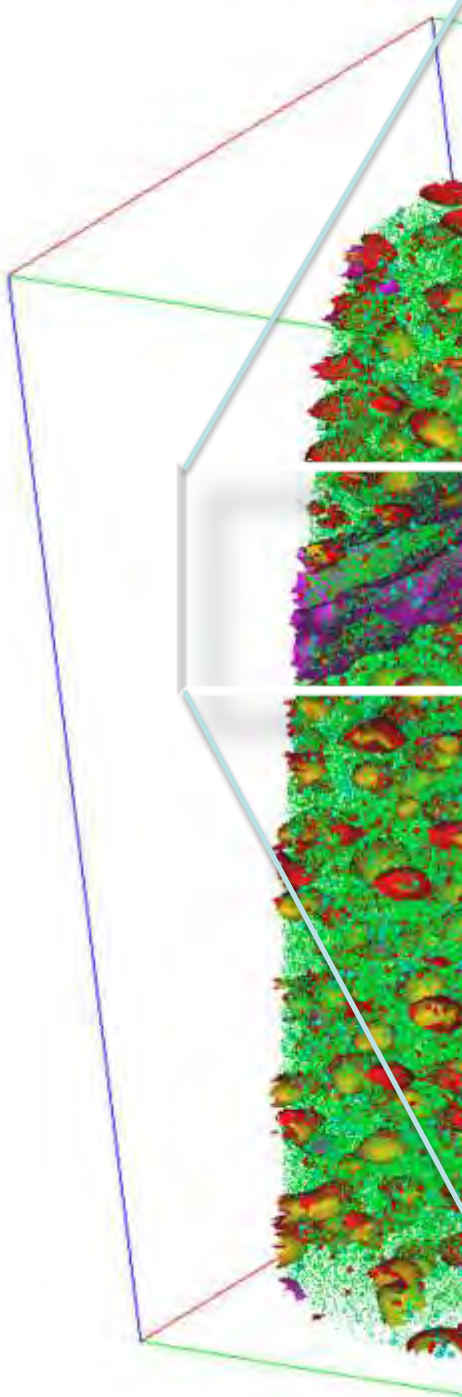
■ Ni surface (6 at.%)

■ Al surface (6 at.%)

10 nm

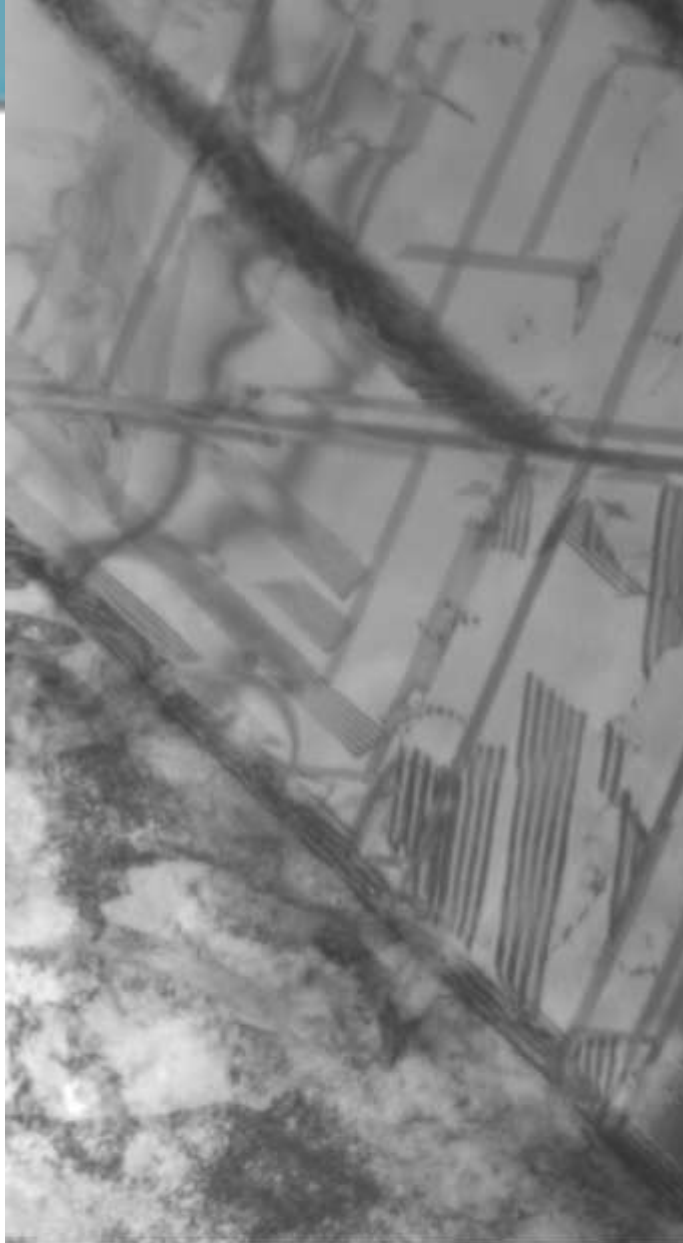






PR.proben003.tif
PR13 65h@450 C
stacking faults
Print Mag: 49500x @ 100 mm
TEM Mode: Imaging

100 nm
HV=200,0kV
Direct Mag: 44000x
X:-107.789 Y: 194.272
MPI fr Eisenforschung - CM20

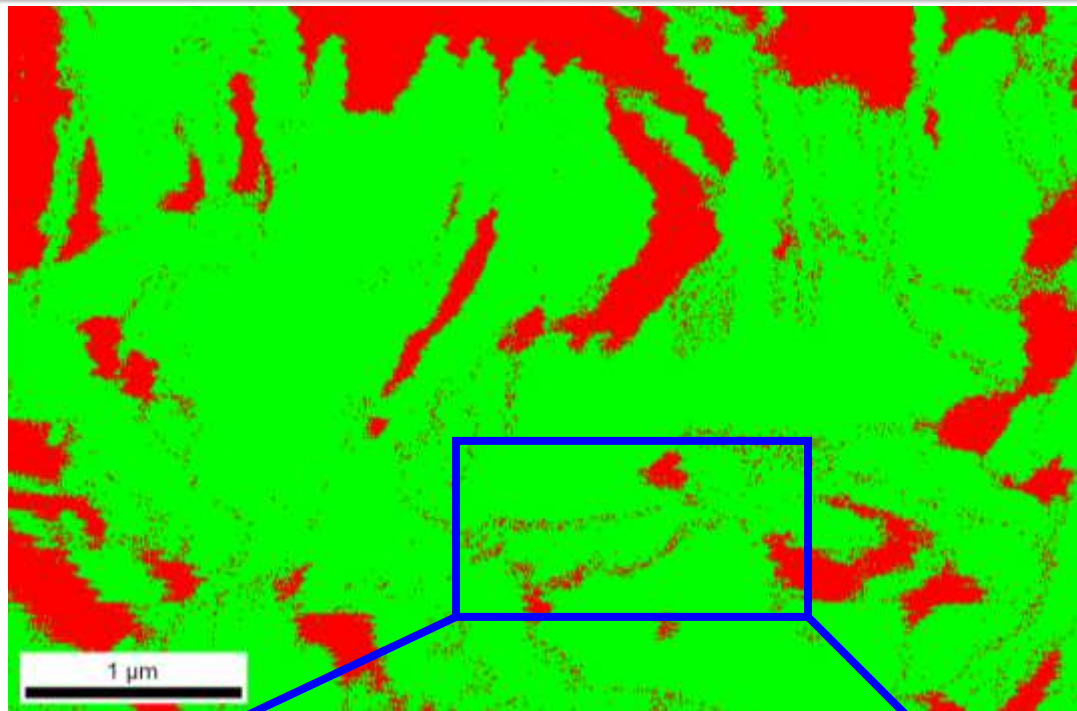


PR_proben031.tif
PR13 65h@450 C
SF 17,5kx BF
Print Mag: 19700x @ 100 mm
TEM Mode: Imaging



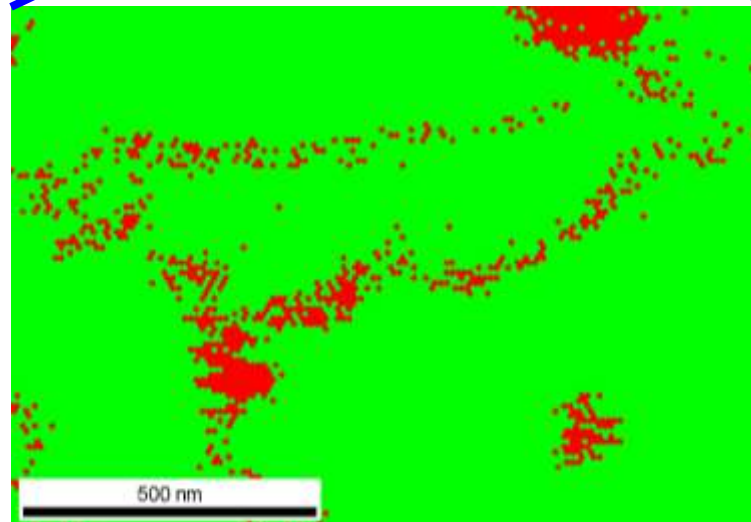
PR_proben032.tif
PR13 65h@450 C
SF 24,5kx BF
Print Mag: 27600x @ 100 mm
TEM Mode: Imaging

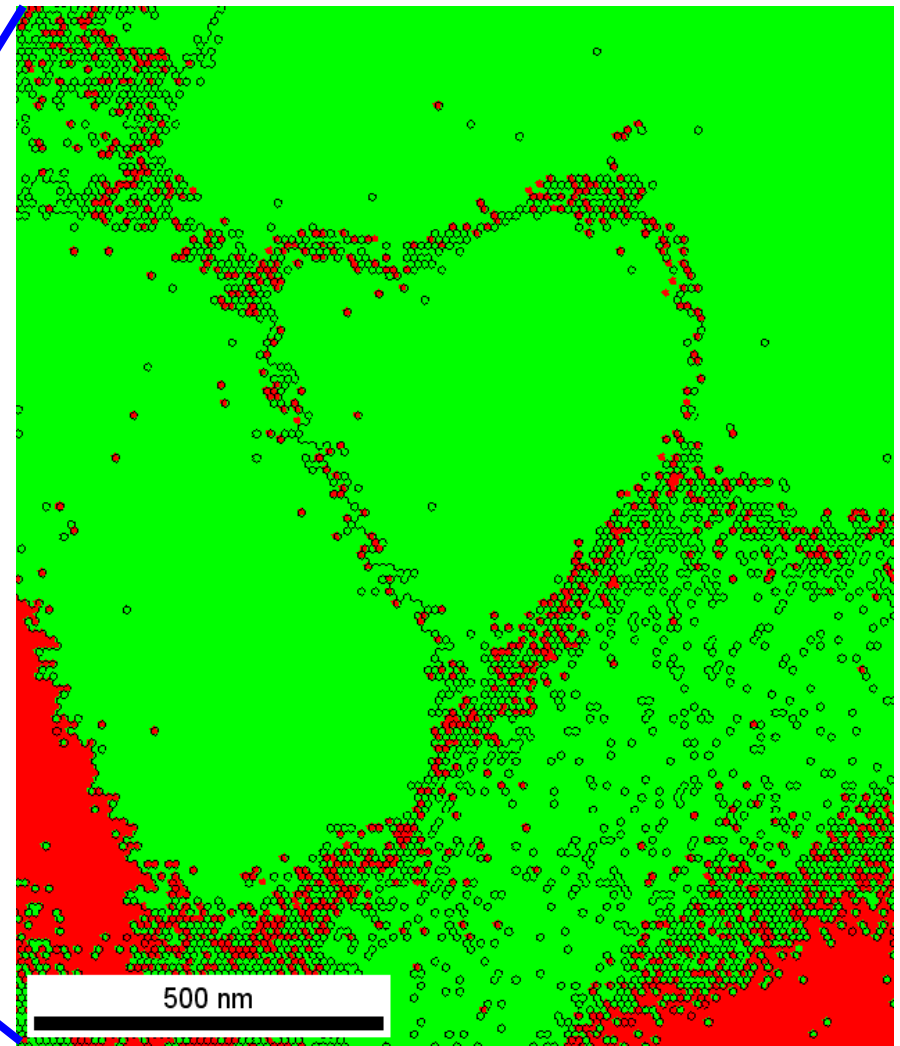
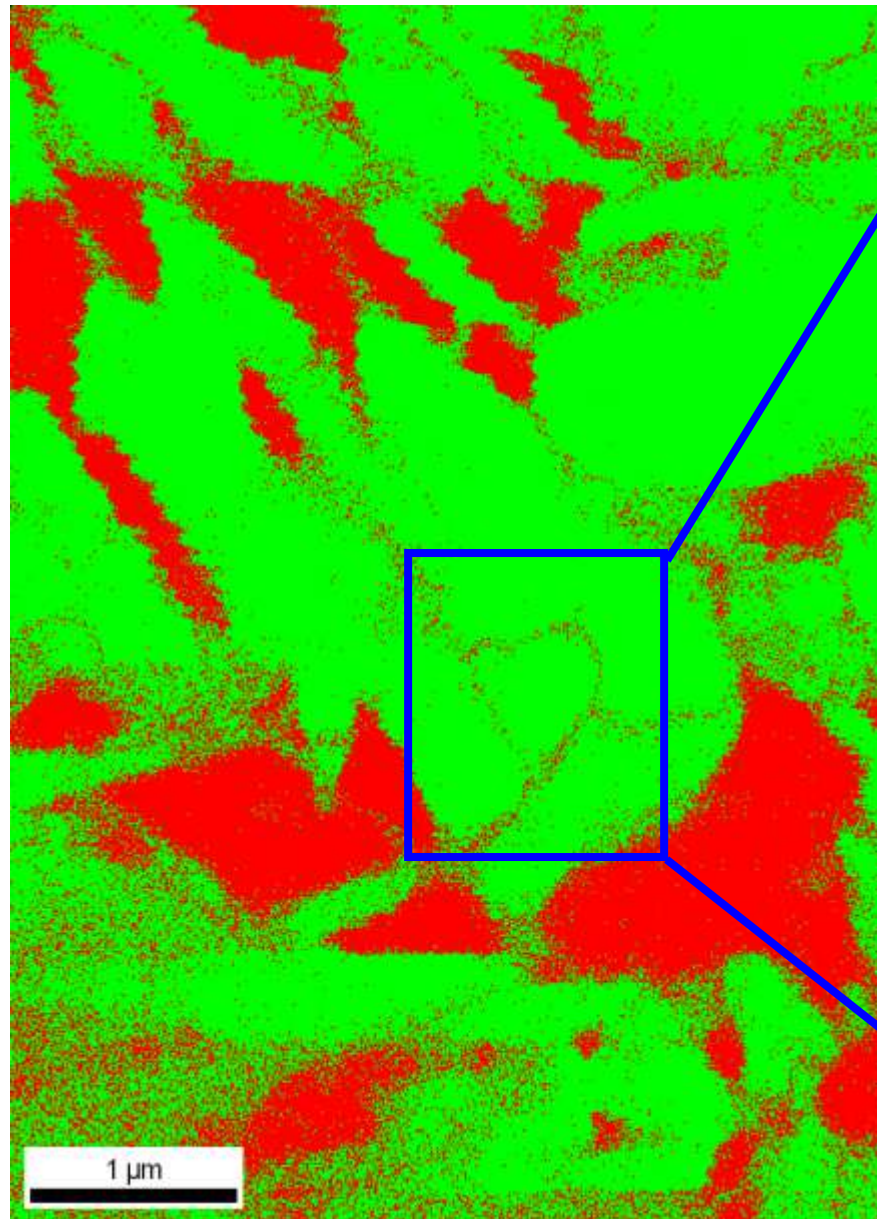
500 nm
HV=200,0kV
Direct Mag: 24500x
X:-76.673 Y: 166.535
MPI fr Eisenforschung - CM20



Phase

	Iron - Gamma
	Iron - Alpha



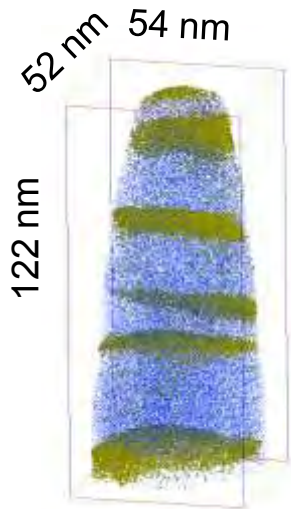


Phase

	Iron - Gamma
	Iron - Alpha



- Fe (2% displayed)
- C (20% displayed)



$\epsilon = 2$

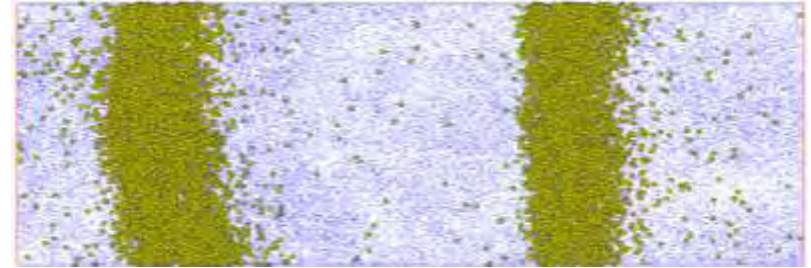


$\epsilon = 5$

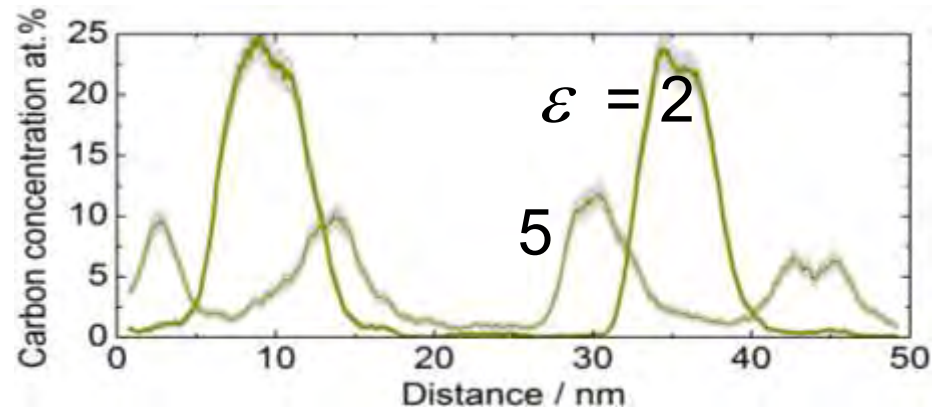
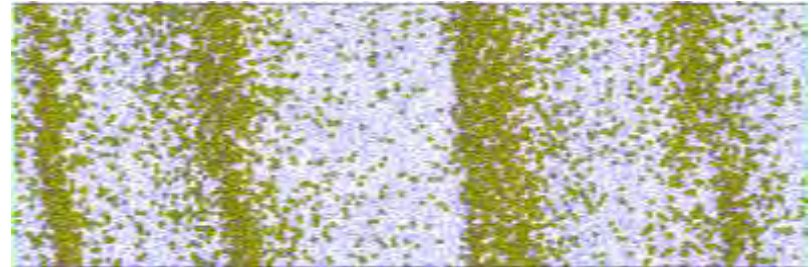
C (100% displayed)

Fe (50% displayed)

$\epsilon = 2$



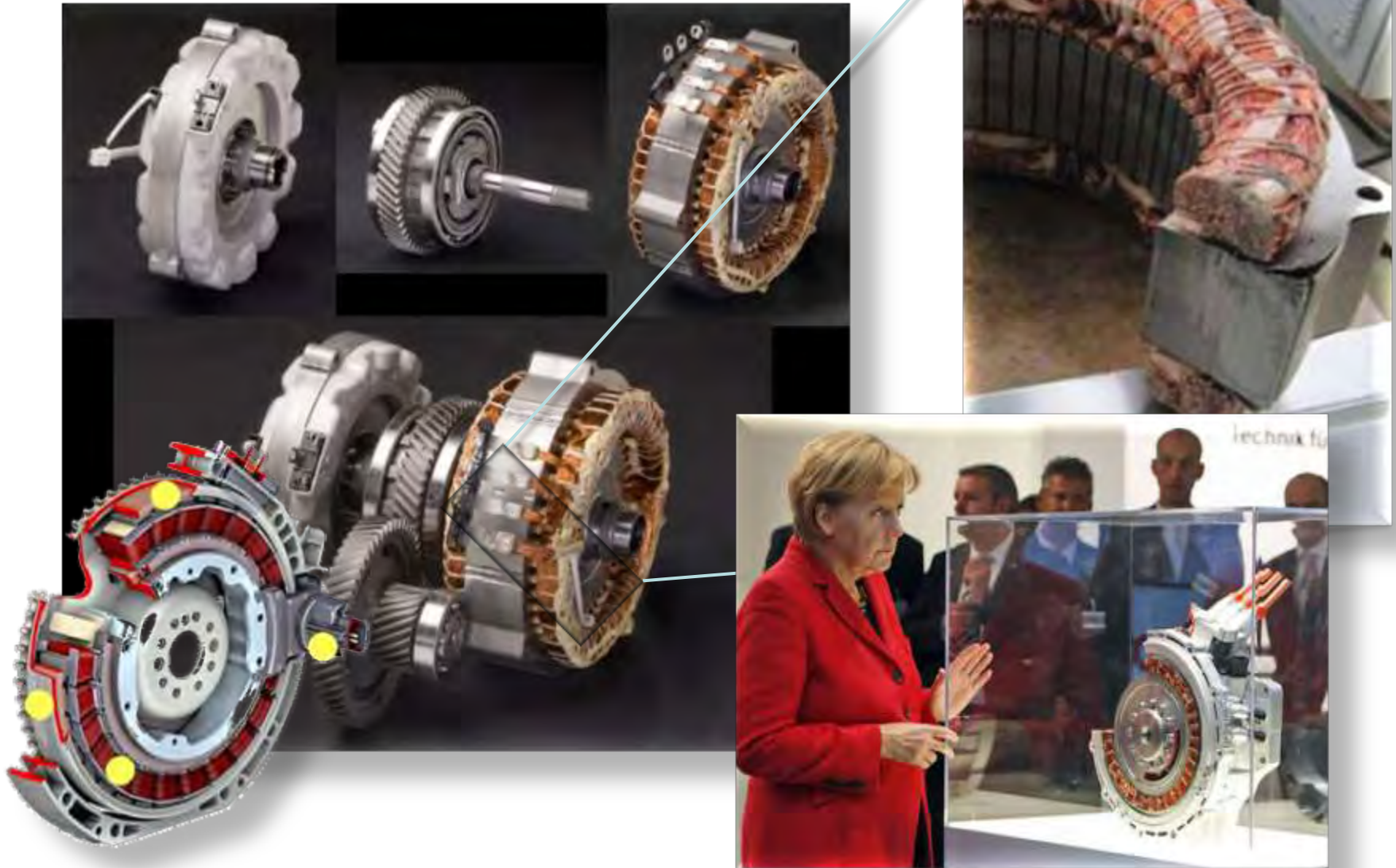
$\epsilon = 5$

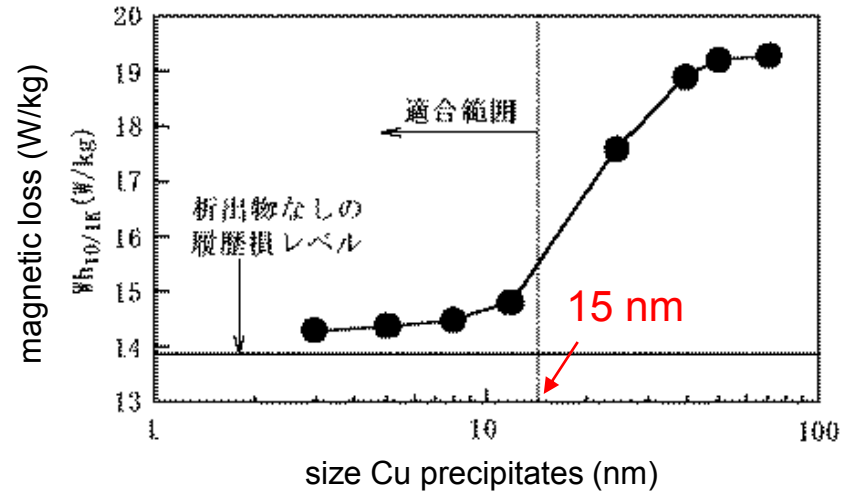


$\epsilon = 2$

5

25 kg (engine) + 12 kg (generator) x 43 Mio cars





{JP 2004 339603}

nanoparticles too small for Bloch-wall interaction but effective as dislocation obstacles

mechanically very strong soft magnets for motors

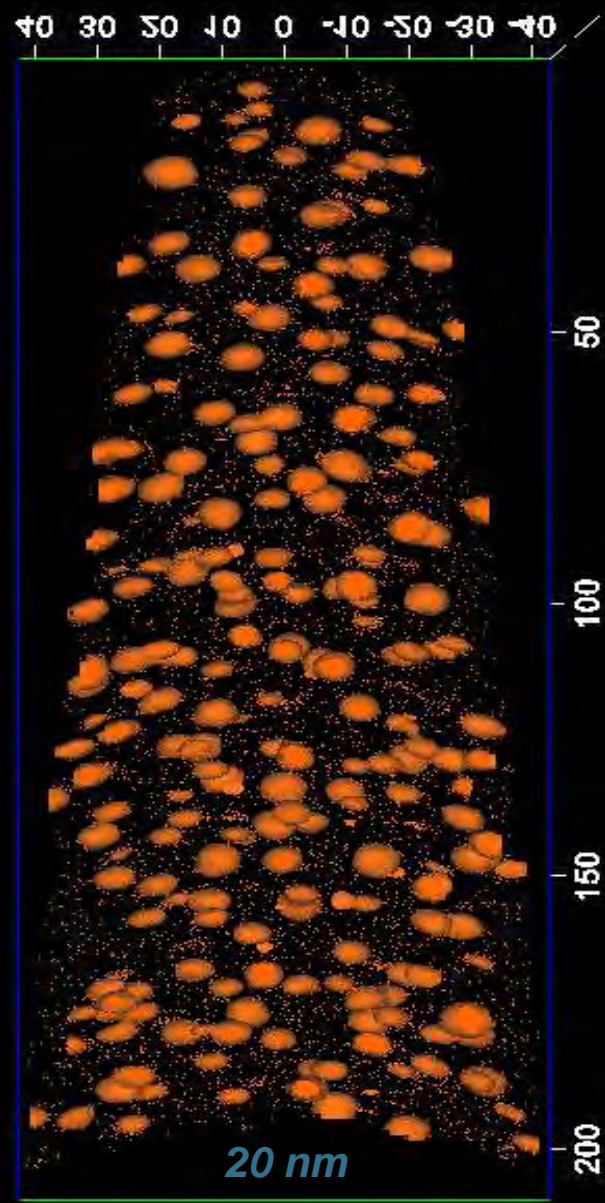
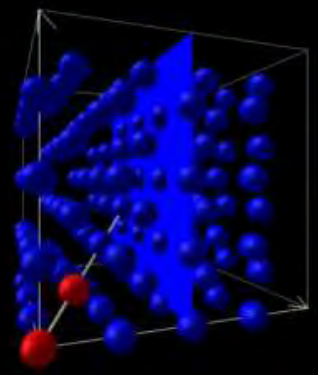
Steels for electromobility: precipitates vs. Bloch walls



Cu 2 wt.%

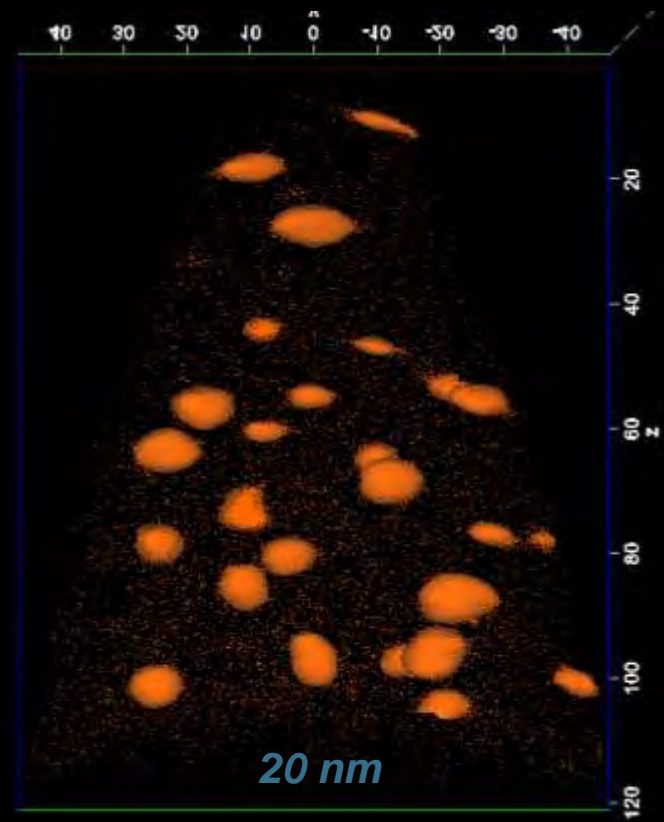
450°C aging

Iso-concentration surfaces at Cu 11 at.%



120 min

6000 min



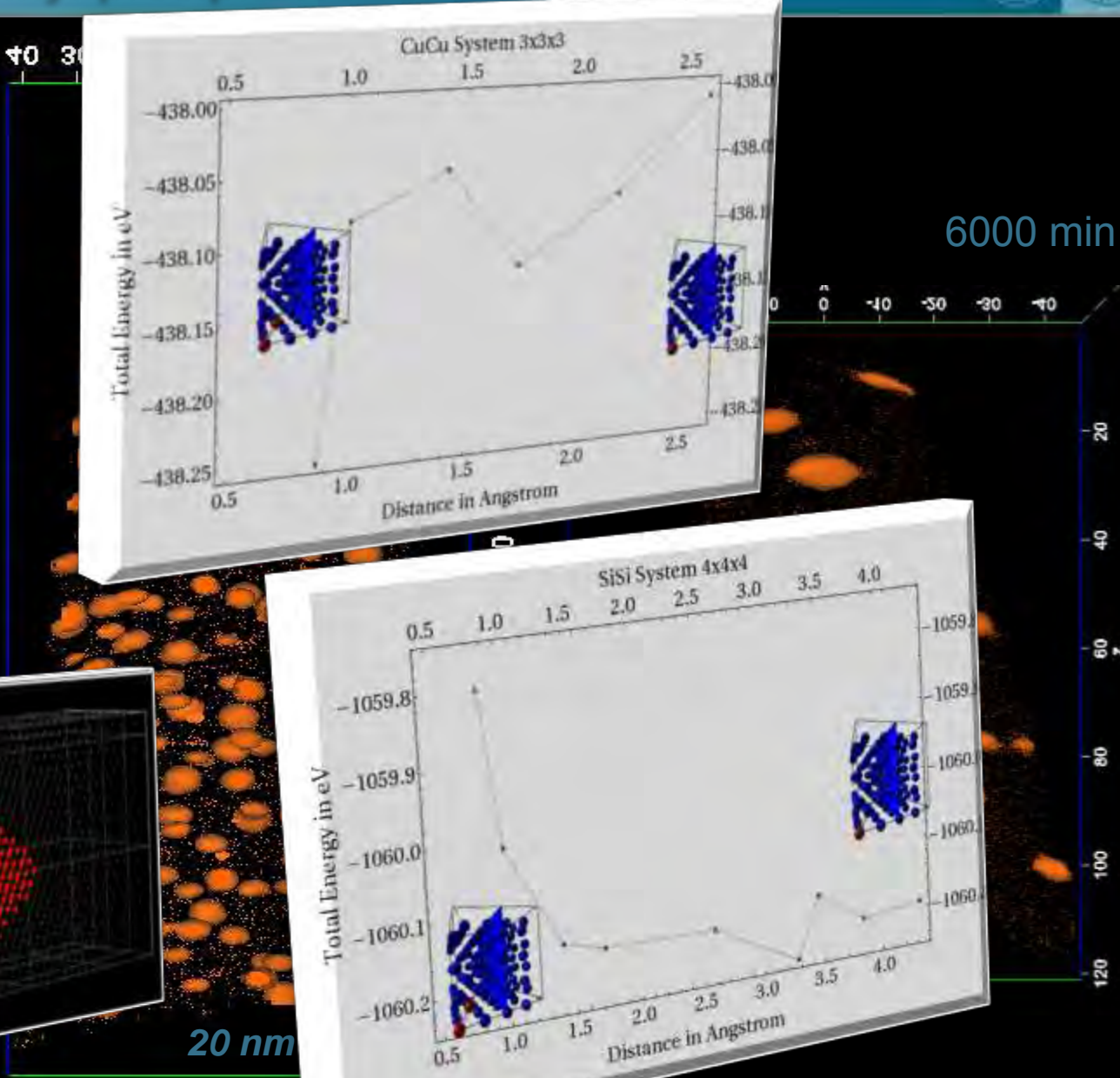
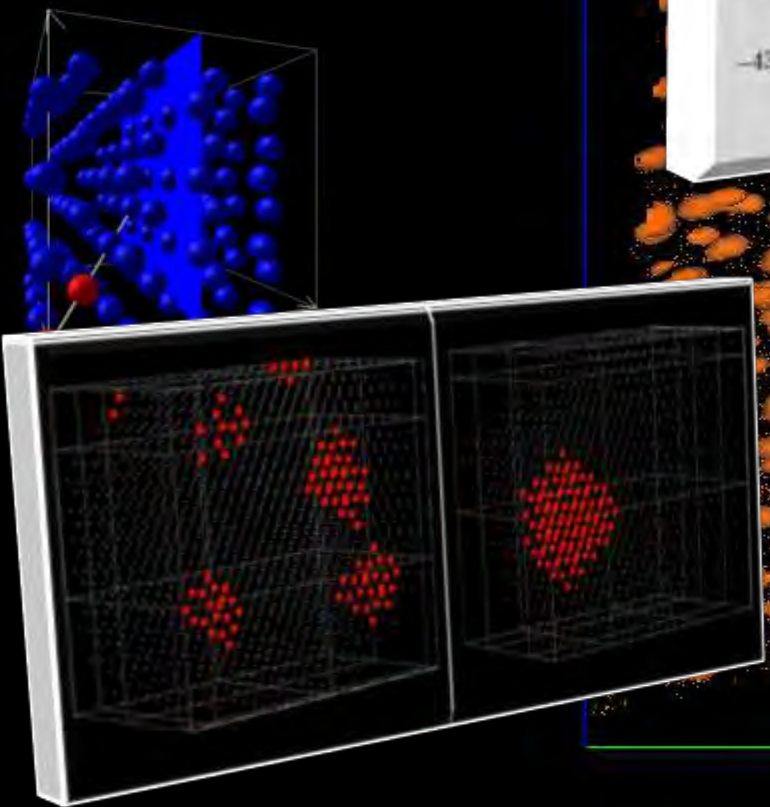
Steels for electromobility: precipitates vs. Bloch walls



Cu 2 wt.%

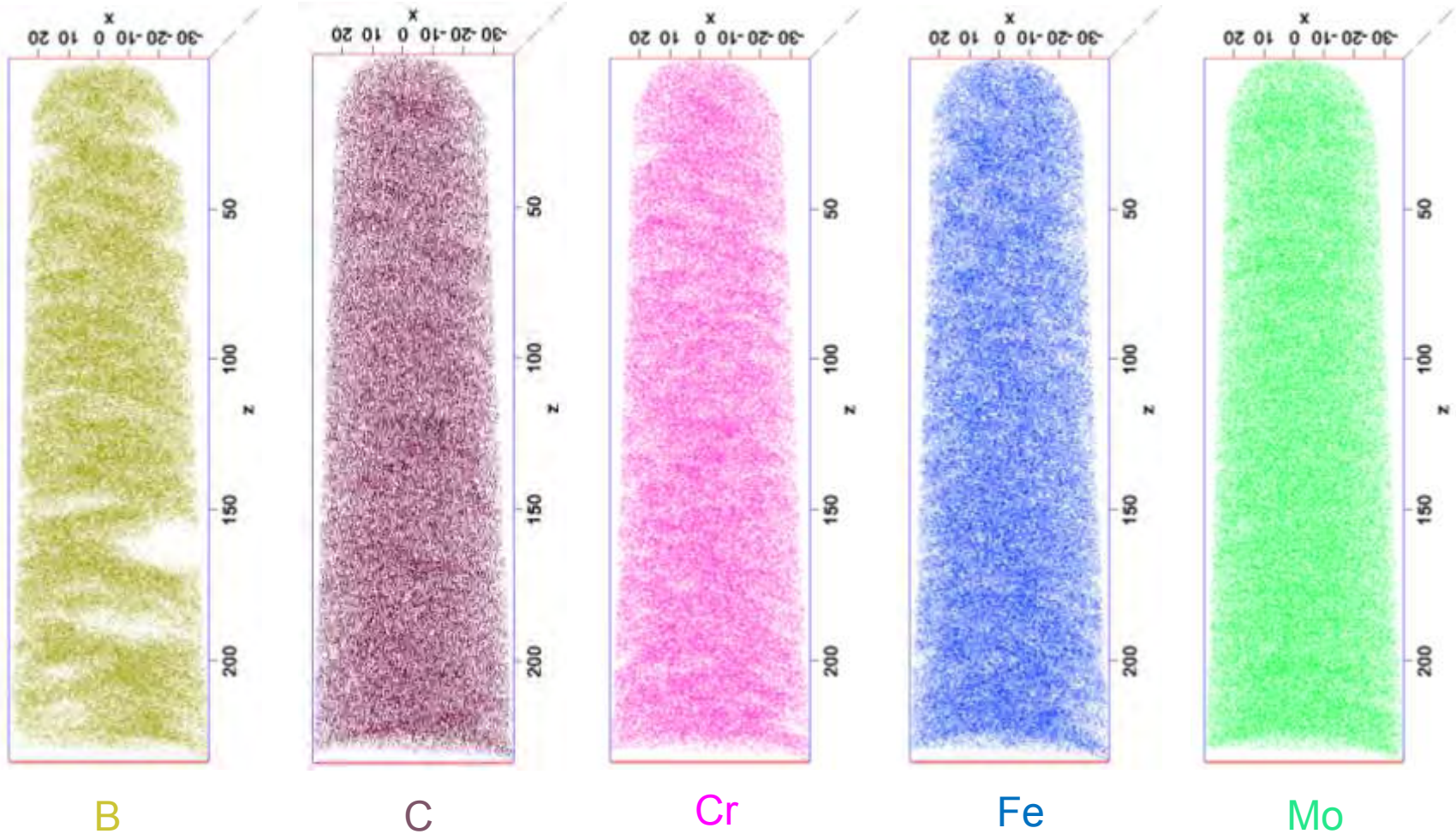
450°C aging

Iso-concentration surfaces at Cu 11 at.%



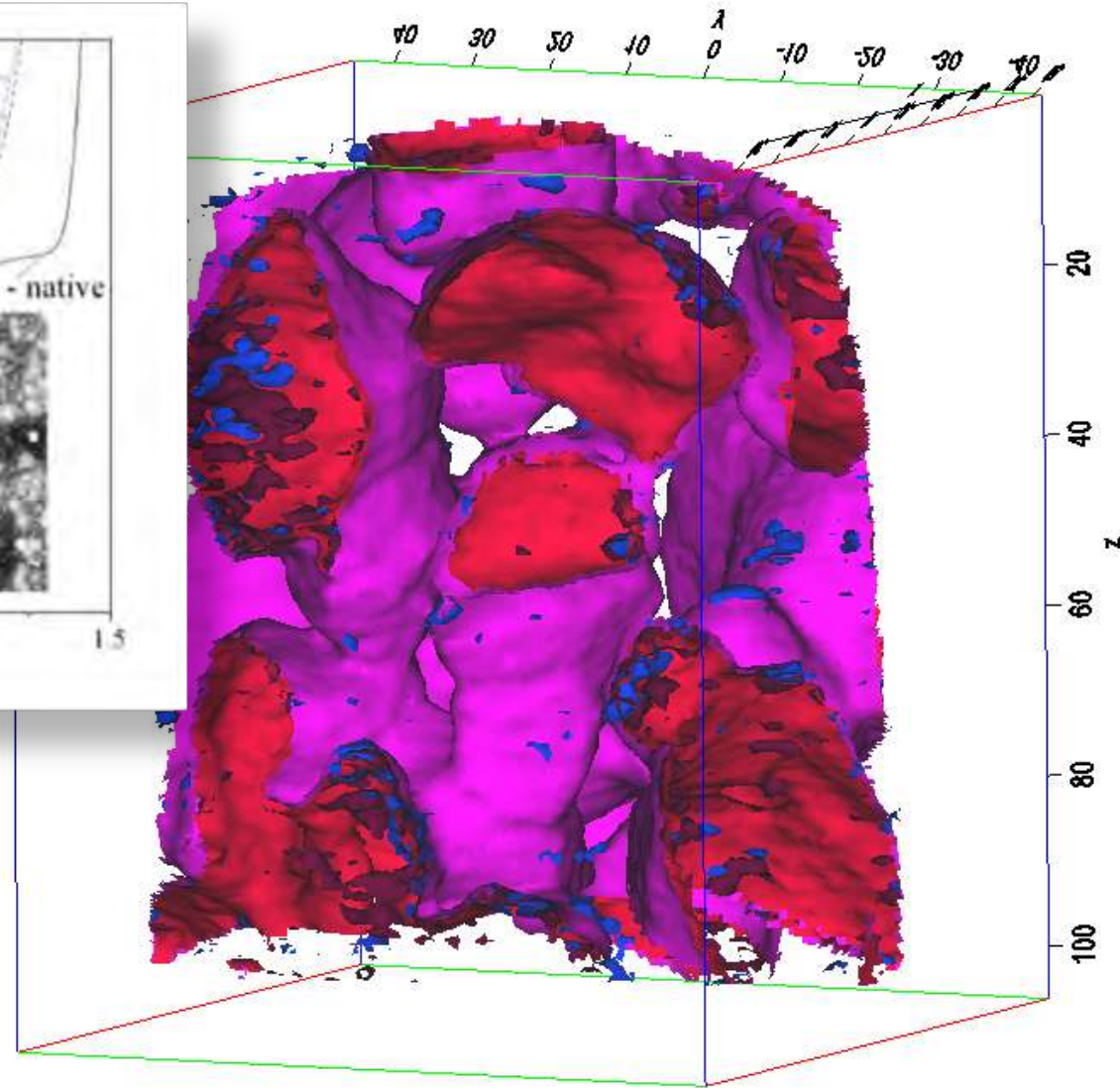
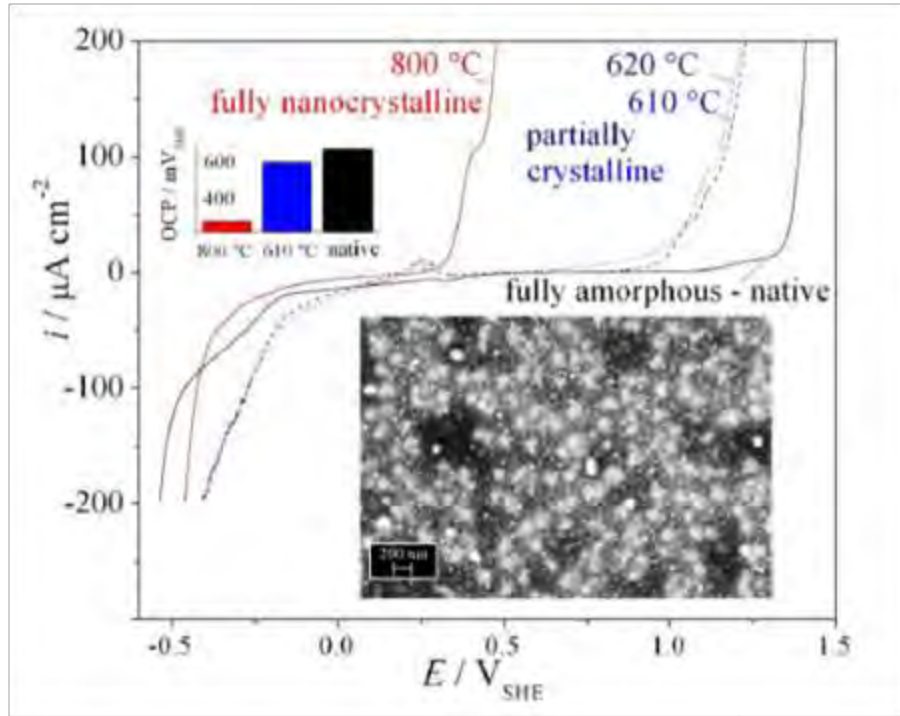
6000 min

20 nm



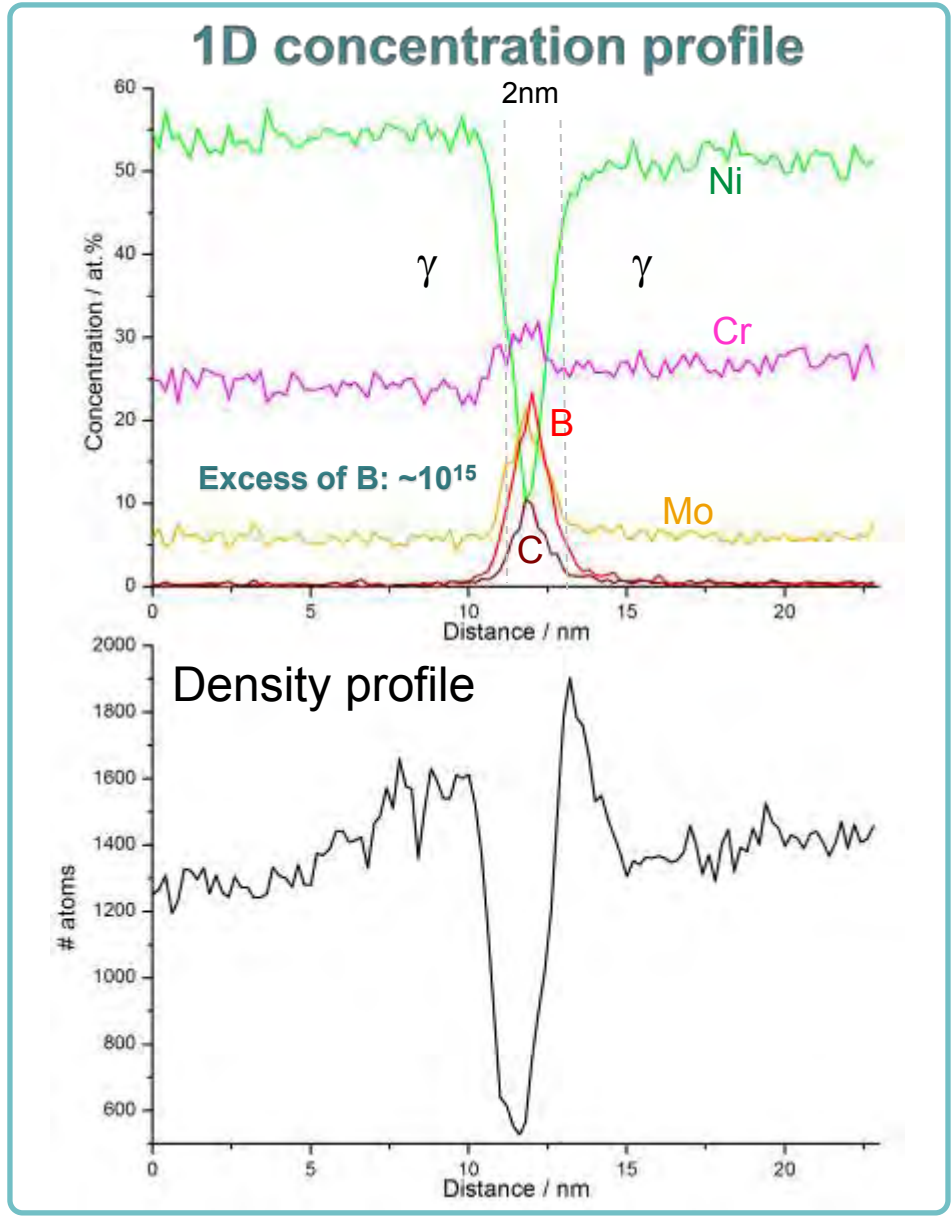
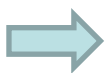
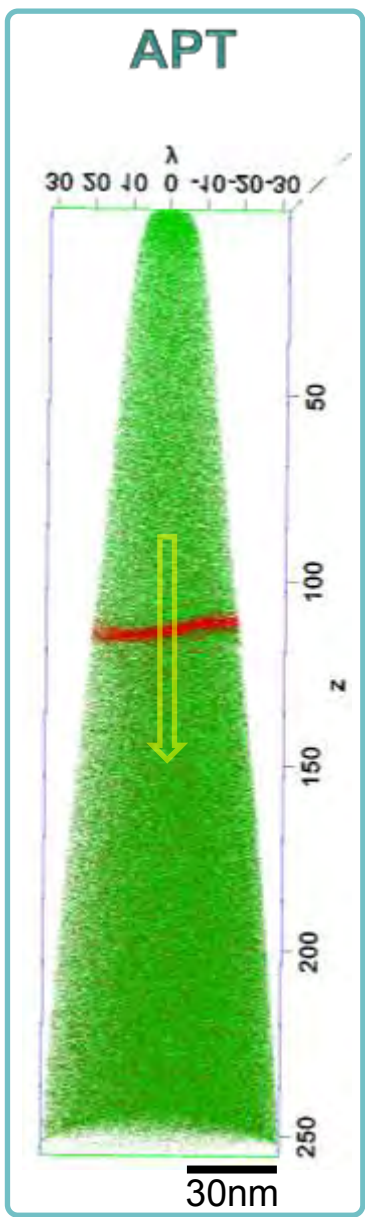
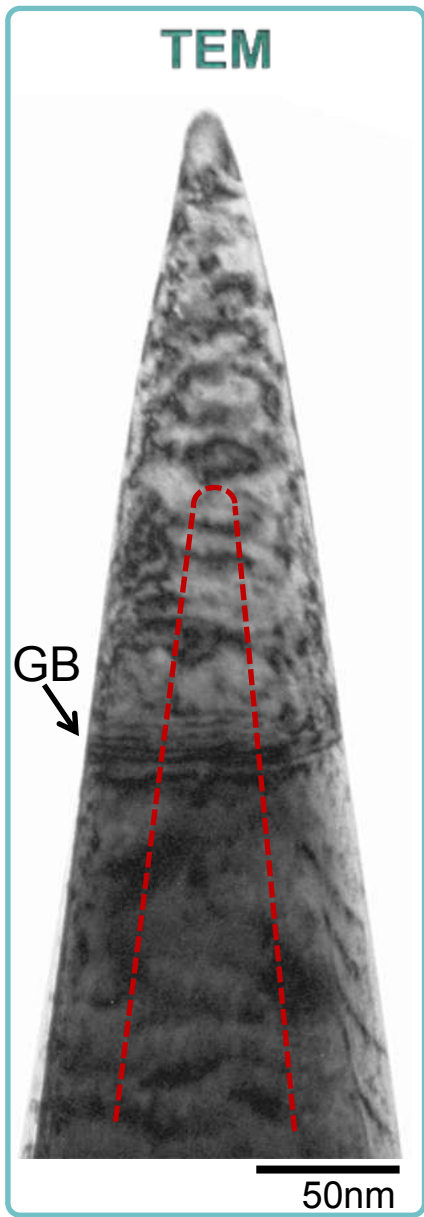
Elements	B	C	Cr	Fe	Mo
Atomic %	5.75	12.314	18.701	44.103	17.698

24 million atoms were detected



Analyses:

- Proxigram - interfacial chemistry
- Sub-cut phases, treating them individually
- approx. sizes of phases
- cluster search algorithm within each phase
- 1-D composition parallel vs. perp. through boundaries



Why?

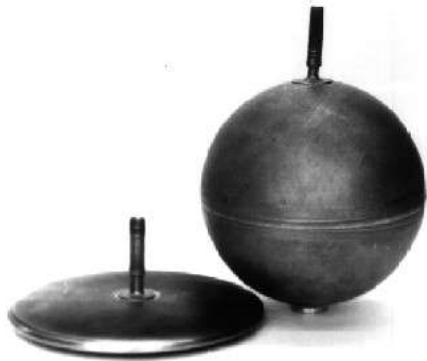
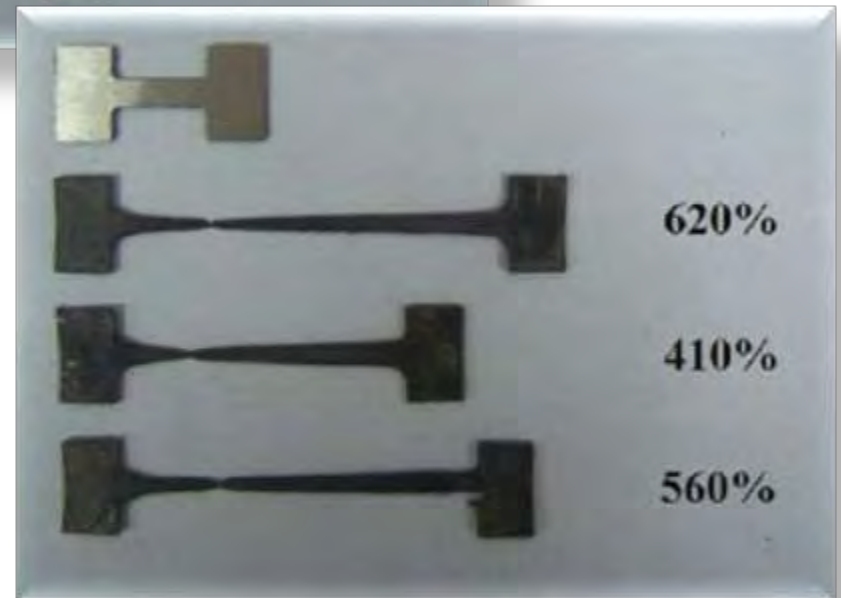
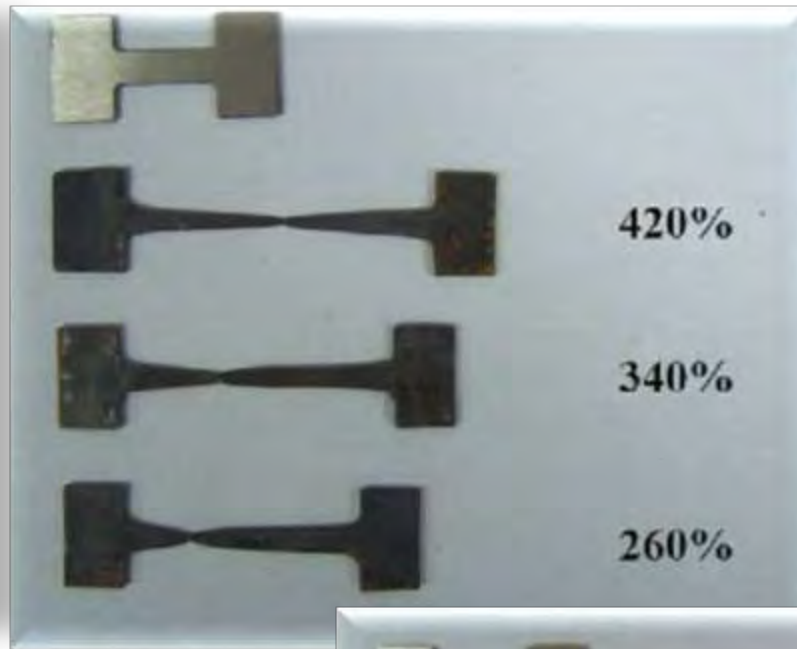
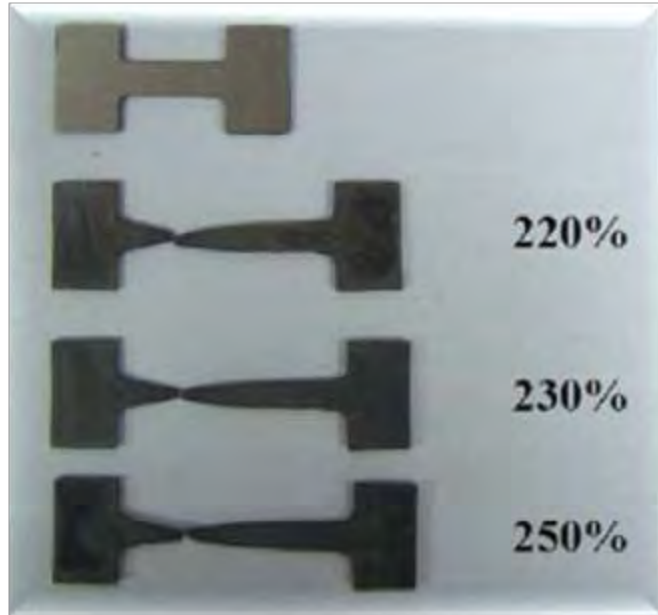
Think new !

Add new properties that steel did not have before, e.g. in the field of manufacturing.

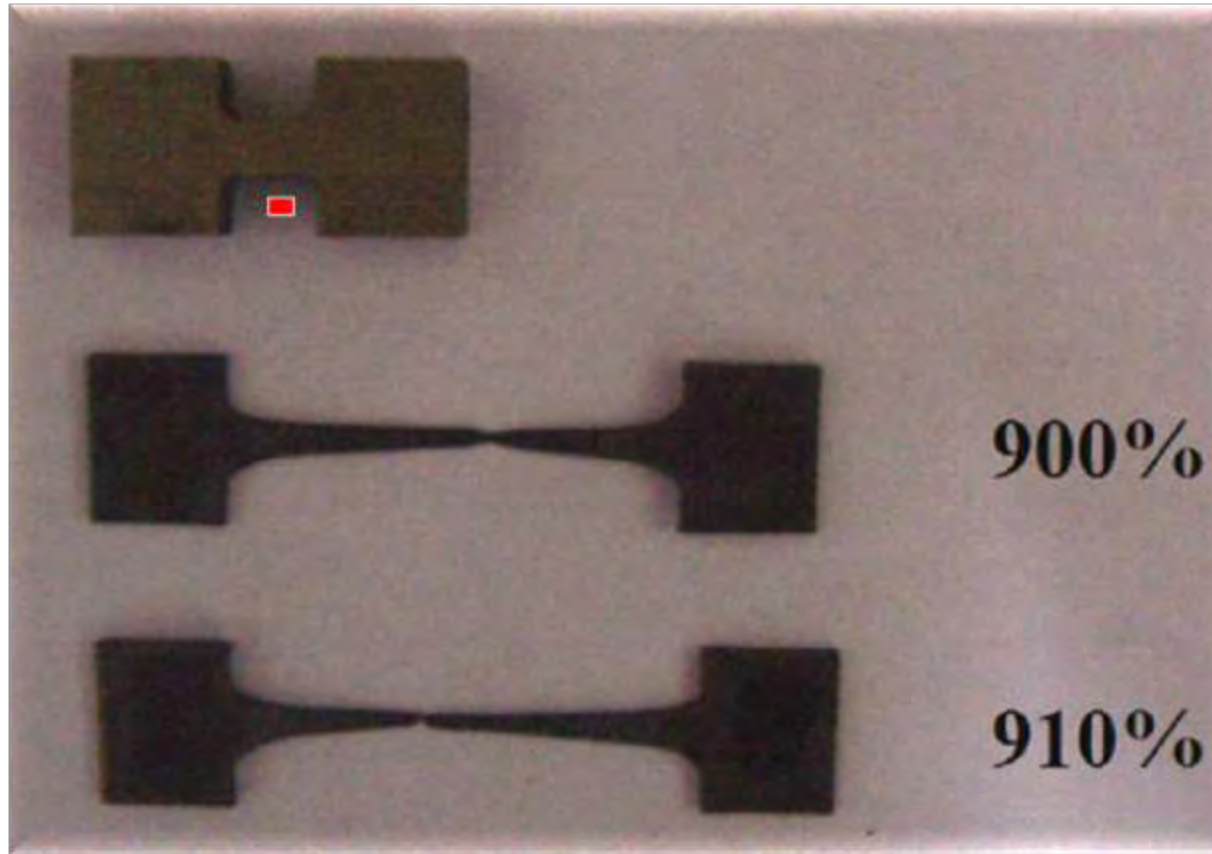
Combine: extreme forming of noble and complex shapes with extreme strength.



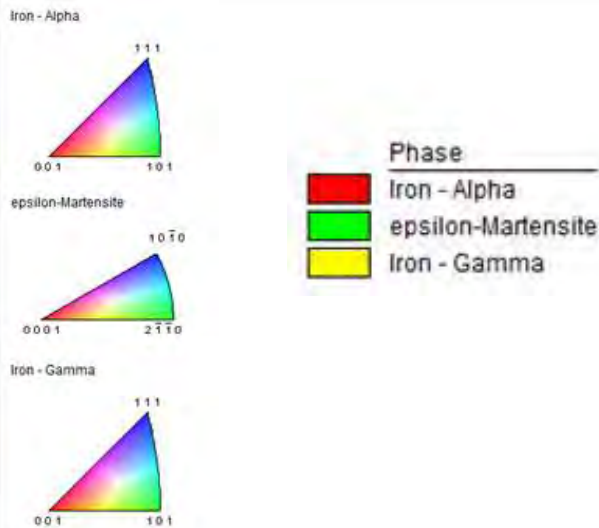
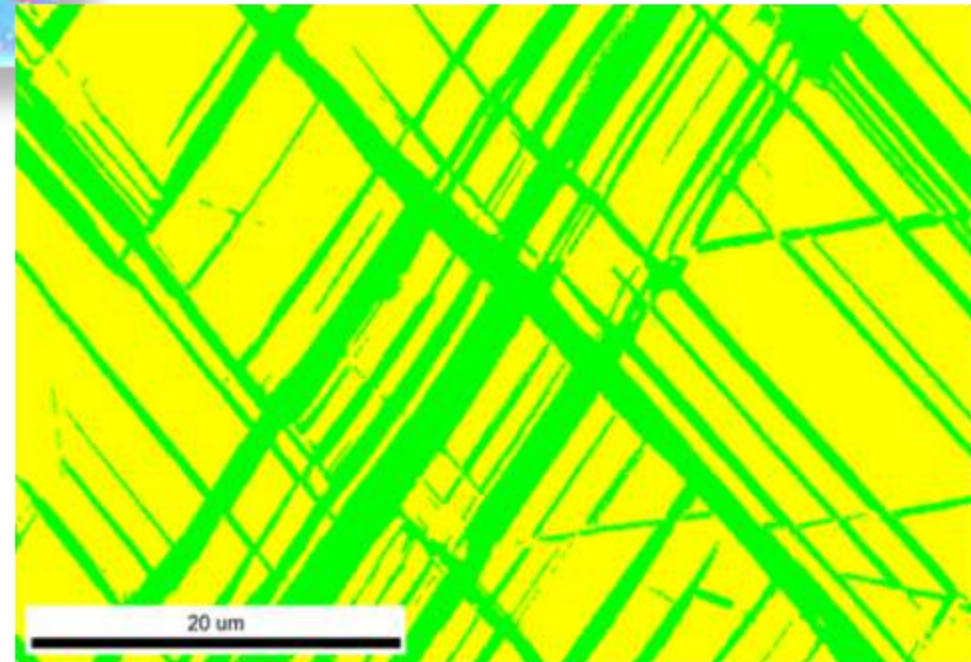
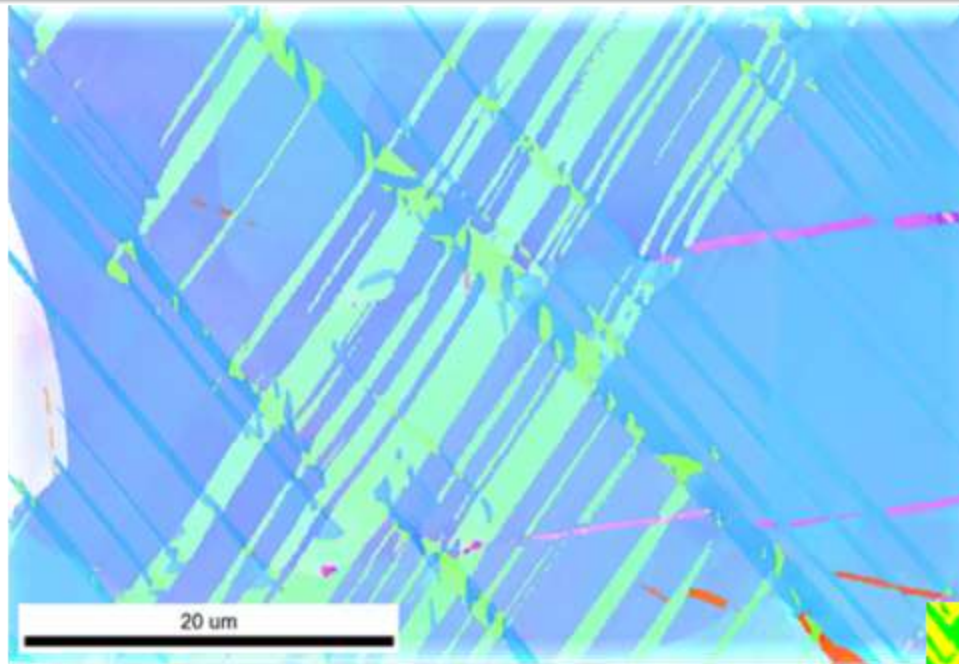
Superplastic steels



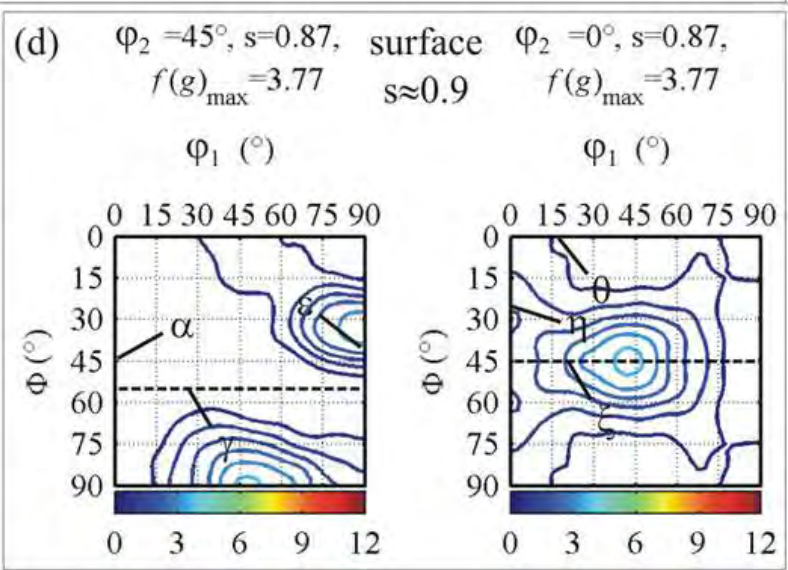
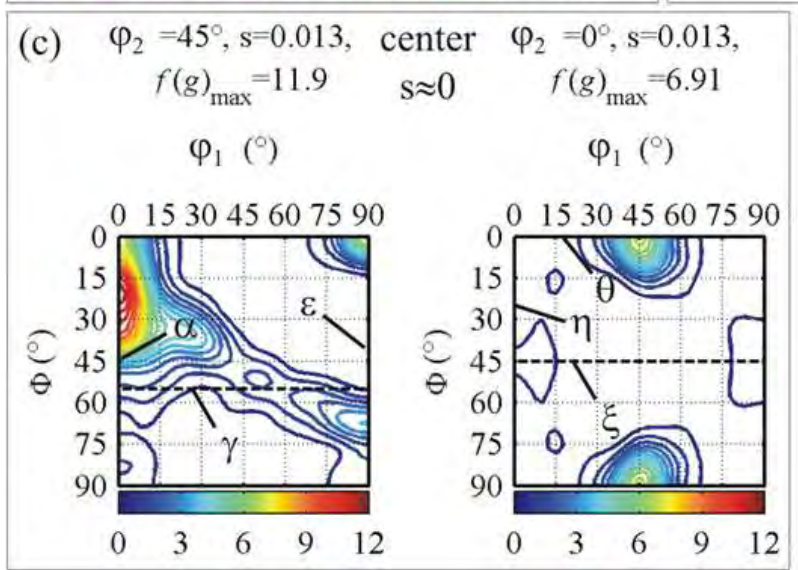
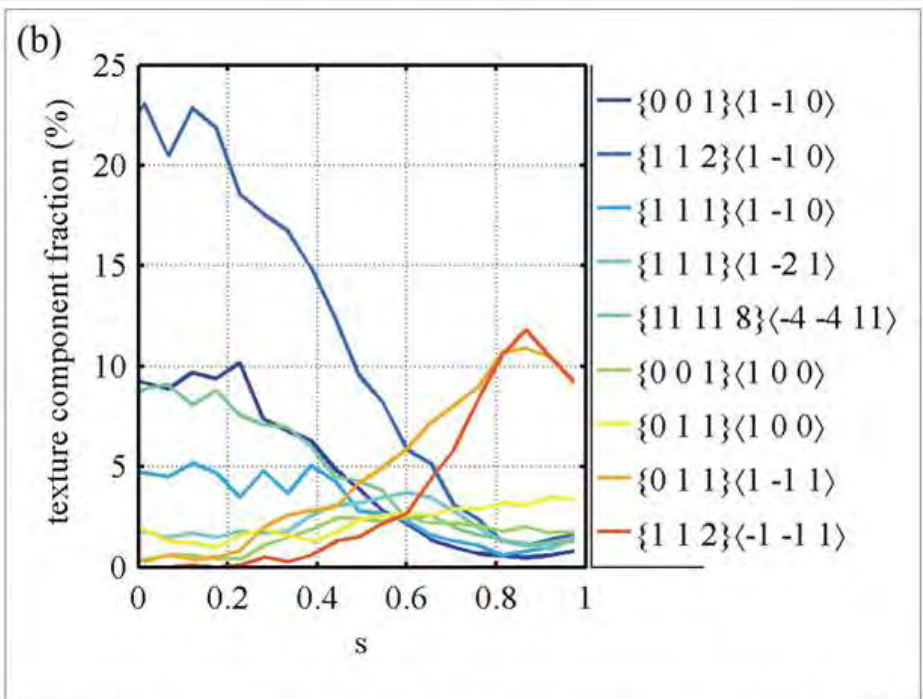
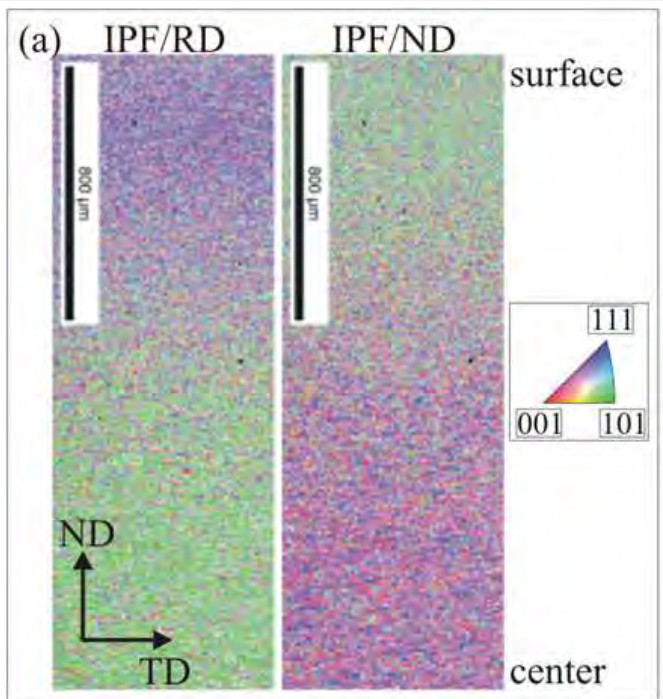
> 1 C- 2-3 Mn- 1-2 Si- Cr steels (mass%)



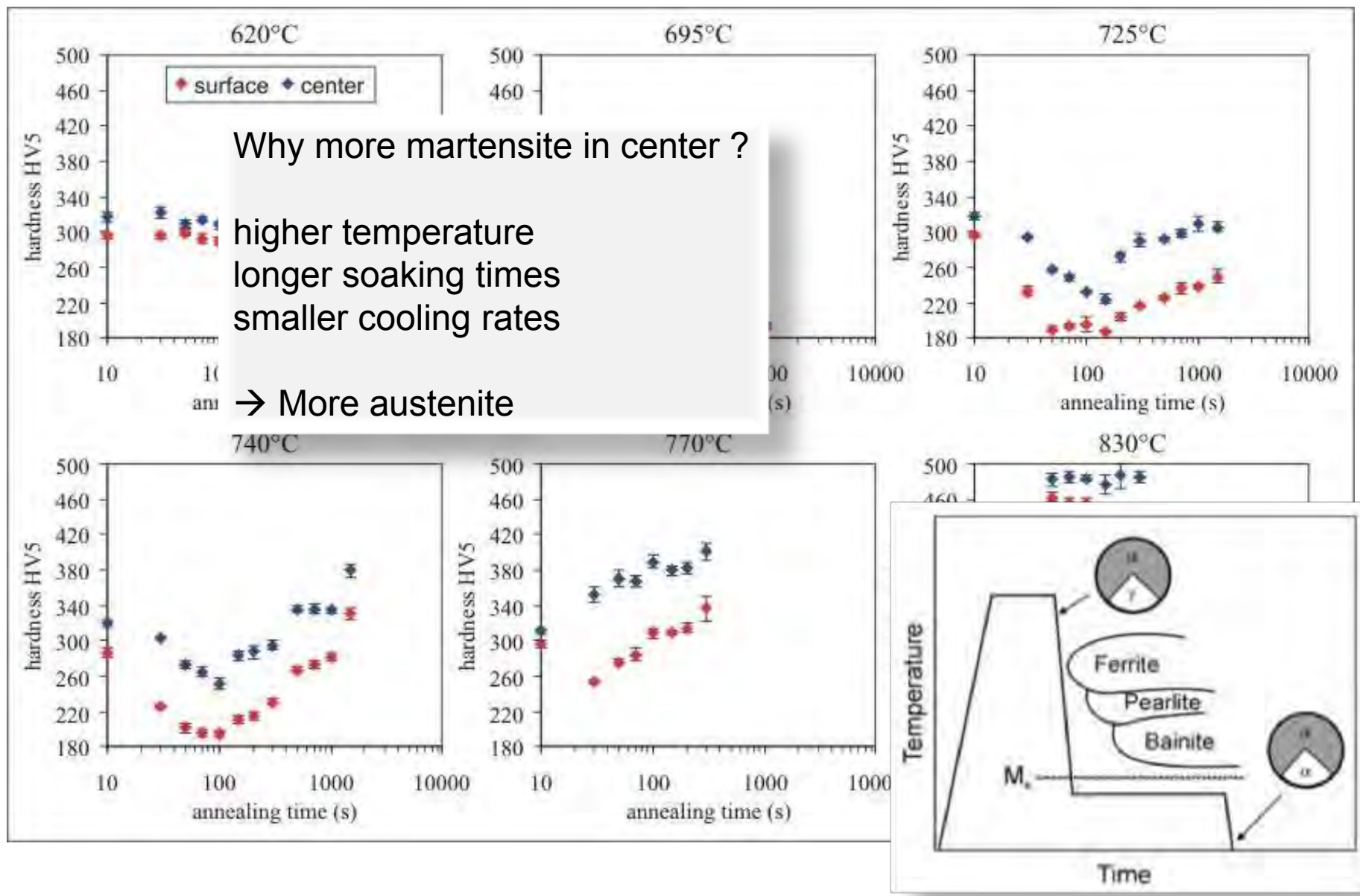
For new cast alloys:
few α' martensite induced at intersections between ϵ martensite **after deformation.**



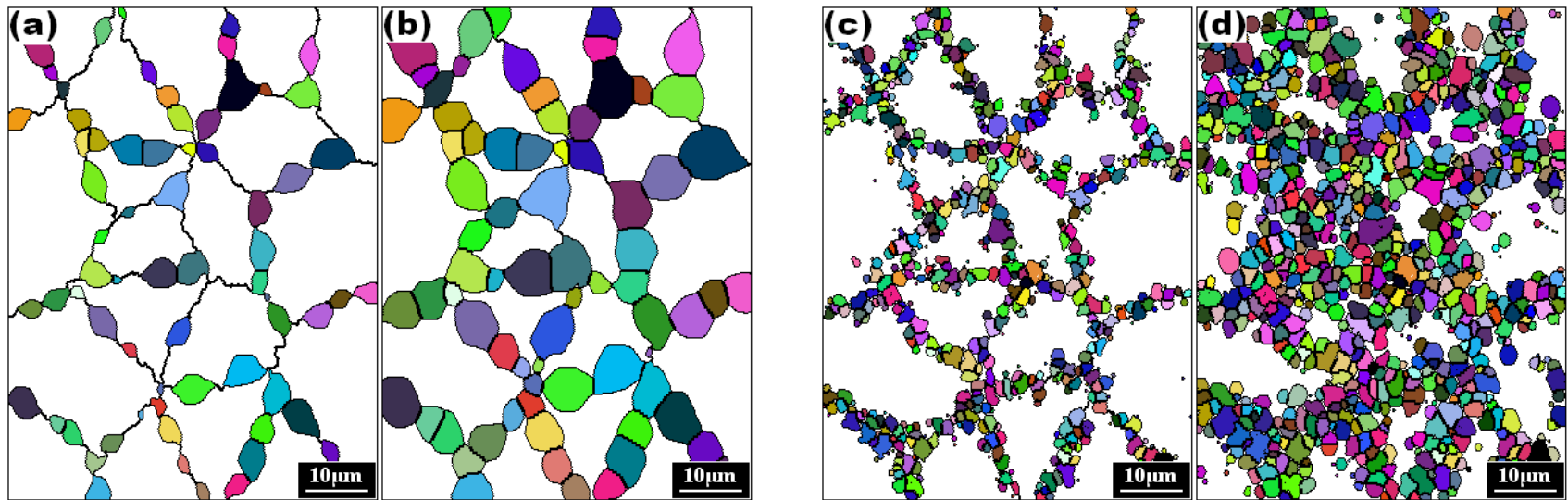
Microstructure and texture evolution – hot band through thickness



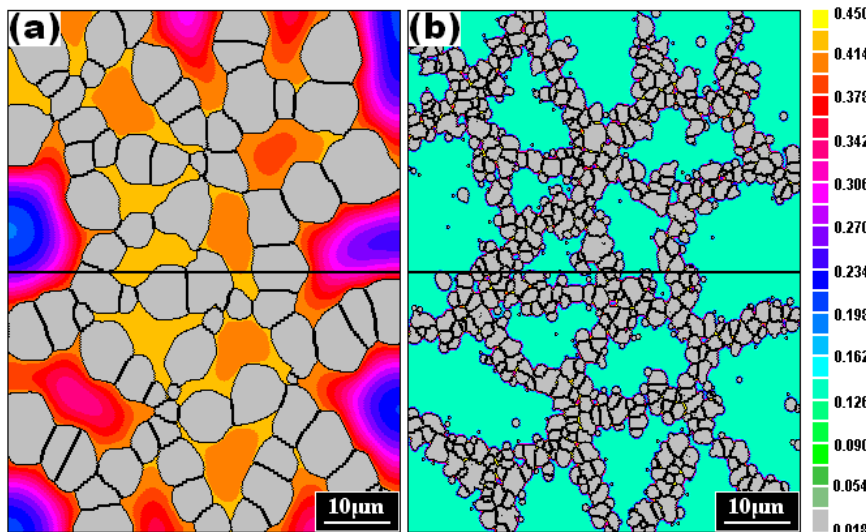
Competition: recrystallization -transformation, through thickness



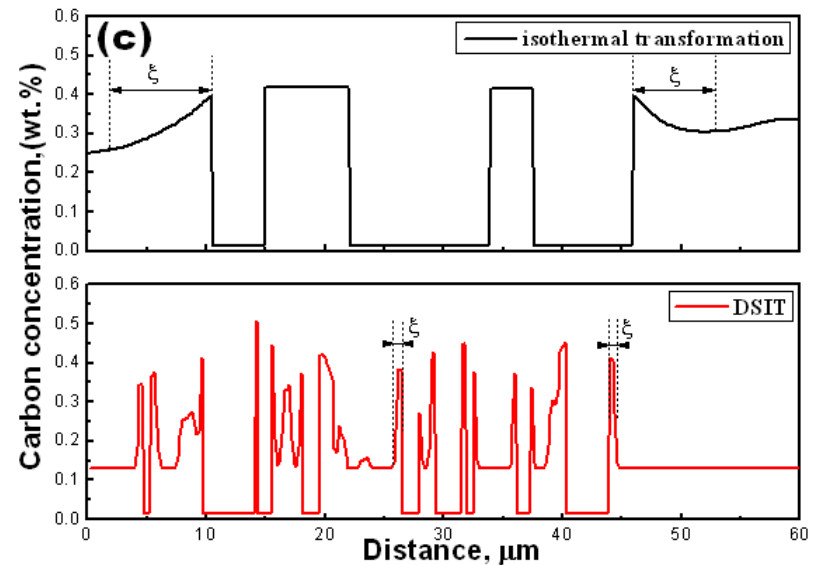
Simulation of recrystallization and C diffusion



Simulated microstructure evolution at 780° C: (a) $t = 5s$; (b) $t = 15s$ and the DSIT: at (c) strain: 0.3; d) 0.8
 DSIT: dynamic strain-induced transformation



C-distribution: 780° C: $t = 20s$; conventional, DSIT



Texture and microstructure—rolled, annealed, through thickness

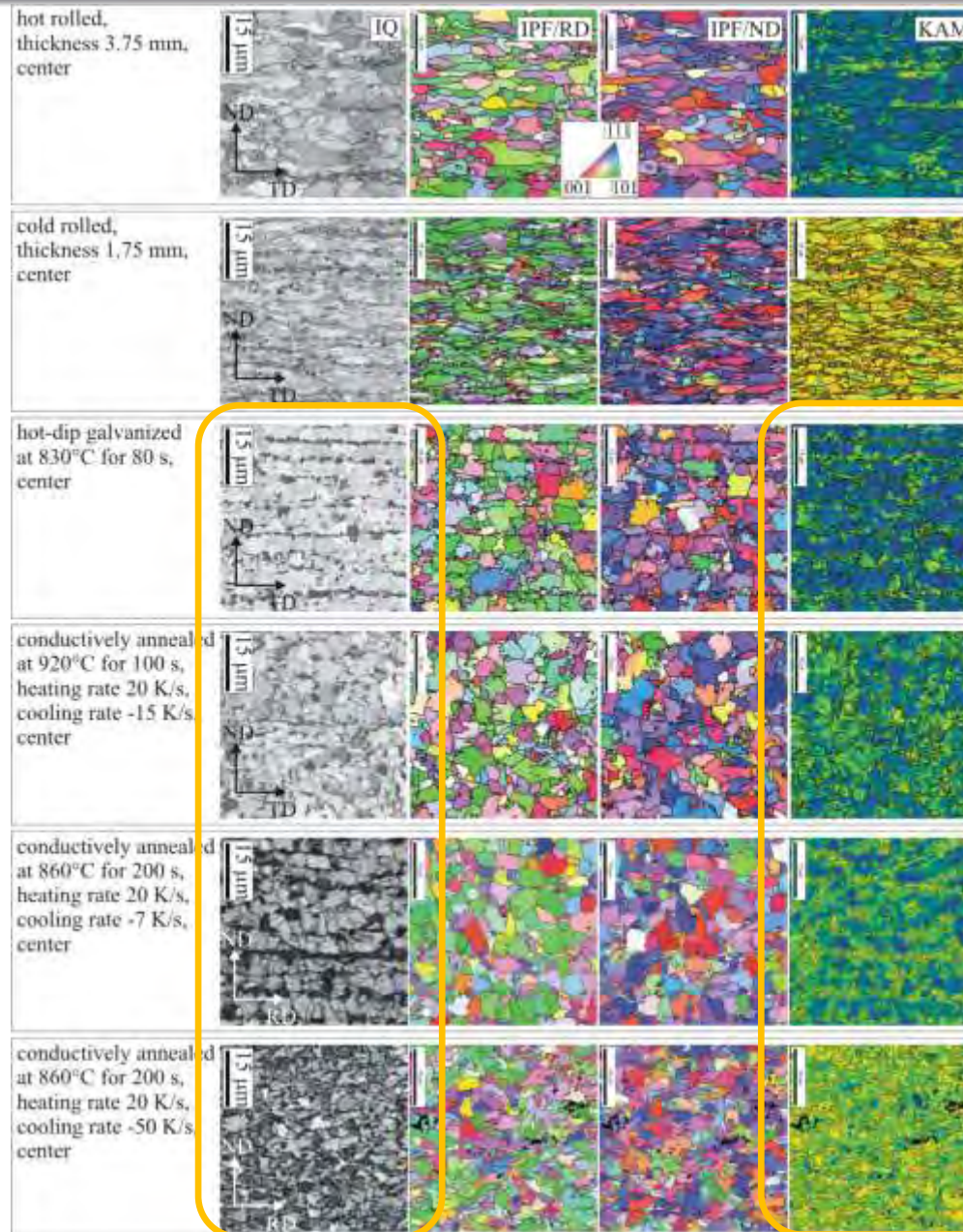
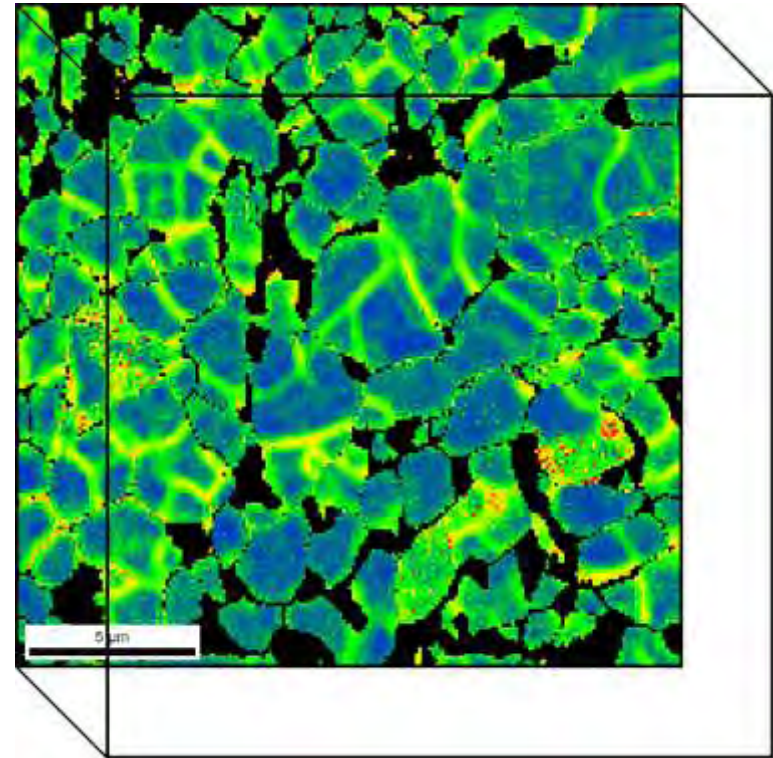
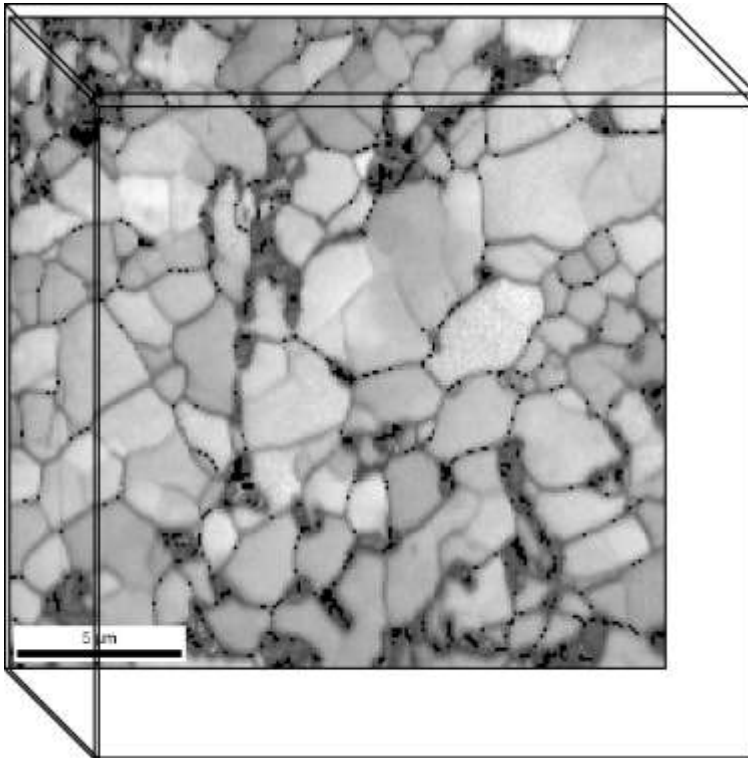




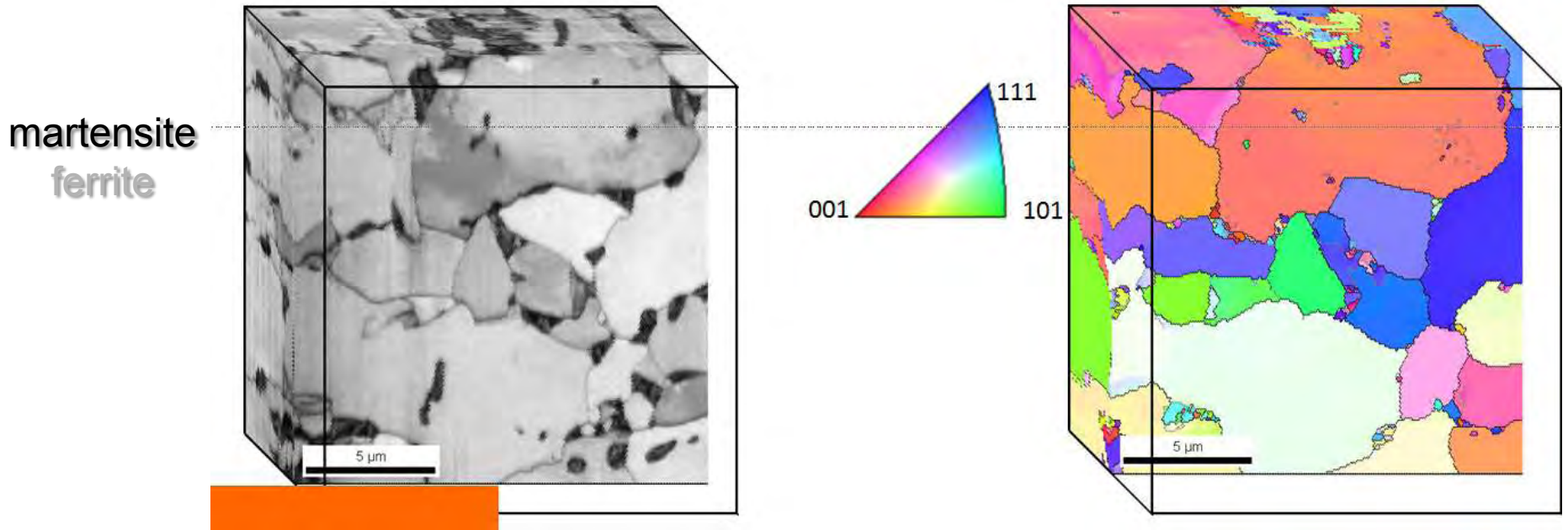
Image Quality

Kernel Average Misorientation
(martensite highlighted in black)

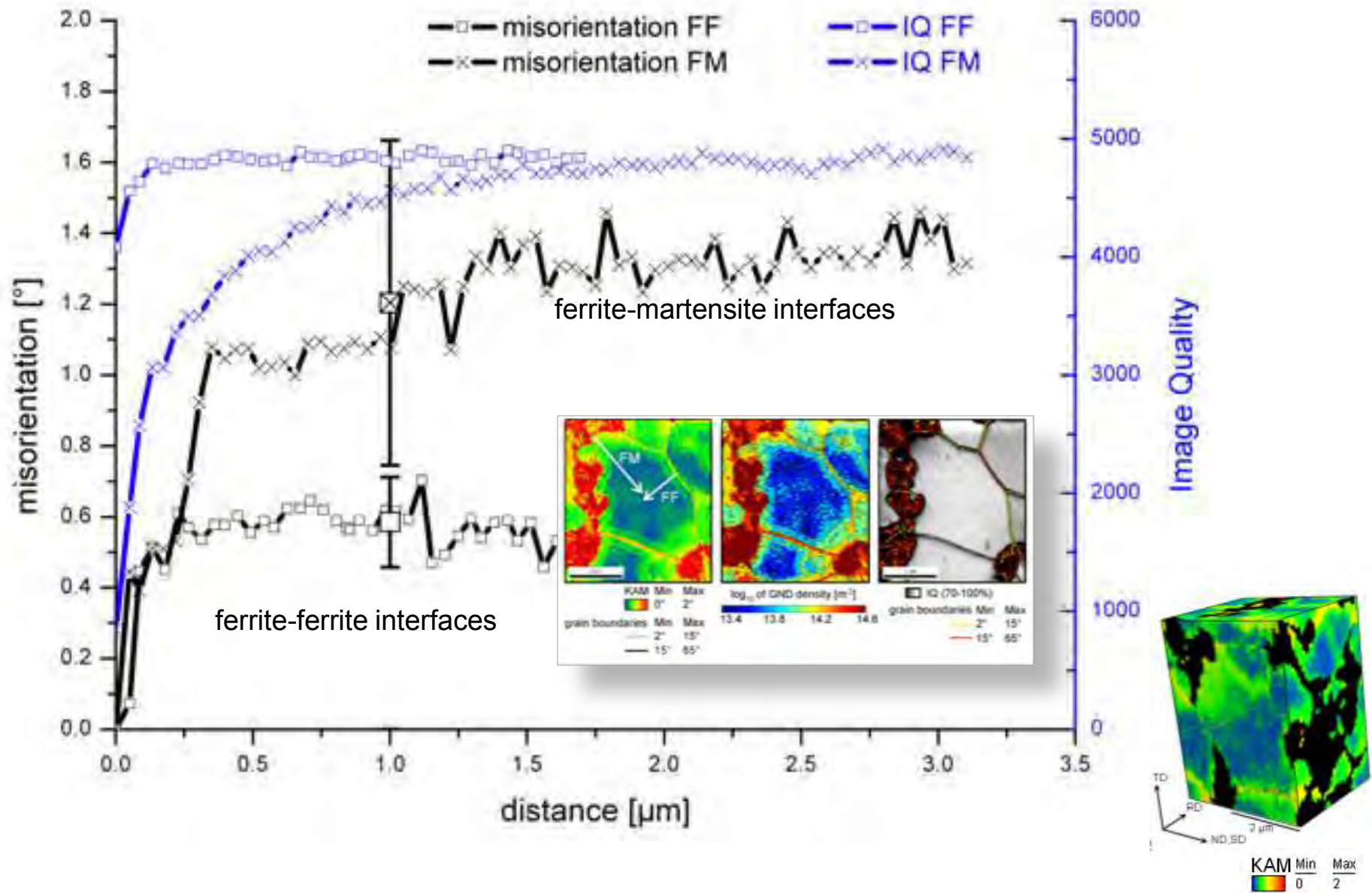


3D EBSD experiment

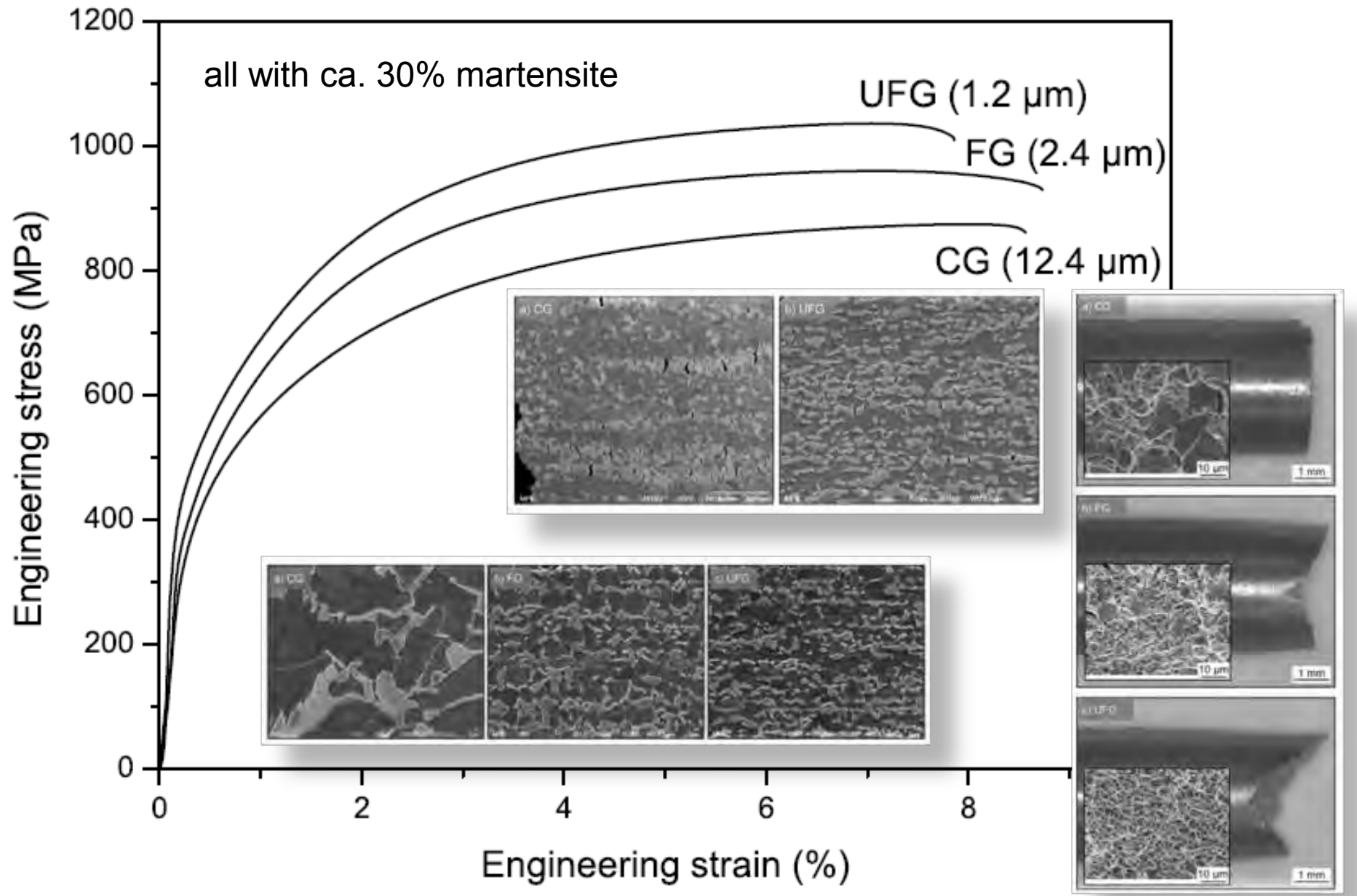




3D EBSD experiment



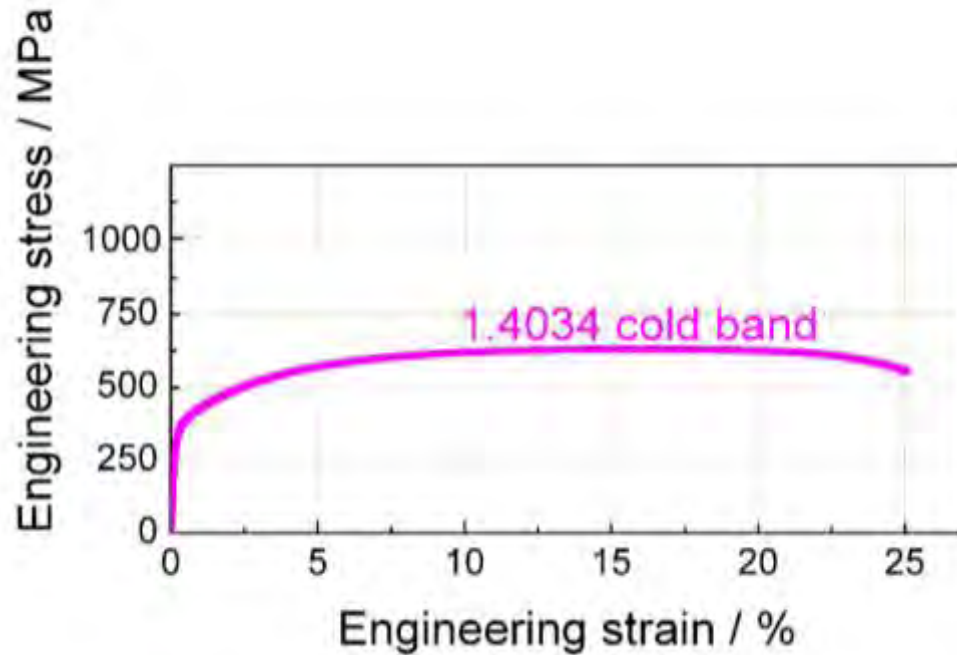
Ultrafine grained DP steels





650 MPa to 2 GPa

Ultra high strength and corrosion resistance



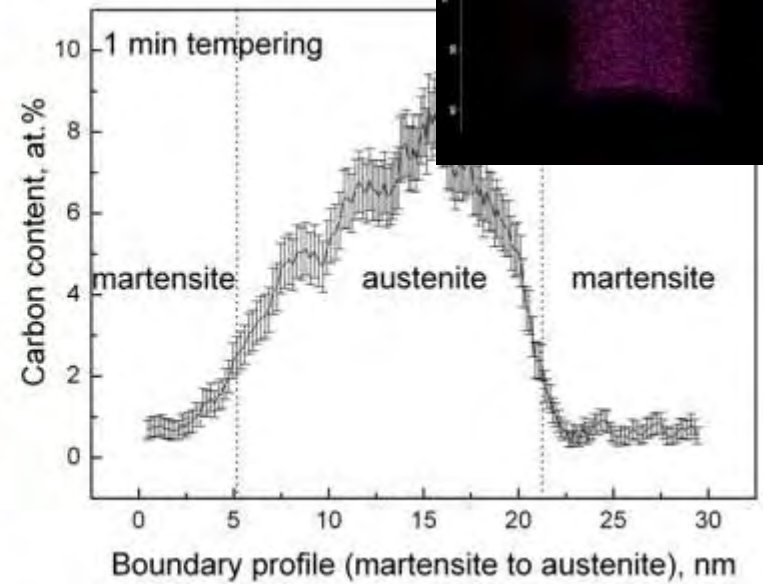
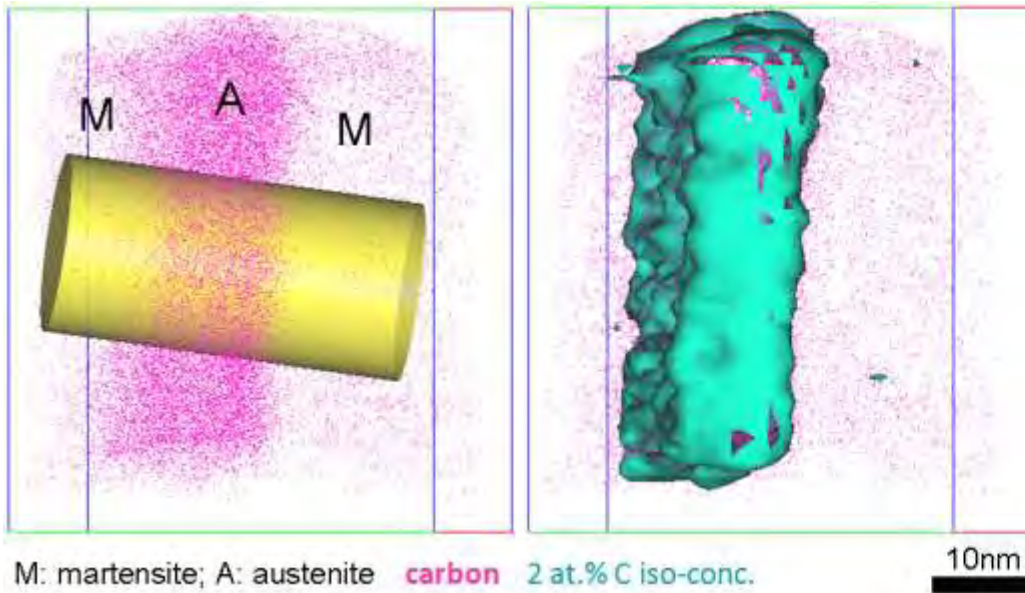
400°C aging: Ms-relaxation + prec. (aging) + austenite reversion

Fe-13.6Cr-0.44C (wt.%)



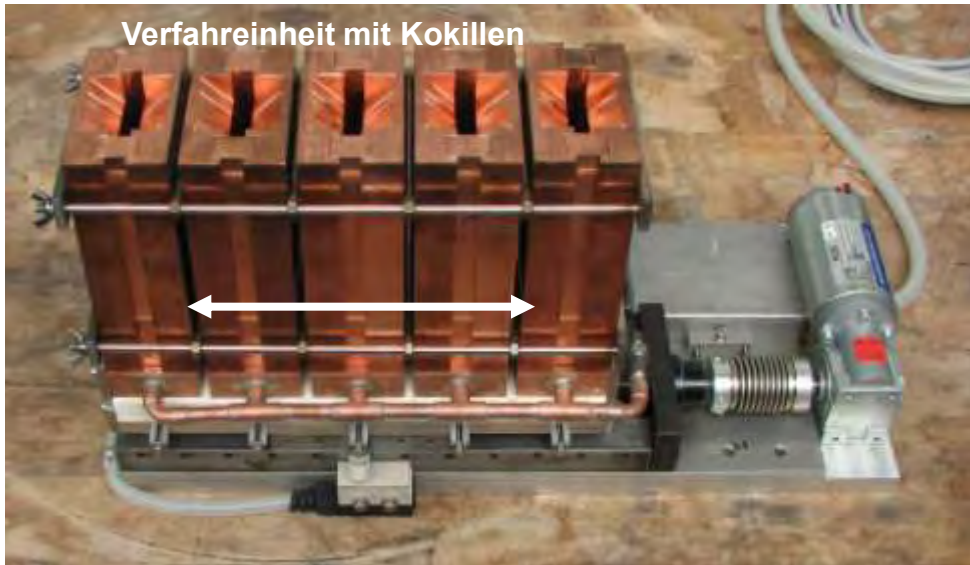


at 5.45 at.% C, austenite forms at 400°C



- C has 'Λ' shape in austenite layer: Gibbs adsorption isotherm; C on martensite grain boundaries
- C has 'V' shape in austenite layer: austenite reversion through partitioning and kinetic freezing

Stahlwerk 'in a box'



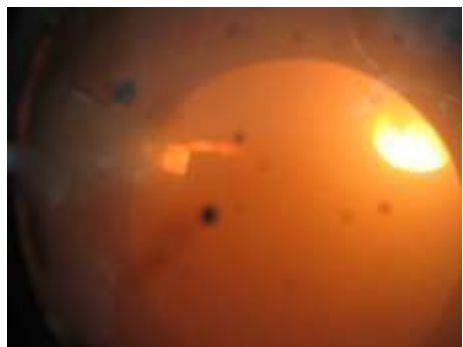
Verfahreinheit mit Kokillen

Verfahreinheit für 5 Cu-Kokillen,
eingebaut in 60 kW Vakuum-
Induktionsofen (Argon Atmosphäre)

Bodenplatte wassergekühlt, elektrische
Positionsanzeige

Starten von Basisschmelze → Abguß →
eindimensional Auflegieren → Verfahren
→ Abguß → ...

➔ 5 Abgüsse à 10 x 50 x 150 mm³



Multistage strain hardening through dislocation substructure and twinning in a high strength and ductile weight-reduced Fe–Mn–Al–C steel

I. Gutierrez-Urrutia ^{*}, D. Raabe

Max-Planck-Institut für Eisenforschung, Max-Planck Str. 1, D-40237 Düsseldorf, Germany

Received 20 May 2012; received in revised form 1 July 2012; accepted 3 July 2012

Available online 23 August 2012

Abstract

We investigate the kinetics of the deformation structure evolution and its contribution to the strain hardening of a Fe–30.5Mn–2.1Al–1.2C (wt.%) steel during tensile deformation by means of transmission electron microscopy and electron channeling contrast imaging combined with electron backscatter diffraction. The alloy exhibits a superior combination of strength and ductility (ultimate tensile strength of 1.6 GPa and elongation to failure of 55%) due to the multiple-stage strain hardening. We explain this behavior in terms of dislocation substructure refinement and subsequent activation of deformation twinning. The early hardening stage is fully determined by the size of the dislocation substructure, namely, Taylor lattices, cell blocks and dislocation cells. The high carbon content in solid solution has a pronounced effect on the evolving dislocation substructure. We attribute this effect to the reduction of the dislocation cross-slip frequency by solute carbon. With increasing applied stress, the cross-slip frequency increases. This results in a gradual transition from planar (Taylor lattices) to wavy (cells, cell blocks) dislocation configurations. The size of such dislocation substructures scales inversely with the applied resolved stress. We do not observe the so-called microband-induced plasticity effect. In the present case, due to texture effects, microbanding is not favored during tensile deformation and, hence, has no effect on strain hardening.

© 2012 Acta Materialia Inc. Published by Elsevier Ltd. All rights reserved.

Keywords: Strain hardening; Electron channeling contrast imaging; Austenitic steel; Deformation structures; Dislocation structures

1. Introduction

High manganese steels have an outstanding combination of strength and ductility owing to their high strain hardening capacity. They are austenitic, i.e. face-centered cubic (fcc) alloys, with a high Mn content (typically between 20 and 30 wt.%) and additions of elements such as carbon (<1 wt.%), silicon (<3 wt.%), or aluminum (<10 wt.%) [1–11]. High-Mn steels exhibit different hardening mechanisms which have been commonly interpreted in terms of the stacking fault energy [6,8,9,12–18]. Several authors have considered the role of clustering of carbon and manganese atoms on strain hardening [5,19–21], in

particular, on the occurrence of serrated flow. For instance, Saeed-Akbari et al. [22] have recently addressed the influence of short range ordering (SRO) on strain hardening. These authors suggest a strain hardening parameter (the so-called theoretical ordering index, TOI) that is related to the SRO strengthening mechanism. Among the different strain hardening mechanisms, twinning-induced plasticity (TWIP) has received much interest due to the good mechanical compatibility between dislocation slip and the dynamically refined twin interfaces compared to other chemical/crystallographic interfaces (for instance, ϵ -martensite) [1,4,6–8,13,23,24]. As twin interfaces act as strong obstacles to dislocation glide, microstructure refinement by deformation twinning increases the strain-hardening rate. The TWIP effect is therefore determined by the twinning kinetics, more specifically by the twinning rate and the average twin spacing.

^{*} Corresponding author. Tel.: +49 2116792 407; fax: +49 2115792333.
E-mail address: i.gutierrez@mpie.de (I. Gutierrez-Urrutia).

Recently, a new hardening mechanism has been proposed in high-Mn steels, namely, microband-induced plasticity (MBIP) [3,25,26]. This mechanism has been reported in Fe–Mn–Al–C alloys with high stacking fault energy ($50\text{--}90\text{ mJ m}^{-2}$). These alloys exhibit an outstanding combination of strength (ultimate tensile strength of $\sim 900\text{ MPa}$) and ductility ($\sim 100\%$ elongation to fracture). Furthermore, the high aluminum content (up to 10 wt.%) renders these steels lightweight alternatives to conventional high strength structural materials. MBIP has been ascribed to the formation of microbands and their role as an individual strain hardening mechanism. The microbands were described as in-grain narrow shear zones that are delimited by geometrically necessary boundaries. However, upon deformation different types of dislocation substructures such as highly dense dislocation walls (HDDWs) and Taylor lattices have been observed as well. Up to now no detailed quantitative characterization of the underlying kinetics of the substructure evolution and their correspondence to the stress–strain and strain hardening evolution in the FeMnAlC system have been performed. Specifically, the contributions of the different types of dislocation substructures, namely, HDDWs, Taylor lattices and microbands, to the excellent strain hardening capacity of FeMnAlC steels are still unclear. Therefore, the present study has the following aims. First, we study in detail the contribution of the evolving dislocation substructure and its effect on strain hardening. Specifically, we aim at clarifying the role of microbanding in FeMnAlC steels. Second, we explore the various suggested strain hardening mechanisms, namely, microband hardening through dislocation substructure patterning (MBIP) and deformation twinning (TWIP), as well as their interactions, in order to better understand the strain hardening behavior of FeMnAlC steels. For these purposes, we have selected a Fe–30.5Mn–2.1Al–1.2C (in wt.%) alloy in solid solution state. We performed a complete quantitative characterization of the underlying deformation structure by transmission electron microscopy (TEM) and electron channeling contrast imaging (ECCI). The ECCI technique combined with electron backscatter diffraction (EBSD) allows us to characterize the deformed structure at a wide field of view in the scanning electron microscope (SEM) [4,13,23,27–30] with a better dislocation and interface contrast than the basic ECCI technique [31]. The contribution of the so characterized dislocation and twin substructures to the strain hardening is analyzed in terms of the dislocation mean free path approach.

2. Experimental

The high-Mn steel used in this study had the chemical composition Fe–30.5Mn–2.1Al–1.2C (in wt.%). The material was melted in an induction furnace under Ar atmosphere and cast to round bars of 25 mm diameter. The cast ingot was reheated to 1200 °C for 30 min, hot-rolled to 75% thickness reduction at 1100 °C, and water quenched. The hot-rolled material was then solution-trea-

ted for 2 h at 1100 °C under Ar, and final water quenching. To avoid any microstructure instability, the samples were subjected to a short annealing at 450 °C for 1 h. The as-annealed material showed a fully austenitic structure with an average grain size of 50 μm , which remained stable during deformation at room temperature. No precipitates were detected by TEM, either in diffraction mode (appearance of extra spots) or in image mode at high magnification. Hence, the present alloy was in solid solution state. Tensile tests were carried out at room temperature at an initial strain rate of $5 \times 10^{-4}\text{ s}^{-1}$ in a Zwick ZH 100 tensile machine. In addition to tensile testing to failure, interrupted tensile tests to true strains of $\varepsilon = 0.02, 0.10, 0.20$ and 0.30 were performed to study the microstructural evolution as a function of strain. The tensile samples were cylindrical, with gauges of 6 mm diameter and 40 mm length. Microstructures of the tensile deformed high-Mn steel were examined by EBSD, ECCI, and TEM. The longitudinal section was examined, i.e. the observation direction was perpendicular to the tensile axis. The EBSD technique was used to analyze the local crystallographic texture. Orientation maps were taken in a 6500 F JEOL field emission gun-scanning electron microscope (FEG-SEM) equipped with a TSL OIM EBSD system at 15 kV acceleration voltage and a working distance of 15 mm. Quantitative characterization of the deformed structure was conducted by ECCI, as in previous works [4,13,23,27,29,30]. We used a newly developed EBSD-based set-up to obtain ECCI images under controlled diffraction conditions, enabling enhanced dislocation and interface contrast [27]. ECCI images were obtained with optimum contrast by orienting the matrix crystal exactly in Bragg condition for a high intensity reflection and exciting the corresponding diffraction vector in a “two-beam” condition. ECCI observations were carried out in a Zeiss Crossbeam instrument (XB 1540, Carl Zeiss SMT AG, Germany). TEM observations were conducted in a Phillips CM20 microscope. Thin foil samples were prepared by electropolishing using 30% nitric acid in methanol at $-30\text{ }^\circ\text{C}$ and 10 V.

3. Results

3.1. Strain hardening

Fig. 1a shows the true stress–true strain curve of the Fe–30.5Mn–2.1Al–1.2C (wt.%) steel with an average grain size of 50 μm tensile deformed at an initial strain rate of $5 \times 10^{-4}\text{ s}^{-1}$, i.e. the true strain rate was not constant. The material exhibits excellent mechanical properties, combining high strength (ultimate tensile strength of 1.6 GPa) and ductility (elongation to failure of 55%). At room temperature and an initial strain rate of $5 \times 10^{-4}\text{ s}^{-1}$, no serrated flow occurred. The stress–strain curve exhibits a significant variation in slope at $\sim 20\%$ true strain. At this strain level, the slope decreases but is still positive, indicating the activation of a secondary strain hardening stage.

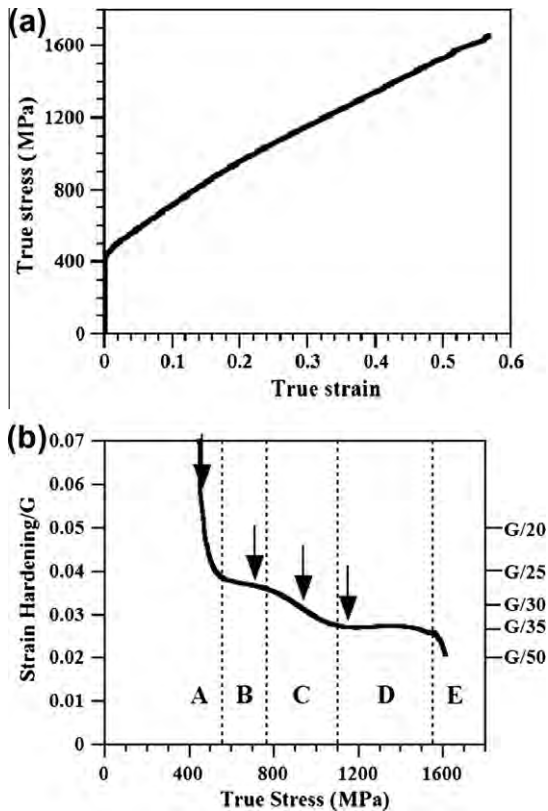


Fig. 1. True stress–true strain curve (a) and normalized strain hardening rate (normalized with shear modulus) vs. true stress (b) of Fe–30.5Mn–2.1Al–1.2C (wt.%) steel tensile deformed at an initial strain rate of $5 \times 10^{-4} \text{ s}^{-1}$.

Fig. 1b shows the normalized strain hardening rate (normalized by the shear modulus) vs. flow stress of the tensile deformed alloy. Arrows indicate the different deformation stages described in the subsequent section. The main characteristic revealed in Fig. 1b is the occurrence of a multiple-stage strain hardening behavior. In particular, in the present material five different deformation stages can be distinguished in the evolution of the strain hardening rate with the true stress. The first stage, referred to as stage A, is characterized by a continuous decrease of the strain hardening rate until a stress of 560 MPa, stage B. This stage reveals a nearly constant hardening rate with a strain hardening coefficient of $\sim G/27$, where G is the shear modulus ($G = 70 \text{ GPa}$ [32]). With further stress, the strain hardening rate decreases gradually, stage C, until the onset of stage D. This stage exhibits a nearly constant strain hardening rate with a strain hardening coefficient of $\sim G/35$. Finally, the

strain hardening rate decreases until rupture, stage E. It should be pointed out that the labeling of the hardening stages used in this work must not be confused with the classical hardening stage analysis used for single crystals and polycrystals of medium–high stacking fault energy; for details see Ref. [33].

3.2. Evolution of the deformation structure

The evolution of the deformation structure is investigated at several deformation stages by TEM, EBSD and ECCI. The grain area fraction and the average size of dislocation substructures are shown in Table 1.

3.2.1. Deformation stage: 0.05 true strain/450 MPa

At this deformation stage, the slip character is planar, resulting in dislocation configurations such as pile-ups, dipole bundles, multipoles, hexagonal dislocation networks and Lomer–Cottrell locks (Figs. 2 and 3). Fig. 2a shows a weak-beam TEM image of a dipole bundle lying parallel along the $(-11-1)$ plane. The bundle consists of an array of dislocation dipoles with an average spacing of 20 nm. At this strain level, multipole configurations formed by highly ordered arrays of dipole bundles are observed, as illustrated in the weak-beam TEM image of Fig. 2b. The closed ends of the multipoles are aligned along the intersection line of the primary and cross-slip planes. In particular, the multipole configuration shown in Fig. 2b is aligned along the (-111) plane. These dislocation configurations are commonly observed in the early hardening stages of low stacking fault energy fcc metals [34–36]. The formation of such dislocation configurations, namely, dipole bundles and multipoles, involves dislocation maneuvers that require the activation of dislocation cross-slip [37].

We also observe the formation of more complex planar dislocation configurations, such as dislocation nodes, hexagonal dislocation networks and Lomer–Cottrell locks (Fig. 3). Most of the dislocation nodes observed (N: nodes, Fig. 3a), correspond to triple nodes which are formed by the interaction of dislocations gliding on coplanar systems [38]. Hexagonal dislocation networks (Fig. 3b) are generally formed by the interaction of two types of nodes, namely, extended and contracted nodes [38]. In particular, the formation of hexagonal networks enables the transformation of dislocation pile-ups into planar dislocation structures. Under the current diffraction conditions, $g = 200$ (g is the diffraction vector), the partial dislocations are not visible whereas the stacking faults associated with

Table 1

Evolution of the grain area fraction and the average size of the different types of dislocation substructures with true strain (see also Figs. 5, 6 and 9).

True strain	True stress (MPa)	Area fraction	Taylor lattice size (nm)	Area fraction	Cell size (nm)	Area fraction	Cell block size (nm)
0.1	710	$\sim 100\%$	450 ± 80	–	–	–	–
0.2	950	–	–	15%	195 ± 50	85%	270 ± 70
0.3	1150	–	–	10%	180 ± 40	90%	220 ± 50
0.57	1650	–	–	Not measured	110 ± 20	Not measured	Not measured

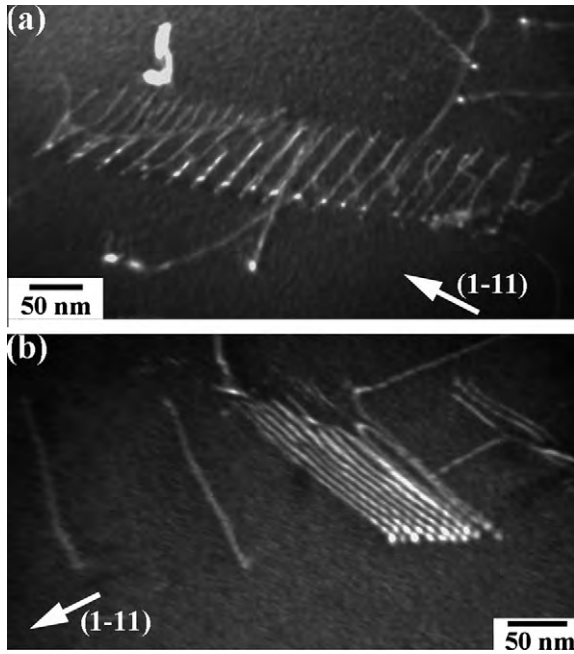


Fig. 2. Weak-beam TEM images of dislocation configurations in a sample deformed to 0.05 true strain/450 MPa: (a) dipole bundle lying parallel along the $(-1\ 1\ -1)$ plane, (b) multipole configurations of edge dislocations. Diffraction vectors are indicated by an arrow.

them are visible. Fig. 3c shows an area containing Lomer–Cottrell (LC) locks. These dislocation configurations are formed by the interaction of dissociated dislocations provided that the leading $\langle 112 \rangle$ partials attract one another. The dislocation product is a $\langle 110 \rangle$ sessile dislocation lying on $\{001\}$ planes. In particular, this figure reveals Lomer–Cottrell dislocations appearing as straight dislocations lying along the $[1-10]$ crystallographic direction and forming Lomer–Cottrell locks (labeled as LC1 and LC2). These locks act as strong barriers to dislocations with slip directions $[101]$ and $[10-1]$. Lomer–Cottrell locks are known to be one of the most important barriers to dislocation glide in stage II hardening of fcc metals [38–40].

3.2.2. Deformation stage: 0.1 true strain/710 MPa

The dislocation structure at this deformation stage is characterized by planar dislocation arrays formed by Taylor lattices and HDDWs (Figs. 4 and 5). Slip bands consisting of pile-up dislocations gliding along the primary slip system and crossing through the grain interior are visible (Fig. 4a). These slip bands contain different average dislocation densities indicating the localization of plasticity along the primary slip system. As secondary slip proceeds, such dislocation configurations transform into dense dislocation networks of planar dislocation arrays forming the so-called Taylor lattices [41] (Fig. 4b). In particular, this figure shows an example of a Taylor lattice formed by two non-coplanar slip systems. These dislocation structures are characteristic of metals with pronounced planar slip [41–43]. Fig. 4c shows an area containing HDDWs along the primary slip system nucleated at a grain boundary

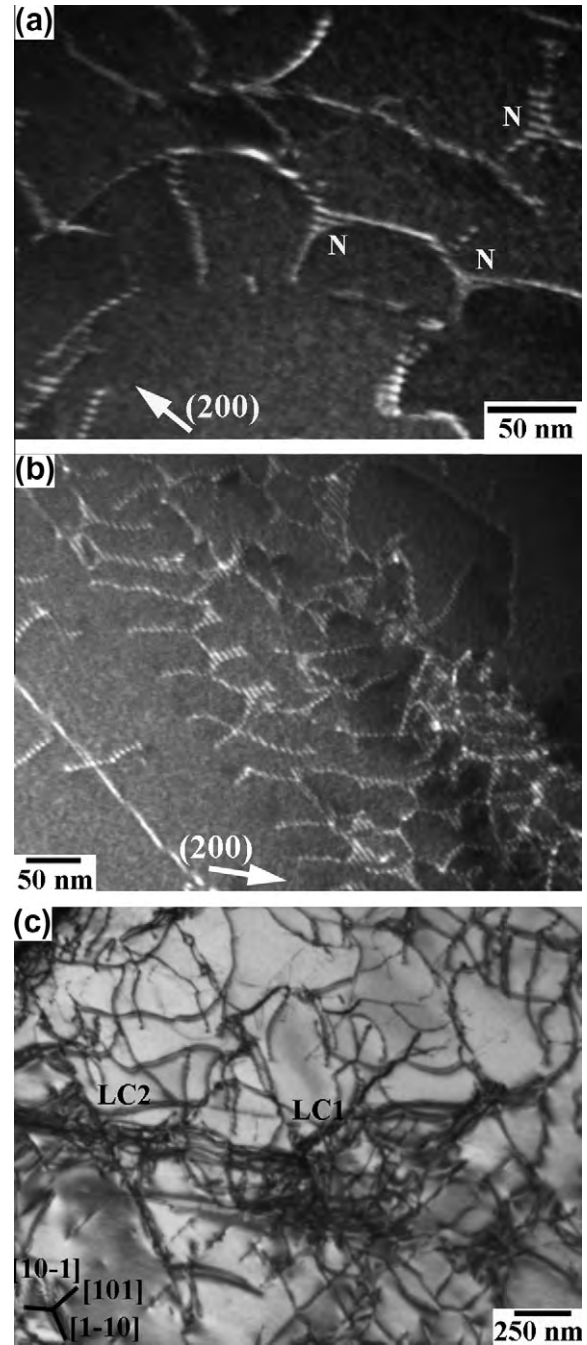


Fig. 3. Extended planar dislocation configurations in a sample deformed to 0.05 true strain/450 MPa: (a) dislocation nodes (N), (b) hexagonal dislocation networks. The stacking faults associated to the partial dislocations are visible. Diffraction vectors are indicated by an arrow. (c) Lomer–Cottrell locks (LC1 and LC2). Lomer–Cottrell dislocations appear as straight dislocations lying along the $[1-10]$ direction.

(GB). These structures are viewed in edge-on position with the $(-1\ -1\ 1)$ reflector parallel to the dislocation walls. The weak alternating contrast between adjacent volumes delimited by HDDWs indicates the small misorientation of the dislocation walls ($<1^\circ$), as revealed by the corresponding diffraction pattern. The weak-beam TEM image of Fig. 4d reveals that HDDWs are formed by dense disloca-

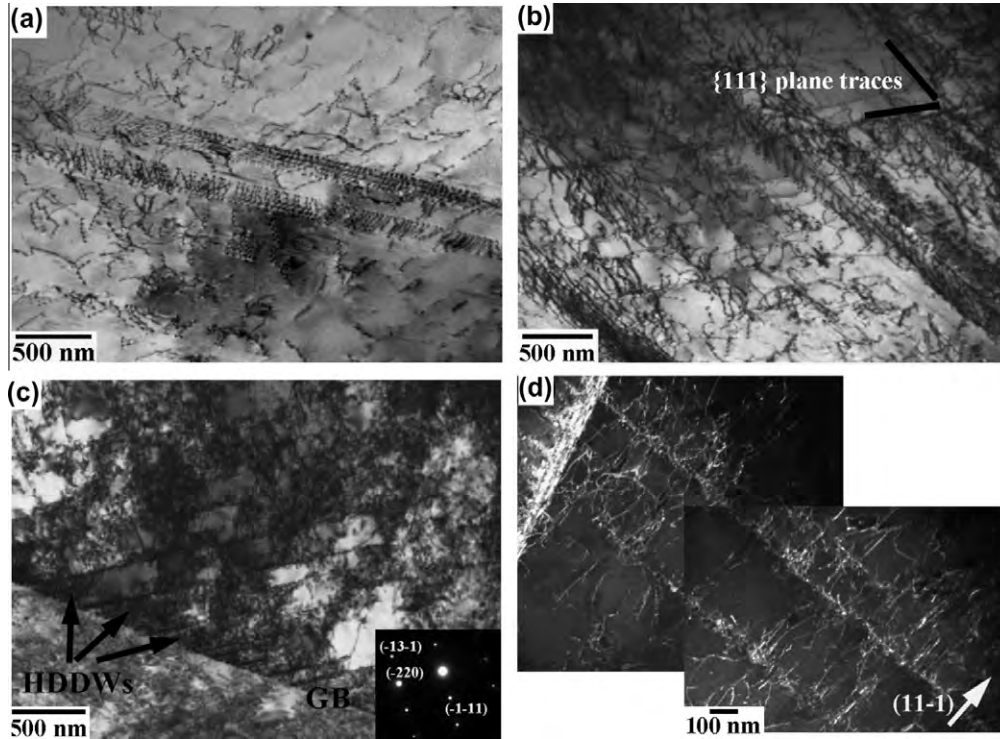


Fig. 4. Dislocation configurations in a sample deformed to 0.1 true strain/710 MPa: (a) slip bands consisting of pile-up dislocations gliding along the primary slip system and crossing through the grain interior, (b) Taylor lattices formed by two non-coplanar slip systems, (c) HDDWs formed along the primary slip system nucleated at a grain boundary (GB), (d) weak-beam TEM image of HDDWs at high magnification. Diffraction vector is indicated by an arrow.

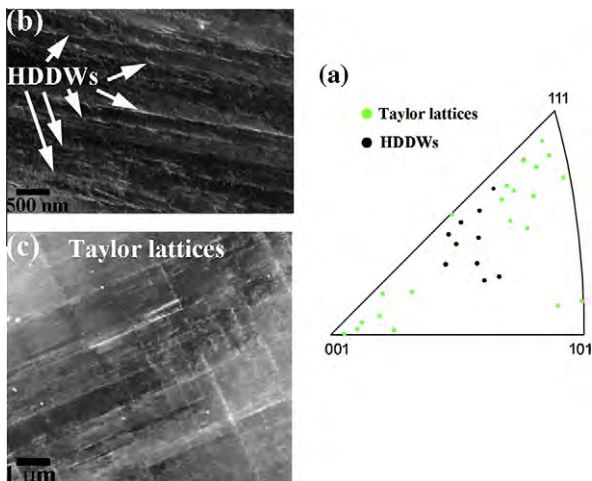


Fig. 5. (a) Inverse pole figure along the tensile axis direction showing experimental grain orientations of a sample deformed to 0.1 true strain/710 MPa (green dots: Taylor lattices; black dots: HDDWs), (b) and (c) ECCI images of HDDWs and Taylor lattices, respectively. (For interpretation of the references to color in this figure legend, the reader is referred to the web version of this article.)

tion sheets lying on the primary slip system. These dislocation structures are spaced between 100 and 300 nm.

The crystallographic orientation dependence of the dislocation patterns, namely, Taylor lattices and HDDWs, was investigated by combined EBSD and ECCI in 30 individual grains (Fig. 5). Fig. 5a shows the inverse pole figure

along the tensile axis direction showing experimentally investigated grain orientations of a sample deformed to 0.1 true strain. Green and black dots correspond to Taylor lattices (green) and HDDWs (black), respectively. The crystal orientations of the grains analyzed represent the crystallographic texture of the material. HDDWs and Taylor lattices (Fig. 5b and c, respectively) are imaged by ECCI as dislocation configurations delimited by dense dislocation sheets which appear as bright straight compact layers due to the electron channeling mechanism and the Bragg diffraction conditions used to image the dislocation structures. Taylor lattices were the most frequently observed dislocation structures with an average size of 450 ± 80 nm. Apparent Taylor lattice sizes were measured from ECCI images and corrected values were then determined by means of a stereological correction considering the corresponding tilting conditions. HDDWs were mostly observed in grains favorably oriented to single slip. Those grains oriented closer to $\langle 111 \rangle // TA$ directions develop a complex dislocation structure formed by HDDWs and Taylor lattices.

3.2.3. Deformation stage: 0.2 true strain/950 MPa

This deformation stage is characterized by the following features: the dislocation substructure consists of planar and wavy dislocation configurations with strong crystal orientation dependence. Further, deformation twinning is activated but at the present deformation stage its activity is

very low (twin area fraction is below 0.01). Specifically, Taylor lattices transform into cell blocks (CBs) and dislocation cells (DCs). CBs are dislocation structures delimited by HDDWs which are subdivided by dislocation walls

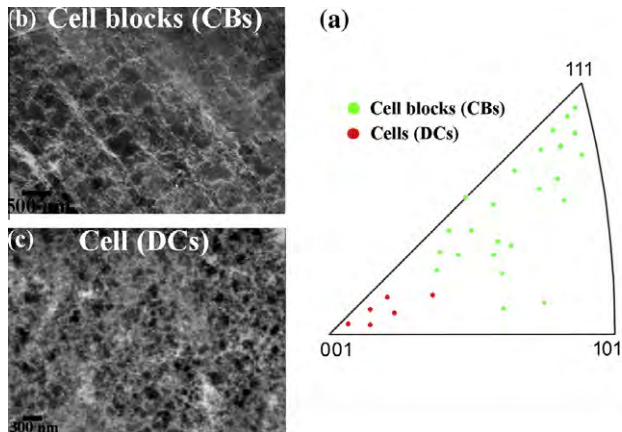


Fig. 6. (a) Inverse pole figure along the tensile axis direction showing experimental grain orientations of a sample deformed to 0.2 true strain/950 MPa (red dots: cells (DCs); green dots: cell blocks (CBs)), (b and c) ECCI images of CBs (b) and DCs (c), respectively. (For interpretation of the references to color in this figure legend, the reader is referred to the web version of this article.)

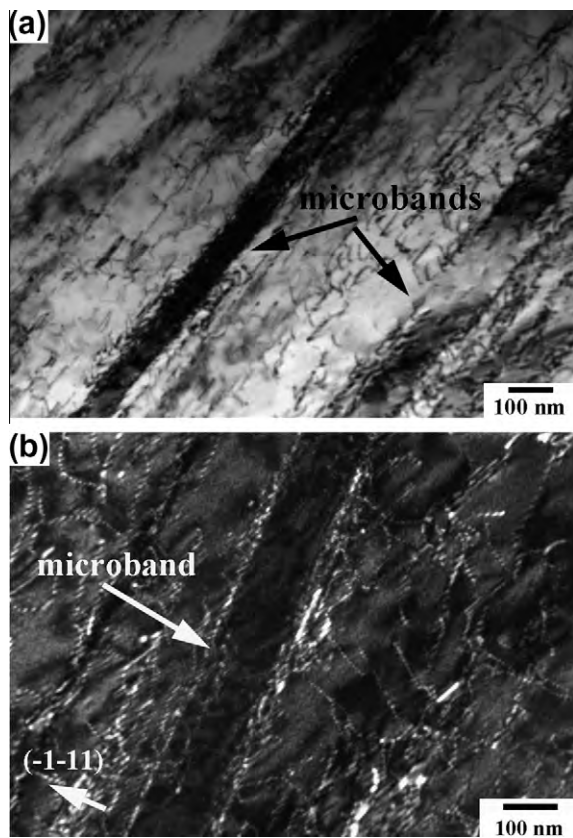


Fig. 7. (a) Bright-field TEM image of an area containing microbands in a sample deformed to 0.2 true strain/950 MPa, (b) weak-beam TEM image of a microband revealing details of the dislocation configuration. Diffraction vector is indicated by an arrow.

formed by statistical dislocation trapping (incidental dislocation boundaries [44]). These dislocation structures are imaged by ECCI as bright compact parallel layers (HDDWs) subdivided by finer bright layers (dislocation walls) (Fig. 6b). At the present strain level, $\sim 85\%$ of the grains contain CBs with an average size of 270 ± 70 nm. The activation of wavy slip enables the formation of equiaxed DCs similar to those observed in medium-to high stacking fault energy metals [4,29,45,46]. These dislocation substructures are imaged by ECCI as bright globular structures with a sharp boundary contrast (Fig. 6c). The area fraction of grains containing cells is $\sim 15\%$ and the average cell size is 195 ± 50 nm. Fig. 7a illustrates an area containing microbands. No detailed quantification was performed since the number of microbands observed at 0.2 true strain was very low. As the weak-beam TEM image of Fig. 7b reveals, microbands are thin dislocation configurations formed by a pair of dislocation sheets of ~ 100 nm in thickness. The dislocation activity in the microband interior is very low compared to that in the matrix. This indicates a strong localization of deformation at the microband walls.

The crystallographic orientation dependence of the dislocation patterns, namely, cell blocks and cells, was investigated by combined EBSD and ECCI in 30 individual grains with a representative orientation distribution that matches the overall texture (Fig. 6a). This figure shows the inverse pole figure along the tensile axis direction showing the grain orientations that were studied in a sample deformed to 0.2 true strain. Green and red dots correspond to CBs (green) and DCs (red), respectively. The data indicate that cell patterning has strong crystal orientation dependence. Equiaxed cells are only developed in grains oriented close to $\langle 001 \rangle // \text{TA}$ directions (Fig. 6c). The remaining grains analyzed contain a well-developed cell block structure (Fig. 6b). The shape of such structures depends on the number of active slip systems.

3.2.4. Deformation stage: 0.3 true strain/1150 MPa

The main characteristic of this deformation stage is the increasing twinning activity resulting in a well-defined twin



Fig. 8. Large view field ECCI image of deformed sample to 0.3 true strain/1150 MPa showing a multiple twin structure with dislocation substructures.

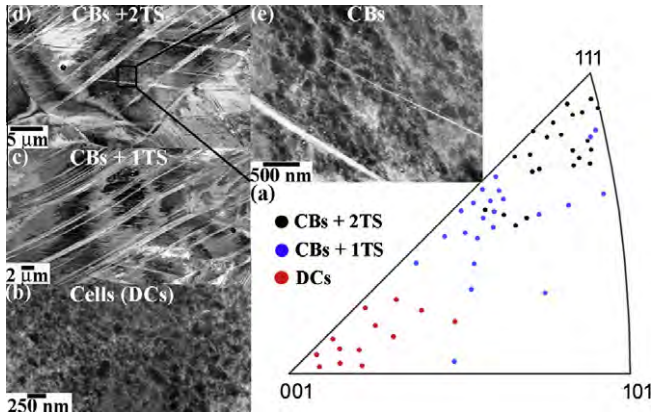


Fig. 9. (a) Inverse pole figure along the tensile axis direction showing experimental grain orientations of a sample deformed to 0.3 true strain/1150 MPa (red dots: cells (DCs); blue dots: cell blocks plus one twinning system (CBs + 1TS); black dots: cell blocks plus two twinning systems (CBs + 2TS)), (b–e) ECCI images of corresponding dislocation and twin substructures. (For interpretation of the references to color in this figure legend, the reader is referred to the web version of this article.)

substructure (Fig. 8). At this deformation stage, $\sim 2/3$ of the grains contain deformation twins that are active on several twinning systems. The grain orientation dependence of the deformation structure was analyzed by combined EBSD and ECCI in 60 individual grains (Fig. 9). The data reveal that we can systematically distinguish three types of grains. The first group consists of grains that are characterized by a dislocation cell structure with low deformation twinning activity (Fig. 9b). These grains contain an area fraction of $\sim 10\%$ and are oriented close to $\langle 001 \rangle // TA$ directions within an angular range of $\sim 15^\circ$ (red dots in Fig. 9a). The average cell size in these grains is 180 ± 40 nm and their shapes depend on the number of slip systems activated. The closer the grain is oriented to $\langle 001 \rangle // TA$ directions the more equiaxed is the cell shape. The second group assembles grains that contain combined dislocation and twin substructures formed by dislocation cell blocks and lamellar twin structures (Fig. 9c). The area fraction of these grains is $\sim 30\%$. They are oriented close to $\langle 112 \rangle // TA$ directions within an angular range of $\sim 15^\circ$ (blue dots in Fig. 9a). The third group contains grains which build up a complex deformed structure consisting of dislocation cell blocks and multiple-twin substructures (Fig. 9d and e). These grains, which are oriented close to $\langle 111 \rangle // TA$ directions within an angular range of $\sim 15^\circ$ (black dots in Fig. 9a), are the most frequent grains with an area fraction of $\sim 60\%$. At 0.3 true strain, the average cell block size in grains oriented close to $\langle 111 \rangle // TA$ or $\langle 112 \rangle // TA$ directions is 220 ± 50 nm. Deformation twins are typically arranged in bundles with thicknesses between 100 and 500 nm (Fig. 10a). These bundles are formed by thin deformation twins with thicknesses ranged between 10 and 50 nm (Fig. 10b). This twin configuration is typical of high-Mn steels [4,8,17,27]. ECCI and TEM observations reveal that at 0.3 true strain, the number of microbands remains very low. Fig. 11 shows an example of an area con-

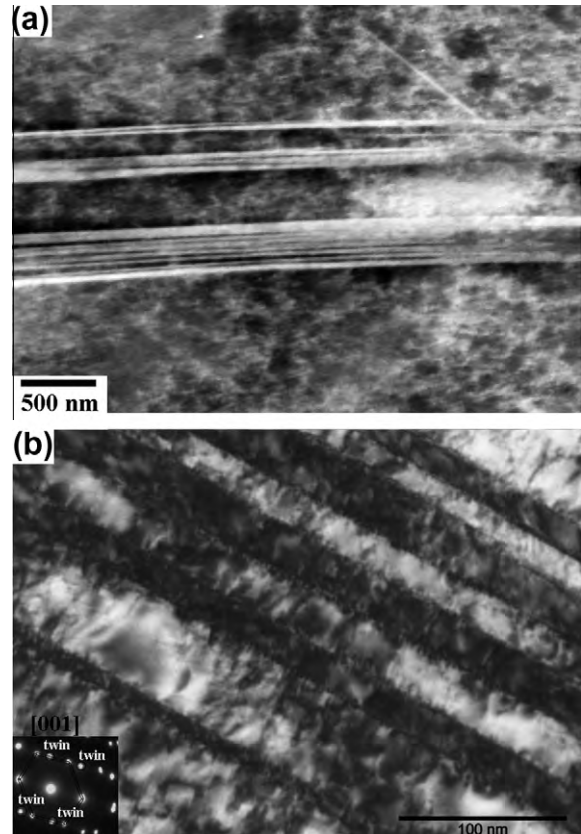


Fig. 10. (a) ECCI image of a bundle of twins in a sample deformed to 0.3 true strain/1150 MPa, (b) detail of a bundle of deformation twins showing single twins with nanometer thickness. Deformation twins are imaged edge-on. The BF-TEM image was obtained close to the zone axis $[001]$. Reflections from twins are indicated in the corresponding diffraction pattern.

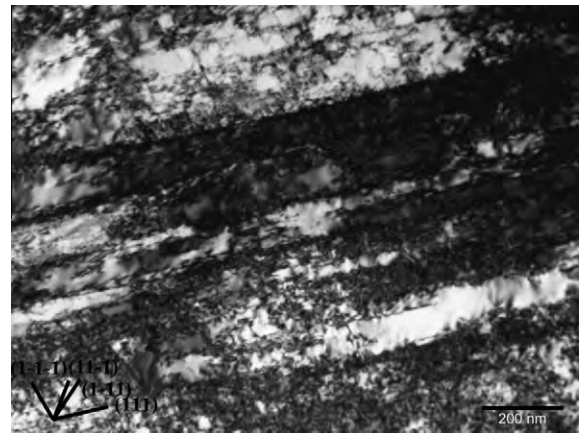


Fig. 11. TEM image of a grain oriented close to the $[-379]$ crystallographic direction in a sample deformed to 0.3 true strain/1150 MPa. Microbands are formed along the $\{111\}$ planes with the highest Schmid factors ($-0.5: \langle 1-11 \rangle (111)$; $-0.4: \langle 1-10 \rangle (111)$).

taining microbands. The grain is oriented close to the $[-379]$ crystallographic direction. Microbands are formed along $\{111\}$ planes which correspond to the slip plane with the highest Schmid factors ($-0.5: \langle 1-11 \rangle (111)$; $-0.4:$

$\langle 1-10 \rangle$ (111)). This image reveals that most of the deformation activity is localized along these slip systems.

4. Discussion

4.1. Dislocation substructure

The FeMnAlC steel exhibits a pronounced evolution in the dislocation configuration upon deformation. We attribute this to the role of solute carbon on dislocation maneuvers. At the early stages of deformation (<0.1 true strain), the formation of dislocation configurations such as pile-ups, multipoles, HDDWs and Taylor lattices indicate strong planar slip character. HDDWs are mainly observed in grains oriented favorably to coplanar or single slip whereas multiple-slip tends to form a homogeneous Taylor lattice structure. Planar slip is promoted in fcc metals by decreasing the stacking fault energy (SFE), increasing the frictional stress due to solute content and the occurrence of short range ordering (SRO) [47,48]. In the FeMnAlC steel studied here, the addition of aluminum and carbon may significantly increase the SFE. To evaluate this effect, we have estimated the SFE at room temperature by means of a modified Olson–Cohen thermodynamical model [14,49]. This approach has been widely applied to high-Mn alloys [3,6,9,15,18,50,51]. In particular, Jin et al. [9] have recently shown that in the FeMnAlC system, the thermodynamical approach provides similar SFEs than those obtained by conventional X-ray diffraction methods. Using thermodynamical data available for the FeMnAlC system [3,9,14,50,52], we estimate a SFE of 63 mJ m^{-2} for the Fe–30.5Mn–2.1Al–1.2C (wt.%) alloy. Magnetic effects were not considered in the present calculation because austenite is paramagnetic at room temperature [53]. This value is close to the reported SFE of 50 mJ m^{-2} in a Fe–31Mn–2.7Al–1.0C (wt.%) alloy [21]. The estimated SFE is similar to that of metals exhibiting non-planar slip character, such as copper [54]. Accordingly, the planar slip character in the alloy studied here cannot be ascribed to the SFE. Detailed observations of TEM diffraction patterns did not reveal diffuse scattering, as would be indicative of short range ordering. We therefore conclude that the planar slip character in the present alloy can be mainly associated to frictional stress effects. Among the different solute species in the present alloy, namely, manganese, aluminum and carbon, the latter provides the strongest dislocation–solute interaction [55]. We can therefore expect a frictional stress effect due to the high carbon content of the present alloy (1.2 wt.%). High frictional stresses have been already reported in high-Mn steels containing the half amount of carbon [56].

With further deformation, 0.2 true strain, wavy slip is remarkably observed, leading to the formation of characteristic dislocation configurations such as cells (DCs) and cell blocks (CBs). DCs are build up in grains when a high number of slip planes are activated and dislocation cross-slip is significantly enabled [43,57], namely, in grains ori-

ented close to $\langle 001 \rangle // \text{TA}$ directions. Grains containing a limited number of active slip systems tend to form CBs. In particular, multiple-slip enables the formation of non-crystallographic dislocation boundaries (i.e. grains oriented close to $\langle 111 \rangle // \text{TA}$ directions) whereas single or coplanar slip tends to produce planar boundaries on crystallographic slip planes (crystallographic dislocation boundaries) [58]. DCs and CBs have been reported in tensile deformed medium-to-high stacking fault energy metals such as copper and aluminum [54,59]. However, the macroscopic stress required to form such dislocation structures in the present FeMnAlC steel, 950 MPa, is much higher than that observed in medium-to-high stacking fault energy metals with similar average grain sizes ($\sim 100 \text{ MPa}$ [60]).

At the present low deformation temperature (room temperature), cell formation is controlled by dislocation cross-slip due to the low activity of dislocation climb. Cross-slip plays an important role in the cell formation through the re-arrangement of screw dislocations in terms of the activation of secondary slip and annihilation of screw dislocations of opposite sign. The localized maneuvers of partial dislocations to transfer dislocation screw segments from one plane to another depend on the SFE [61,62]. However, as the SFE of the alloy studied here is high ($\sim 60 \text{ mJ m}^{-2}$), this means that there is another microstructure parameter having a strong influence on the cross-slip frequency. As the FeMnAlC steel is austenitic, i.e. fcc, we assume the Fridel–Escalaig model of dislocation cross-slip to be applied [63,64]. This model describes the dislocation configuration required for a dissociated screw dislocation to cross-slip into a $\{111\}$ slip plane. According to the Fridel–Escalaig model, this event is determined by the energy required for the recombination or constriction of the two Shockley partials into the cross-slip plane, which is strongly dependent on the stress component acting on the edge parts of the partials. As these partials may interact with a surrounding solute atom field, we therefore expect a significant influence of the carbon field on the constriction energy of cross-slip in the FeMnAlC alloy. Andrews et al. have recently calculated the dependence of the constriction energy on size misfit, modulus mismatch and solute concentration for a screw dislocation in an fcc metal in the presence of a solute field, in particular carbon [65]. The results show that the dislocation–solute field interaction has a strong positive contribution to the total constriction energy. In other words, the presence of a carbon field strongly hinders dislocation cross-slip in fcc metals. In the present FeMnAlC alloy, the high carbon content in solid solution (1.2 wt.%) delays the formation of dislocation structures assisted by cross-slip and shifts them to high macroscopic stress levels. It is worth mentioning that this effect is strongly dependent on the carbon content in solid solution. In particular, we have not observed such effect in a tensile deformed Fe–22Mn–0.6C (wt.%) steel where cells are formed at a lower stress level than in the FeMnAlC steel ($\sim 300 \text{ MPa}$ [4]).

4.2. Strain hardening

The strain hardening behavior of the Fe–30.5Mn–2.1Al–1.2C (wt.%) alloy in solid solution state is characterized by a multiple-stage behavior. In contrast, conventional high-Mn steels containing average grain sizes similar to that obtained in the alloy studied here (50 μm) typically exhibit a single hardening stage associated with a high overall strain hardening (the so-called twinning-induced plasticity, TWIP, effect) [4,6,8,9,12,23]. It is worth pointing out that variations in the strain hardening behavior due to grain size [8,23] or strain rate effects can be found [66]. Stage A hardening is characterized by a decrease in the strain hardening rate. TEM observations reveal that this stage contains dislocation configurations similar to those found in stage II hardening of low stacking fault energy fcc metals, namely, multipoles, dipoles, hexagonal networks and Lomer–Cottrell locks. The low activity of cross-slip suggests that dynamic recovery processes such as annihilation of screw dislocations are limited. Accordingly, this stage can be associated to dislocation hardening, mainly by Lomer–Cottrell locks, and reduced dynamic recovery. The microstructure observations indicate that stage B is associated to dislocation substructure hardening via Taylor lattices. This hardening mechanism is typically observed in materials with pronounced planar slip behavior [43,45,67]. The value of the strain hardening coefficient observed in this regime, $G/27$, is remarkably higher than the typical value of $G/200$ observed for multiple slip in common fcc metals [33,40]. However, it is similar to the hardening coefficient ascribed to dislocation substructure hardening found in FeMnC alloys ($G/20$ – $G/40$ [4,68,69]). With further deformation, the dislocation substructure evolves from Taylor lattices to cells (DCs) and cell blocks (CBs). The limited refinement of the size of the dislocation substructure and the significant activation of dislocation cross-slip lead to a decrease in the strain hardening, stage C.

Fig. 12 shows the variation of the average size of dislocation substructures, namely, Taylor lattices and CBs

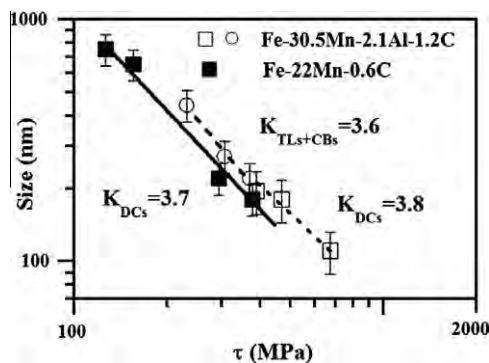


Fig. 12. Variation of the average size of dislocation substructures with flow stress in a Fe–30.5Mn–2.1Al–1.2C (wt.%) steel (white dots: Taylor lattices (TLs) and cell blocks (CBs); white squares: cells (DCs)) and a Fe–22Mn–0.6C (wt.%) steel (black squares: cells (DCs)). The constant K is calculated from the relationship $\tau = KGb/D$ (see also Figs. 5, 6 and 9).

(white dots), and DCs (white squares), with resolved flow stress, τ . Error bars of the average size of dislocation substructures obtained from the statistical treatment of the data are included. We use the microstructure parameters shown in Table 1. For comparison, we also include the evolution of the average cell sizes upon tensile deformation of a Fe–22Mn–0.6C (wt.%) alloy containing a similar average grain size than the alloy studied here [4]. τ was obtained from σ/M , where σ is the macroscopic applied stress and M is the corresponding Taylor factor estimated from the texture ($M = 2.44$ for cell-forming crystals, i.e. grains oriented $\langle 001 \rangle // \text{TA}$ directions, and M is ranged between 2.8 and 3.1 for non cell-forming crystals). This figure reveals that both types of dislocation substructures, viz. Taylor lattices and CBs, and DCs follow a relationship:

$$\tau = KGb/D \quad (1)$$

where τ is the resolved flow stress, G is the shear modulus, K is a constant, b is the magnitude of the Burgers vector and D is the dislocation substructure size. This is a widely observed empirical relationship that has been well established and confirmed in the framework of the mesh-length theory of work hardening [43,67]. Using $b = 2.5 \times 10^{-10}$ m [70] and $G = 70$ GPa [32], we obtain a value of the constant K of 3.6 for Taylor lattices and CBs, $K_{TLs+CBs}$, and 3.8 for DCs, K_{DCs} . Interestingly, these values are very close to that obtained for DCs in the Fe–22Mn–0.6C alloy, $K_{DCs} = 3.7$. Two important conclusions can be drawn from these findings. First, the sizes of the different types of dislocation substructures present in the FeMnAlC steel, namely, Taylor lattices, CBs, and DCs follow the same stress dependence. Second, this stress dependence is practically the same as that obtained for cell-forming crystals free of twins in a Fe–22Mn–0.6C steel. These results reveal that the specific dislocation mechanisms involved in the formation of the different dislocation substructures, in particular, dislocation cross-slip, determine the type of dislocation substructure, viz. Taylor lattices, CBs or DCs. The size of such dislocation substructures scales inversely with the applied resolved stress.

In order to yield a better understanding of the influence of the dislocation substructure on strain hardening, we have evaluated its contribution to the flow stress, $\Delta\sigma$, at different strain levels, specifically, between 0.1 and 0.3 true strain, by means of Eq. (1) and the relationship $\sigma = M\tau$, where M is the Taylor factor. We use the microstructure parameters shown in Table 1, the values of M , b and G used in Fig. 12, and the constants K previously calculated. Fig. 13 shows the calculated stresses from Eq. (1) together with the overall flow stress. Error bars of the stresses calculated from the statistical distribution of the dislocation substructure size, D , is included. This figure reveals that the calculated stresses follow the same evolution with strain as the experimental flow stress. The difference in the absolute stress values, $\sigma - \Delta\sigma$, is constant. We ascribe this stress, ~ 300 MPa, to the frictional stress. We expect a value of the frictional stress close the yield stress (420 MPa) in the

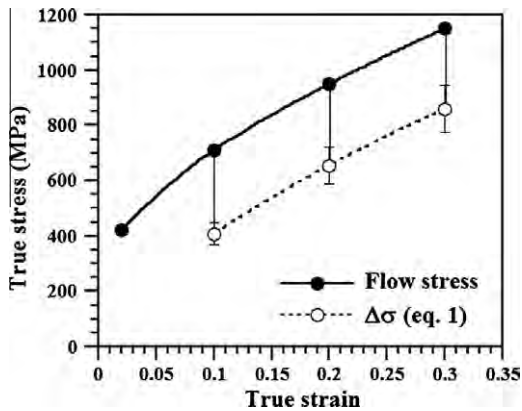


Fig. 13. Contribution of the dislocation substructure to the flow stress calculated from Eq. (1) (white dots) and overall flow stress (black dots) in the strain range 0.1–0.3 true strain (see also Figs. 5, 6 and 9).

present alloy due to the large grain size (50 μm). This analysis indicates that within the strain regime between 0.1 and 0.3 true strain, i.e. hardening stages B–C, the main structural parameter that determines the flow stress and the strain hardening is the size of the dislocation substructure.

With further straining, the development of a twin substructure results in a further decrease of the dislocation mean free path (MFP) leading to stages D–E hardening. Twin boundaries act as strong obstacles to dislocation motion serving as efficient sites for dislocation accumulation. The contribution of twinning to hardening can be described by [4,71]:

$$\Delta\sigma_{\text{twinning}} = K_{H-P} / (\lambda_{\text{twin}})^{1/2} \quad (2)$$

where K_{H-P} is a constant and λ_{twin} is the average twin spacing. The crystallographic orientation dependence of the twin substructure is similar to that found in a tensile deformed Fe–22Mn–0.6C (wt.%) alloy [4]: grains with a highly favorable (multiple twin substructure) or unfavorable orientation (no twin substructure) for twinning follow Schmid's law with respect to the macroscopic stress state. The rest of the crystals develop a lamellar twin substructure. These crystals exhibit deviations from Schmid's law which are associated to local stress concentrations at grain boundaries [13].

4.3. Deformation localization: HDDWs and microbands

We observe that the Fe–30.5Mn–2.1Al–1.2C (wt.%) alloy develops dislocation configurations upon straining that are characteristic of deformation localization phenomena, such as HDDWs and microbands (Figs. 4c and d, 5b and 7). These dislocation arrangements are characterized by a high dislocation activity along the primary slip system resulting in parallel dense dislocation arrays containing low dislocation densities in their interiors. As Fig. 5 shows, these dislocation configurations are mainly formed in grains oriented favorably to single or coplanar slip. Under the current tensile deformation, a typical α -fiber, character-

ized by two strong texture components, namely, $\langle 111 \rangle // \text{TA}$ and $\langle 001 \rangle // \text{TA}$, is formed. Multiple slip is activated in these orientations and, hence, the number of grains containing HDDWs and microbands is low, in agreement with TEM and ECCI observations. Recently, it was proposed that microbanding can account for the good combination of strength and ductility in FeMnAlC steels [3,25,26] (the so-called microband-induced plasticity, MBIP). Yoo et al. have reported the formation of Taylor lattices, deformation bands and microbands upon tensile deformation in a Fe–28Mn–10Al–1.0C (wt.%) steel in solid solution state [3,25]. Based on their TEM observations, these authors attributed the high strain hardening to the formation of deformation bands and microbands. As the previous section shows, the FeMnAlC steel studied here exhibits a high strain hardening due to its specific dislocation substructure, namely, Taylor lattices, dislocation cells and cell blocks, and not due to microbands. In the present case, due to texture effects, microbanding is not favored during tensile deformation and, hence, plays no role in strain hardening. Also, from a more general point of view, we believe that microbanding plays no substantial role in strain hardening in FeMnAlC steels during tensile deformation: As Figs. 7 and 11 reveal, microbands are formed as a result of intense plastic localization on single or coplanar slip. Dislocation activity on secondary non-coplanar slip systems is limited. Accordingly, we expect from such highly localized microstructure a softening instead of a hardening effect.

4.4. Alloy design of high-Mn steels

In this section we compare the mechanical properties (strength/elongation) of the present FeMnAlC steel to those reported in similar high-Mn steel grades. We only focus on room temperature behavior and the solid solution state. Fig. 14 shows the plot of ultimate tensile strength (UTS) vs. elongation of several high-Mn steel grades obtained from engineering stress–strain curves [1,3,4,6,8,9,18,23,25,72,73]. We have classified the steel grades into medium Mn content, referred to as M–Mn,

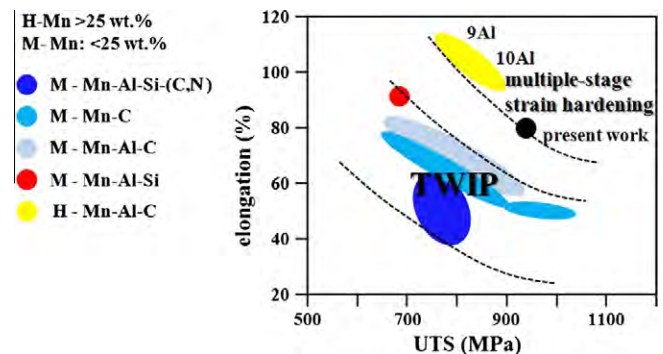


Fig. 14. Ultimate tensile stress (MPa) vs. elongation chart for several high-Mn steel grades. M–Mn: steels with Mn content lower than 25 wt.% Mn; H–Mn: steels with Mn content higher than 25 wt.% Mn. TWIP: twinning-induced-plasticity effect. Chemical composition in wt.%.

as those steels with a Mn content below 25 wt.%, and high Mn content, referred to as H–Mn, as those steels with a Mn content above 25 wt.% Mn. We analyzed results from four M–Mn grades: M–Mn–C [8,9,18,73], M–Mn–Al–C [1,5,6] and M–Mn–Al–Si+(C,N) [4,23,72]. The strain hardening behavior of these steels exhibits the typical twinning-induced plasticity (TWIP) effect, namely, microstructure refinement by deformation twinning. Twin spacing is the key microstructural parameter due to the activation of deformation twinning at low-to-intermediate macroscopic stress values [74,75]. Accordingly, twinning kinetics determine the mechanical properties.

The present H–Mn–Al–C steel presents a superior combination of strength and ductility due to its multiple-stage strain hardening behavior associated to dislocation substructure refinement and subsequent activation of deformation twinning after reaching high stress levels. As the twinning stress, σ_{twinning} , scales with the SFE [76]:

$$\sigma_{\text{twinning}} \sim \gamma/b \quad (3)$$

where γ is the SFE and b is the magnitude of the Burgers vector, a considerable high macroscopic stress is required to promote twinning in the present alloy. This agrees with the outstanding mechanical properties obtained in H–Mn–Al–C alloys with high Al content (9–10 wt.%) [3,25]. These results confirm that the H–Mn–Al–C grade is a promising high performance steel. The key features of the excellent strain hardening behavior of the present steel are as follows. First, the development of a fine dislocation substructure with nanometer size: this is ascribed to the role of carbon solute on dislocation cross-slip. Due to the high carbon content of the H–Mn–Al–C system (~1 wt.%), cross-slip is strongly impeded. As a consequence, its frequency increases with the applied stress, resulting in a gradual transition in the type of dislocation configuration from planar (Taylor lattices) to wavy (cells, cell blocks). This dislocation transition is key to minimizing damage mechanisms triggered by local stress concentrations at grain boundaries provided by dense planar dislocation configurations. Second, the development of a twin substructure at intermediate deformation levels results in a further microstructure refinement (TWIP effect). The good mechanical compatibility between dislocation slip and the evolving twin interfaces results in a critical stress required to transfer plastic deformation across the twin bundle, $\tau_{t\text{-transfer}}$, which is only dependent on the shear modulus, G , and twin thickness t :

$$\tau_{t\text{-transfer}} \sim Gb/t \quad (4)$$

where b is the magnitude of the Burgers vector. This stress is higher than that required to transfer plasticity across a dislocation boundary with low misorientation:

$$\tau_{db\text{-transfer}} \sim Gb(\theta/Db)^{1/2} \quad (5)$$

where D is the dislocation substructure size and θ is the misorientation angle [77,78]. Accordingly, the strength of the twin interface is higher than that of a dislocation

boundary against dislocation glide. In other words, the effect of twinning on the flow stress is higher than that of dislocation substructure refinement. The present study indicates that multiple-stage strain hardening due to size refinement of the dislocation substructure and the subsequent activation of deformation twinning, which leads to a steady increase of strain hardening, promotes an enhanced combination of strength and ductility.

5. Conclusions

We investigated the underlying kinetics of the deformation structure evolution and its contribution to the strain hardening of a Fe–30.5Mn–2.1Al–1.2C (wt.%) steel during tensile deformation by means of TEM and ECCI combined with EBSD. The following conclusions are drawn:

- The present steel exhibits a superior combination of strength and ductility (ultimate tensile strength of 1.6 GPa and elongation to failure of 55%) due to the multiple-stage strain hardening behavior associated to dislocation substructure refinement and subsequent activation of deformation twinning, which leads to a steadily increase of the strain hardening.
- The early hardening stage is fully determined by the size of the dislocation substructure, namely, Taylor lattices, cell blocks and dislocation cells. We do not observe the so-called microband-induced plasticity (MBIP) effect. In the present case, due to texture effects, microbanding is not favored during tensile deformation and, hence, plays no role in strain hardening. We further suggest that due to the highly localized nature of microbands, they should rather produce a softening instead of a hardening effect.
- The characterization of dislocation substructure evolution reveals a strong influence of carbon solute on the evolving dislocation substructure. We attribute this effect to the role of carbon on dislocation cross-slip. Due to the strong impediment of cross-slip, its frequency increases with the applied stress, resulting in a gradual transition in the type of dislocation configuration from planar (Taylor lattices) to wavy (cells, cell blocks).
- The specific dislocation mechanisms involved in the formation of the different dislocation substructures, in particular, dislocation cross-slip, determine the resulting type of dislocation substructure, viz. Taylor lattices, cell blocks or cells. The size of such dislocation substructures scales inversely with the applied resolved stress.

Acknowledgements

We gratefully acknowledge the financial support of the German Research Foundation (Deutsche Forschungsgemeinschaft DFG) through the project “SFB-761 – steel ab initio”.

References

- [1] Grässel O, Krüger L, Frommeyer G, Meyer LW. *Int J Plast* 2000;16:1391.
- [2] Scott C, Allain S, Faral M, Guelton N. *Rev Metall* 2006;103:293.
- [3] Yoo JD, Park K-T. *Mater Sci Eng A* 2008;496:417.
- [4] Gutierrez-Urrutia I, Raabe D. *Acta Mater* 2011;59:6449.
- [5] Kim J-K, Chen L, Kim H-S, Kim S-K, Estrin Y, De Cooman BC. *Metall Mater Trans A* 2009;40A:3147.
- [6] Curtze S, Kuokkala V-T. *Acta Mater* 2010;58:5129.
- [7] Idrissi H, Renard K, Schryvers D, Jacques PJ. *Scripta Mater* 2010;63:961.
- [8] Bouaziz O, Allain S, Scott CP, Cugy P, Barbier D. *Current Opinion Solid State Mater Sci* 2011;15:141.
- [9] Jin J-E, Lee Y-K. *Acta Mater* 2012;60:1680.
- [10] Lee S-J, Kim J, Kane SN, De Cooman BC. *Acta Mater* 2011;59:6809.
- [11] Koyama M, Sawaguchi T, Lee T, Lee CS, Tsuzaki K. *Mater Sci Eng A* 2011;528:7310.
- [12] Allain S, Chateau JP, Bouaziz O. *Mater Sci Eng A* 2004;387–389:143.
- [13] Gutierrez-Urrutia I, Zaefferer S, Raabe D. *Mater Sci Eng A* 2010;527:3552.
- [14] Dumay A, Chateau JP, Allain S, Migot S, Bouaziz O. *Mater Sci Eng A* 2008;483–484:184.
- [15] Saeed-Akbari A, Imlau J, Prah U, Bleck W. *Metall Mater Trans A* 2009;40A:3076.
- [16] Shiekhelsouk MN, Favier V, Inal K, Cherkaoui M. *Int J Plast* 2009;25:105.
- [17] Idrissi H, Renard K, Ryelandt L, Schryvers D, Jacques PJ. *Acta Mater* 2010;58:2464.
- [18] Park K-T, Jin KG, Han SH, Hwang SW, Choi K, Lee CS. *Mater Sci Eng A* 2010;527:3651.
- [19] Dastur YN, Leslie WC. *Metall Trans A* 1981;12A:749.
- [20] Zuidema BK, Subramanyam DK, Leslie WC. *Metall Trans A* 1987;18A:1629.
- [21] Shun T, Wan CM, Byrne JG. *Acta Metall Mater* 1992;40:3407.
- [22] Saeed-Akbari A, Mosecker L, Schwedt A, Bleck W. *Metall Mater Trans A* 2012;43A:1688.
- [23] Gutierrez-Urrutia I, Raabe D. *Scripta Mater* 2012;66:992.
- [24] Dancette S, Delannay L, Renard K, Melchior MA, Jacques PJ. *Acta Mater* 2012;60:215.
- [25] Yoo JD, Hwang SW, Park K-T. *Metall Mater Trans A* 2009;40A:1520.
- [26] Park K-T, Kim G, Kim SK, Lee SW, Hwang SW, Lee CS. *Metal Mater Int* 2010;16:1.
- [27] Gutierrez-Urrutia I, Zaefferer S, Raabe D. *Scripta Mater* 2009;61:737.
- [28] Gutierrez-Urrutia I, Raabe D. *Scripta Mater* 2012;66:343.
- [29] Gutierrez-Urrutia I, Raabe D. *Mater Sci Forum* 2012;702–703:523.
- [30] Eisenlohr A, Gutierrez-Urrutia I, Raabe D. *Acta Mater* 2012;60:3994.
- [31] Zhang ZF, Wang ZG. *Prog Mater Sci* 2008;53:1025.
- [32] Kim J, Lee SJ, De Cooman BC. The stacking fault energy of TWIP steels. Seoul: HMnS2011; 2011.
- [33] Kocks UF, Mecking H. *Prog Mater Sci* 2003;48:171.
- [34] Pande CS, Hazzledine PM. *Philos Mag* 1971;24:1039.
- [35] Steffens T, Schwink C, Korner A, Karnthaler HP. *Philos Mag A* 1987;56:161.
- [36] Feaugas X. *Acta Mater* 1999;47:3617.
- [37] Jackson PJ. *Prog Mater Sci* 1985;29:139.
- [38] Nabarro FRN. *Theory of crystal dislocations*. Oxford: Oxford University Press; 1967.
- [39] Hirth JP, Lothe J. *Theory of dislocations*. New York: McGraw-Hill; 1968.
- [40] Nabarro FRN, Basinski ZS, Holt DB. *Adv Phys* 1964;13:193.
- [41] Hughes DA. *Acta Metall Mater* 1993;41:1421.
- [42] Karaman I, Sehitoglu H, Maier HJ, Chumlyakov YI. *Acta Mater* 2001;49:3919.
- [43] Kuhlmann-Wilsdorf D. *Mater Sci Eng A* 1989;113:1.
- [44] Hughes DA, Hansen N, Bammann DJ. *Scripta Mater* 2003;48:147.
- [45] Bay B, Hansen N, Hughes DA, Kuhlmann-Wilsdorf D. *Acta Metall Mater* 1992;40:205.
- [46] Huang X. *Scripta Mater* 1998;38:1697.
- [47] Gerold V, Karnthaler HP. *Acta Metall* 1989;37:2177.
- [48] Hong SI, Laird C. *Acta Mater* 1990;38:1581.
- [49] Allain S, Chateau JP, Bouaziz O, Migot S, Guelton N. *Mater Sci Eng A* 2004;387–389:158.
- [50] Lee Y-K, Choi C-S. *Metall Mater Trans A* 2000;31A:355.
- [51] Nakano J, Jacques PJ. *CALPHAD* 2010;34:167.
- [52] Olson GB, Cohen M. *Metall Trans A* 1976;7A:1897.
- [53] Huang W. *Calphad* 1989;13:243.
- [54] Heino P, Perondi L, Kaski K, Ristolainen E. *Phys Rev B* 1999;60:14625.
- [55] Bhadeshia HKDH, Honeycombe R. *Steels: microstructure and properties*. Oxford: Elsevier; 2006.
- [56] Sevillano JG. *Scripta Mater* 2009;60:336.
- [57] Bay B, Hansen N, Hughes DA, Kuhlmann-Wilsdorf D. *Acta Metall Mater* 1992;40:205.
- [58] Winther G, Jensen DJ, Hansen N. *Acta Mater* 1997;45:5059.
- [59] Schulthess TC, Turchi PEA, Gonis A, Nieh TG. *Acta Mater* 1998;46:2215.
- [60] Kocks UF, Mecking H. *Prog Mater Sci* 2003;48:171.
- [61] Hirth JP, Lothe J. *Theory of dislocations*. Chichester: Wiley; 1982.
- [62] Jackson PJ. *Prog Mater Sci* 1985;29:139.
- [63] Püschl W. *Prog Mater Sci* 2002;47:415.
- [64] Bonneville J, Escaig B. *Acta Metall* 1979;27:1477.
- [65] Andrews SD, Sehitoglu H, Karaman I. *J Appl Phys* 2000;87:2194.
- [66] Rodriguez P. *Metall Mater Trans A* 2004;35A:2697.
- [67] Kuhlmann-Wilsdorf D. *Philos Mag A* 1999;79:955.
- [68] Canadinc D, Sehitoglu H, Maier HJ, Chumlyakov YI. *Acta Mater* 2005;53:1831.
- [69] Canadinc D, Sehitoglu H, Maier HJ. *Mater Sci Eng A* 2007;454–455:662.
- [70] Bouaziz O, Allain S, Scott C. *Scripta Mater* 2008;58:484.
- [71] Asgari S, El-Danaf E, Kalidindi SR, Doherty RD. *Metall Mater Trans A* 1997;28A:1781.
- [72] Huang BX, Wang XD, Wang L, Rong YH. *Metall Mater Trans A* 2007;39A:717.
- [73] Jin J-E, Lee Y-K. *Mater Sci Eng A* 2009;527:157.
- [74] Lu L, Sui ML, Lu K. *Science* 2000;287:1463.
- [75] Yan FK, Liu GZ, Tao NR, Lu K. *Acta Mater* 2012;60:1059.
- [76] Christian JW, Mahajan S. *Prog Mater Sci* 1995;39:1.
- [77] Hughes DA, Hansen N. *Acta Mater* 2000;48:2985.
- [78] Liu B, Raabe D, Eisenlohr P, Roters F, Arsenlis A, Hommes G. *Acta Mater* 2011;59:7125.



Nanoscale austenite reversion through partitioning, segregation and kinetic freezing: Example of a ductile 2 GPa Fe–Cr–C steel

L. Yuan^a, D. Ponge^a, J. Wittig^{a,b}, P. Choi^a, J.A. Jiménez^c, D. Raabe^{a,*}

^a Max-Planck-Institut für Eisenforschung, Max-Planck-Str. 1, 40237 Düsseldorf, Germany

^b Vanderbilt University, Nashville, TN 37235-1683, USA

^c CENIM-CSIC, Avda. Gregorio del Amo 8, 28040 Madrid, Spain

Received 5 July 2011; received in revised form 29 November 2011; accepted 25 January 2012

Available online 2 March 2012

Abstract

Austenite reversion during tempering of a Fe–13.6 Cr–0.44 C (wt.%) martensite results in an ultra-high-strength ferritic stainless steel with excellent ductility. The austenite reversion mechanism is coupled to the kinetic freezing of carbon during low-temperature partitioning at the interfaces between martensite and retained austenite and to carbon segregation at martensite–martensite grain boundaries. An advantage of austenite reversion is its scalability, i.e. changing tempering time and temperature tailors the desired strength–ductility profiles (e.g. tempering at 400 °C for 1 min produces a 2 GPa ultimate tensile strength (UTS) and 14% elongation while 30 min at 400 °C results in a UTS of ~1.75 GPa with an elongation of 23%). The austenite reversion process, carbide precipitation and carbon segregation have been characterized by X-ray diffraction, electron back-scatter diffraction, transmission electron microscopy and atom probe tomography in order to develop the structure–property relationships that control the material's strength and ductility.

© 2012 Acta Materialia Inc. Published by Elsevier Ltd. All rights reserved.

Keywords: Austenite reversion; Partitioning; Diffusion; Strength; Ductility

1. Introduction

A high demand exists for lean, ductile and high-strength Fe–Cr stainless steels in the fields of energy conversion, mobility and industrial infrastructure. As conventional martensitic stainless steels (MSSs) typically exhibit brittle behavior, supermartensitic Fe–Cr stainless steels (SMSSs) with enhanced ductility have been designed in the past years by reducing carbon (<0.03 wt.%) and adding nickel (4–6.5 wt.%) and molybdenum (2.5 wt.%) [1–4]. The heat-treated microstructures of these materials are characterized by tempered martensite and retained austenite [1–4].

In this work we present an alternative approach of designing MSSs with both high strength and high ductility. Our method is based on nanoscale austenite reversion and

martensite relaxation via a modest heat treatment at 300–500 °C for several minutes. We make the surprising observation that this method leads to very high strength (up to 2 GPa) of a Fe–13.6Cr–0.44C (wt.%) steel without loss in ductility (X44Cr13, 1.4034, AISI 420).

Quenching followed by tempering is known to improve the strength and toughness of martensitic steels [5–7]. Specifically, quench and partitioning (Q&P) treatments are efficient for producing steels with retained austenite and improved ductility [8]. The heat treatment sequence for Q&P steel involves quenching to a temperature between the martensite-start (M_s) and martensite-finish (M_f) temperatures, followed by a partitioning treatment either at, or above, the initial quench temperature. Partitioning is typically designed in a way that enriches and stabilizes the retained austenite with carbon from the supersaturated martensite [9]. In conventional Q&P processes, the quench temperature is hence chosen such that some retained austenite prevails and subsequent tempering leads to carbon

* Corresponding author. Tel.: +49 0211 6792 333.

E-mail address: d.raabe@mpie.de (D. Raabe).

partitioning between martensite and austenite. Typically, no new austenite is formed during partitioning.

In our study we modify this approach with the aim to increase the amount of austenite during low-temperature partitioning. We start with austenitization and water quenching to room temperature. This provides a martensitic–austenitic starting microstructure. During a subsequent heat treatment in the range 300–500 °C, austenite reversion [10–15] takes place on the basis of partial partitioning according to local equilibrium, segregation and kinetic freezing of carbon inside the newly formed austenite.

It is important to point out that the phenomena occurring during austenite reversion are in the present case different from conventional Q&P approaches: in Q&P processing, the carbon diffuses from martensite into the already present austenite during tempering where equilibration of the carbon distribution inside the austenite is generally assumed. In the current case of low-temperature partitioning, however, the carbon is enriched in front of the austenite boundary and accumulates there since it has a much higher diffusion rate in body-centered cubic (bcc) than in face-centered cubic (fcc) material. The accumulated carbon at the martensite–austenite interface then provides a high local driving force for austenite reversion. Once captured by the growing austenite, the carbon is kinetically frozen owing to its small mobility in this phase.

The phenomena occurring during austenite reversion in Fe–Cr–C stainless steels are complex due to the high content of carbon and substitutional alloying elements. In contrast to typical Q&P steels where carbide precipitation (M_3C) is suppressed by alloying with Si and/or Al [16], in the present alloy M_3C -type carbide precipitation occurs at 400 °C. This means that a kinetic and thermodynamic competition exists for carbon between austenite reversion, enrichment of retained austenite and carbide formation during tempering.

Therefore, the partitioning temperature must be chosen on a theoretically well founded basis for two reasons: first, low temperature annealing requires more local carbon enrichment to provide a driving force high enough for austenite reversion. We emphasize in this context that the local equilibrium matters for this process, i.e. a high carbon content is required at the martensite–austenite interface (not everywhere within the austenite). Equilibration of the carbon inside the austenite is not necessarily required. Second, high temperature annealing may cause more carbide formation, consuming too much carbon, so that austenite reversion is suppressed due to an insufficient carbon chemical potential to promote it.

In order to elucidate the competing phenomena occurring during such low-temperature partitioning, namely, carbide formation vs. austenite reversion as well as the carbon redistribution inside the retained and reversed austenite fractions, atom probe tomography (APT) was used. This method allows us to measure the carbon content inside the austenite, which determines its stability, as well as inside the martensite and the carbides [17–28]. The

APT method allows for three-dimensional (3-D) elemental mapping with nearly atomic resolution and provides information about internal interfaces and local chemical gradients [28–32].

2. Experimental

The material used in this study was a martensitic stainless steel with the chemical composition Fe–13.6Cr–0.44C (wt.%; 1.4034, X44Cr13, AISI 420), which was provided by ThyssenKrupp Nirosta as a cold rolled sheet, Table 1. The A_{e3} temperature, calculated by Thermo-Calc [33] using the TCFE5 database [34], indicates that the incipient holding temperature for full austenitization should be above 800 °C. The calculation further reveals that full dissolution of chromium carbides in austenite is achieved at ~ 1100 °C. Hence, the annealing conditions were set to 1150 °C for 5 min. Dilatometer tests were performed using a Bähr Dil805 A/D quenching and deformation device to identify the M_s temperature during quenching. After water quenching, tempering at 300, 400 and 500 °C, respectively, with different holding times was performed to study carbon redistribution, austenite reversion and carbide formation (Fig. 1).

Mechanical properties were determined by tensile and Vickers hardness measurements (980N load, HV10). Tensile tests were carried out along the rolling direction of the samples at room temperature. Flat tensile specimens were machined with a cross-section of 2.5 mm \times 8 mm and a gauge length of 40 mm. The tests were conducted on a Zwick/Roell Z100 tensile testing machine at a constant cross-head speed of 1 mm min⁻¹, corresponding to an initial strain rate of 4.2×10^{-4} s⁻¹.

The volume fraction of the austenite phase after heat treatments (carbide dissolution annealing and tempering at 400 °C for 1, 2, 10 and 30 min) was measured by X-ray diffraction (XRD), electron back-scatter diffraction (EBSD) and magnetic characterization (Feritscope MP30E-S).

EBS samples were prepared by standard mechanical grinding and polishing procedures normal to the rolling direction. Subsequently, these samples were electropolished using Struers electrolyte A3 at room temperature using a voltage of 40 V, a flow rate of 20 s⁻¹ and a polishing time of 20 s. EBSD was performed on a JEOL-6500F high-resolution field-emission scanning electron microscope operated at 15 kV [35].

XRD measurements were carried out using Co K α radiation. XRD data were collected over a 2θ range of 30–138°

Table 1
Chemical composition of material used for the investigation (1.4034, X44Cr13, AISI 420).

	C	Cr	Mn	Ni	Si	N	Fe
wt.%	0.437	13.6	0.53	0.16	0.284	0.0205	Bal.
at.%	1.97	14.19	0.52	0.15	0.55	0.079	Bal.

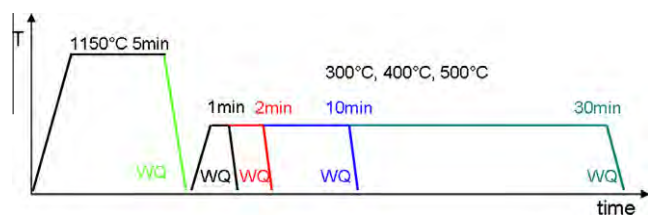


Fig. 1. Schematic diagram of the heat treatment route (WQ: water quenching).

with a step width of 0.05° and a counting time of 10 s per step. The Rietveld method was used for the calculation of the structural parameters from the diffraction data of the polycrystalline bulk materials. We used version 4.0 of the Rietveld analysis program TOPAS (Bruker AXS). The analysis protocol included consideration of background, zero displacement, scale factors, peak breath, unit cell parameter and texture parameters. The room temperature structures used in the refinement were martensite/ferrite and austenite.

Thin foils were prepared using standard twin-jet electropolishing from the as-quenched material and the tempered samples before and after deformation [36]. These samples were examined by transmission electron microscopy (TEM) in a Philips CM 20 at an acceleration voltage of 200 kV to characterize the carbide evolution and the formation of reverted austenite. Carbide characterization was also carried out by using a carbon extraction replica technique [37] and investigated by electron diffraction and energy dispersive spectroscopy (EDS) in the transmission electron microscope.

Needle-shaped APT samples were prepared by applying a combination of standard electropolishing and subsequent ion-milling with a focused-ion-beam (FIB) device. APT analyses were performed with a local electrode atom probe (LEAP™ 3000X HR) in voltage mode at a specimen temperature of ~ 60 K. The pulse-to-base voltage ratio and the pulse rate were 15% and 200 kHz, respectively. Data analysis was performed using the IVAS software (Cameca Instruments).

3. Results

3.1. Mechanical properties

The as-received cold rolled and recrystallized material has an ultimate tensile strength (UTS) of 640 MPa and a uniform elongation of 19%, Fig. 2a. After austenitization at 1150 °C and water quenching, the material is brittle and fails before the yield stress is reached at a stress of 400 MPa (Fig. 2a). Thus, the true UTS for the as-quenched state could be only estimated from the indentation hardness. The relationship between Vickers hardness (HV) and tensile strength was calculated considering a linear relationship of the form $\Delta HV = K \times \Delta UTS$. A constant K of 3.5 was determined by linear regression through data

obtained from the hardness and UTS values obtained from samples after tempering at 400 °C for different times. Fig. 2e suggests that the hardness for the as-quenched state corresponds to a tensile strength of more than 2300 MPa.

Fig. 2a also shows the stress–strain curves obtained from the tensile tests performed on samples tempered at 400 °C for different times. The most remarkable feature of these curves is the transition from a brittle behavior in the as-quenched material to a ductile one after tempering. When the tempering time is increased, we observe an increase in uniform elongation and a decrease in UTS. After 30 min, the uniform elongation of the sample reaches a value of $\sim 22\%$ and a UTS above 1760 MPa. This value for the UTS can be also reached upon tempering at 500 °C, but in this case, a gradual increase in total elongation upon increase in tempering time is not observed, Fig. 2b. It can be observed that in this case the stress does not go through a maximum; that is, σ/ϵ (the partial derivative of the stress with respect to strain) does not go through zero. This would indicate that the sample fractures before the strain reach the necking value. At 300 °C, after 1 min, the ductility improves slightly, i.e. longer tempering is required for obtaining better ductility at this temperature, as shown in Fig. 2c. When comparing the mechanical properties of samples tempered at different temperatures (Fig. 2d), the 400 °C treatment yields the optimum improvement in both UTS and total elongation (TE).

3.2. Phase fractions and kinetics: predictions and experiments

Thermo-Calc was used to calculate the phase equilibrium at the different partitioning temperatures. For evaluating kinetics during heating and cooling, we conducted dilatometer tests (Fig. 3). The heating and cooling rates were set to 10 and -30 K s^{-1} , respectively. Above 876 °C, the microstructure is fully austenitic. The M_s temperatures were derived from the dilatometer tests (118 °C after 1150 °C annealing and 360 °C after 950 °C annealing). The Thermo-Calc calculations were used to predict the equilibrium carbon content of the austenite after annealing at different temperatures (Fig. 3c).

Fig. 4 shows the phase fraction of austenite vs. tempering time for 400 °C measured by feritscope (magnetic signal), EBSD and XRD. For the as-quenched state the EBSD result provides a higher volume fraction (20%) than the magnetic (14.5%) and the XRD data (8%), which is attributed to the limited statistics of the EBSD method. During the first 2 min of tempering the amount of austenite increases rapidly, indicating austenite reversion. After 30 min, nearly 40 vol.% austenite is observed consistently for all three methods.

Fig. 5 shows in situ EBSD observations of the austenite during tempering. Fig. 5a maps the material in the as-quenched state containing only retained austenite. Fig. 5b shows the same area during the in situ experiment containing both retained plus reverted austenite after 5 min

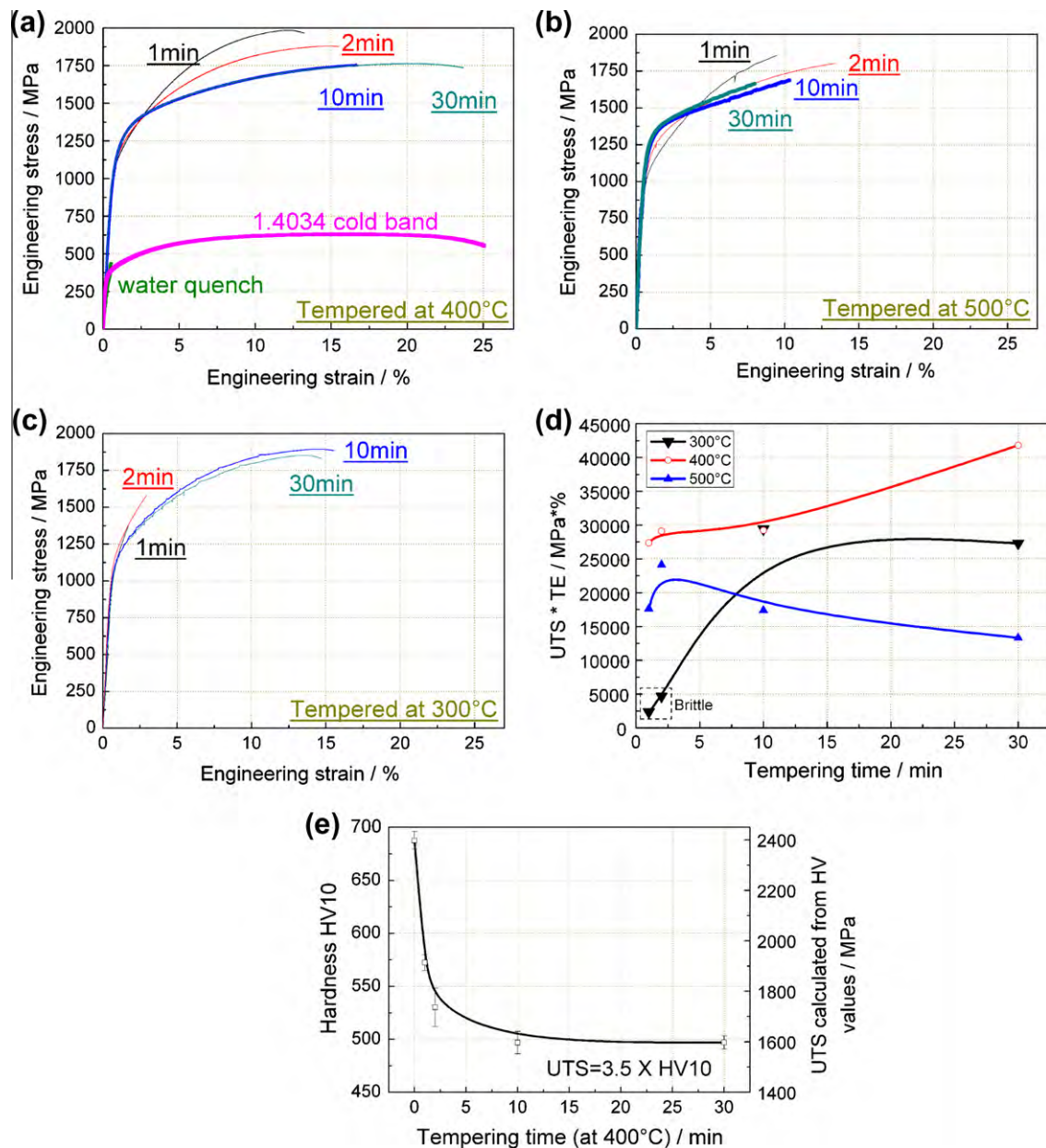


Fig. 2. Mechanical properties of the quenched and partitioned stainless steel Fe-13.6Cr-0.44C (wt.%, 1.4034, AISI 420) after different types of partitioning and austenite reversion treatments. The original state of a commercial alloy (1.4034, cold band) is shown as reference. The term “cold band” refers here to hot rolled, cold rolled and finally recrystallized material. (a–c) Stress–strain curve of samples tempered at 400, 500 and 300 °C, respectively. Note in (a) that the as-quenched sample (green) fails already in the elastic regime. (d) Multiplied quantity UTS × TE as a function of annealing time for the three different temperatures; (e) UTS–HV relationship (UTS: ultimate tensile strength; HV: Vickers hardness; TE: total elongation).

tempering at 400 °C subsequent to the quenching treatment. The EBSD map reveals the fine dispersion of the newly formed reverted austenite after 5 min. We observe two kinds of austenite, namely one with a coarse topology and another one with a fine and dispersed topology.

The microstructures of the samples tempered for 0, 1 and 2 min, respectively, are shown in Fig. 6. The as-quenched material (0 min tempering) is brittle and failed already in the elastic regime during tensile testing. From the microstructure it can be seen (Fig. 6b, left: before tensile test; right: after tensile test, for each state) that only a small amount of austenite was transformed to

martensite when the material failed, i.e. austenite bands can still be observed near the fracture interface. For samples after 400 °C tempering, no premature failure takes place and the total elongation (TE) reaches 14% (engineering strain). The microstructure at the fracture zone shows nearly no remaining austenite. This observation indicates that deformation-driven austenite-to-martensite transformation takes place. Secondary cracks along the tensile direction are visible in the EBSD maps. It seems that these cracks follow the band-like former retained austenite regions, which transformed during straining into martensite.

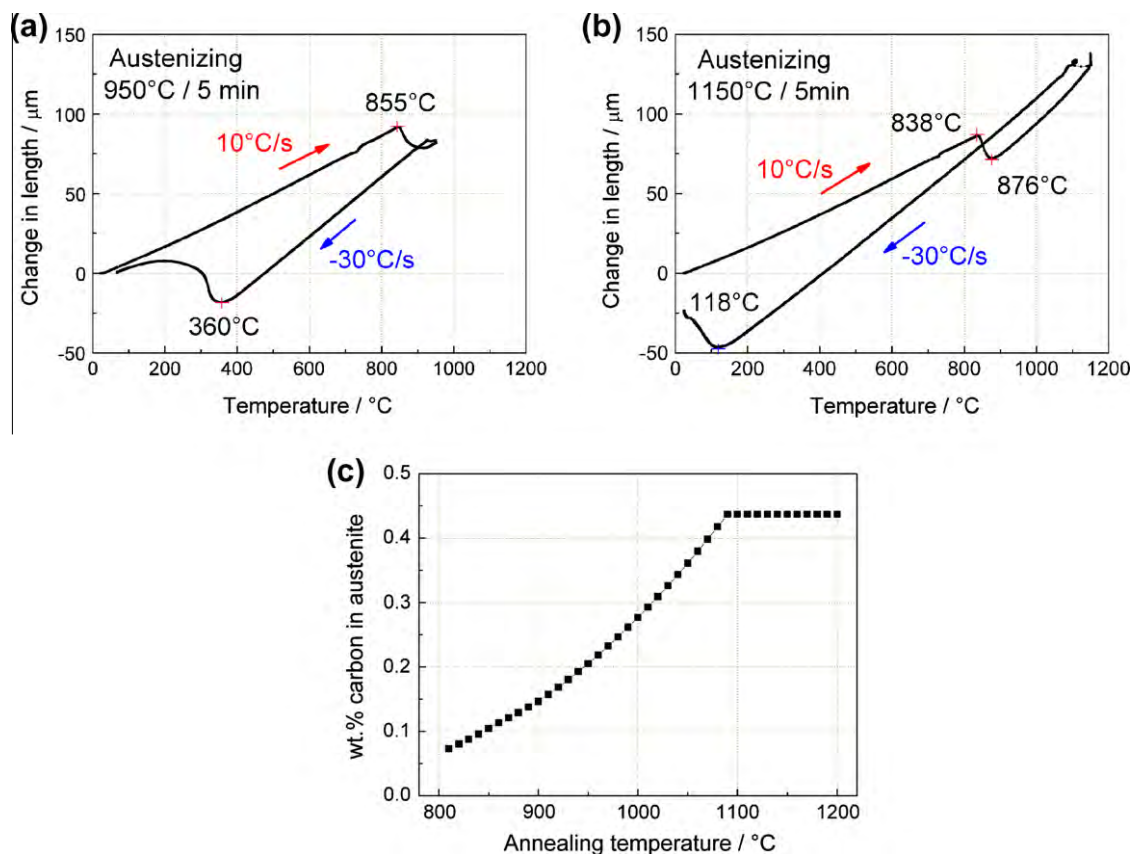


Fig. 3. Results of the dilatometer tests of the stainless steel Fe–13.6Cr–0.44C (wt.%, 1.4034). (a) Austenitization at 950 °C for 5 min. (b) Austenitization at 1150 °C for 5 min. (c) Calculated equilibrium carbon content in austenite at different annealing temperatures (Thermo-Calc TCFE5).

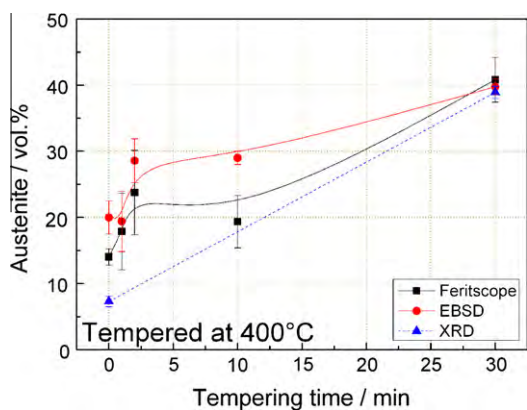


Fig. 4. Austenite volume fraction as a function of tempering time (at 400 °C) measured by feritscope (magnetic signal), EBSD and XRD.

3.3. TEM characterization

After solid solution and subsequent water quenching, we found no retained austenite in the TEM foils (Fig. 7a and b). This is in contrast to the results obtained from the EBSD maps which show retained austenite in the as-quenched state (Figs. 5 and 6). We attribute this discrepancy between TEM and EBSD results to the fact that the as-quenched metastable retained austenite – when thinned

for TEM analysis – is no longer constrained by the surrounding martensite and hence transforms into martensite.

After 1 min tempering at 400 °C we observe a high tensile strength of 2 GPa, Fig. 2a. The corresponding microstructure was monitored by TEM, Fig. 7. Fig. 7c and d gives an overview of the nanoscaled elongated carbides formed during tempering.

The carbides have an average length of 70 nm and an average width of 5 nm. After 30 min tempering the average particle spacing is ~80 nm and the length 110 nm. The carbides after 1 min tempering at 400 °C were examined via carbon extraction replica. The diffraction patterns reveal that they have M_3C structure. This means that the formation of $M_{23}C_6$ carbides is suppressed at such a low tempering temperature. EDS analyses showed that the metal content in the carbide (M in M_3C) amounts to 74 at.% Fe and 26 at.% Cr, i.e. the Cr/Fe atomic ratio is 0.35. The measured chromium content in the M_3C carbides significantly deviates from the nominal chromium concentration of 14.2 at.% Cr/82.5 at.% Fe = 0.17.

Fig. 7e shows the formation of a thin austenite layer that is located at a former martensite–martensite grain boundary. Fig. 7f is a close-up view of a thin austenite zone that is surrounded by martensite. Electron diffraction analysis reveals that a Kurdjumov–Sachs orientation relationship exists between the martensite matrix and the thin austenite

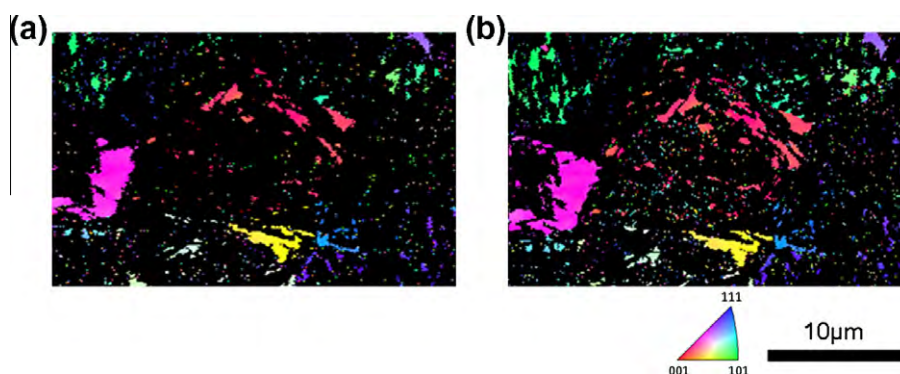


Fig. 5. EBSD inverse pole figure map of the same specimen region showing retained and reverted austenite (IPF||ND, only austenite shown): (a) shows the material as-quenched containing only retained austenite; (b) shows the material containing both retained plus reverted austenite after quenching and 5 min tempering at 400 °C (EBSD: electron back-scatter diffraction; IPF: inverse pole figure color code; ND: normal direction).

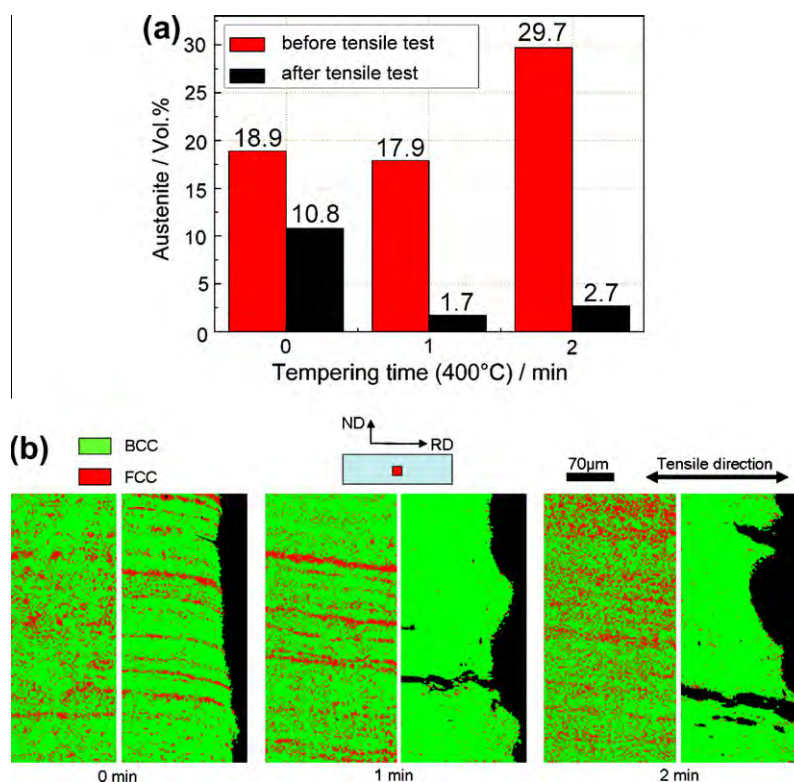


Fig. 6. (a) EBSD phase maps of samples tempered at 400 °C for 0, 1 and 2 min at 400 °C, and of the TRIP effect obtained from EBSD phase analysis. The red columns show the austenite content before and the black ones after the tensile tests. (b) Microstructure of samples before and after tensile testing subjected to different tempering conditions (left: before tensile test; right: after tensile test); bcc: martensite phase; fcc: austenite phase.

layer, Fig. 7g [38]. In line with the in situ EBSD results in Fig. 5, where we observed reverted austenite formed between martensitic grains, the austenite film observed here in TEM might be either retained or reverted austenite. In order to determine more reliably which of the two kinds is observed local atomic scale chemical analysis is conducted by using APT as outlined below. The two types of austenite can then be distinguished in terms of their carbon content: Retained austenite has at first the nominal quenched-in C content (~ 2 at.% in the present case) of the alloy while reverted austenite has a higher C content

(up to 9 at.%) owing to local partitioning and kinetic freezing. However, we also have to account for the possibility that the retained austenite can have a higher C content as the lath martensite mechanism is slow enough to allow for some C diffusion out of the martensite into the retained austenite during quenching.

3.4. Atom probe tomography

The local chemical compositions and their changes during 400 °C tempering of the martensite, austenite, carbides

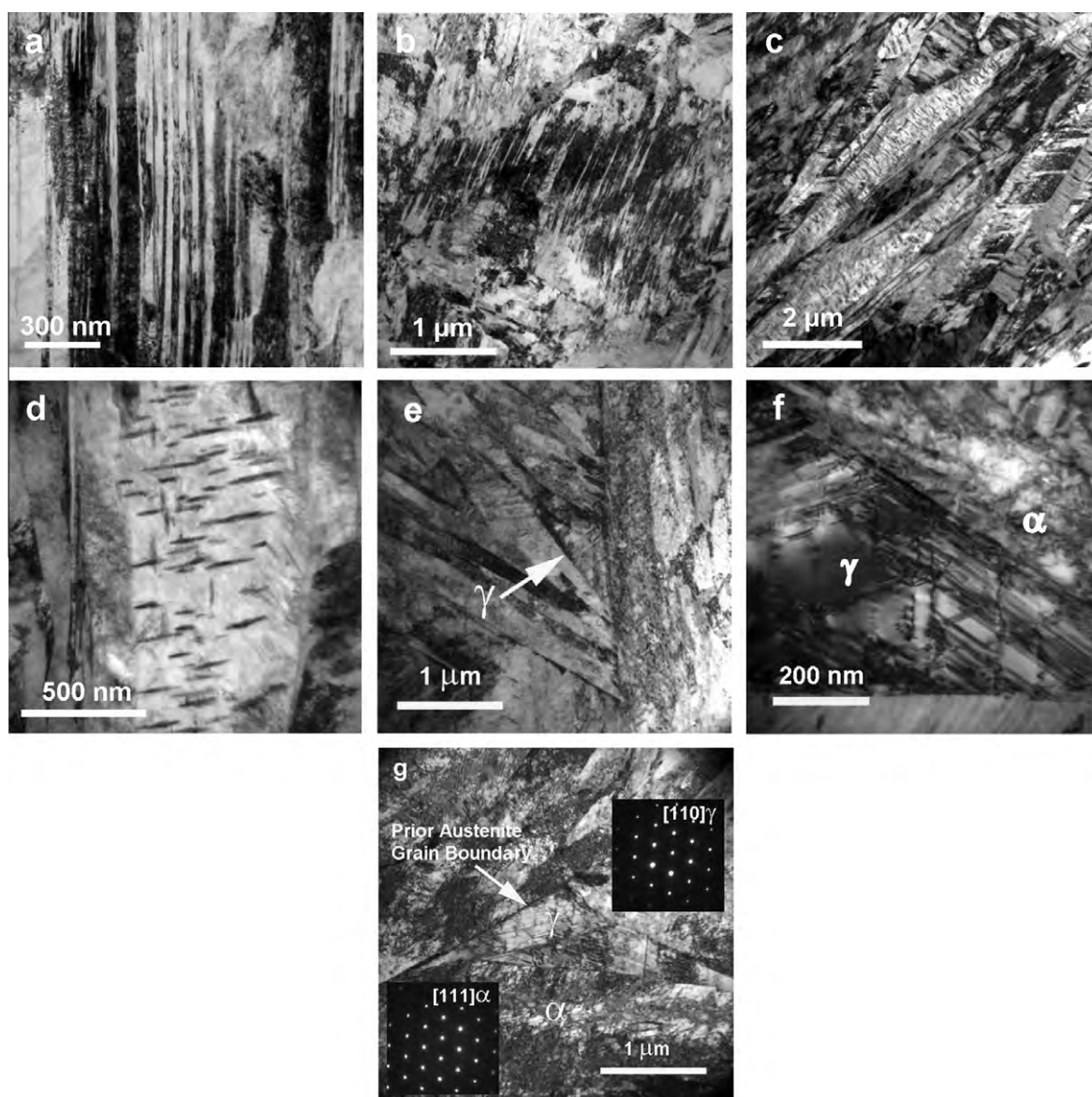


Fig. 7. TEM images of as-quenched sample (only lath martensite was found: (a and b) TEM images of samples tempered at 400 °C for 1 min; (c) overview image of the very dense array of nanoscaled carbides that is formed during tempering; (d) in-grain view of the carbides; (e) overview image of the formation of a reverted austenite grain that is located at a former martensite–martensite grain boundary; (f) close-up view of reverted austenite that is surrounded by martensite; (g) electron diffraction analysis reveals that a Kurdjumov–Sachs growth orientation relationship exists between the martensite matrix and the reverted austenite.

and interface regions were studied by atom probe tomography. Phase identification is in all cases achieved via the characteristic carbon contents of the present phases. Fig. 8 shows the 3-D atom maps after water quenching (Fig. 8a), water quenching plus tempering at 400 °C for 1 min (Fig. 8b) and water quenching plus tempering at 400 °C for 30 min (Fig. 8c). Carbon atoms are visualized as pink dots and carbon iso-concentration surfaces are in green for a value of 2 at.%. This value corresponds to the nominal carbon concentration of the alloy of 0.44 wt.%. The different phases (martensite, austenite, carbide) are marked. They were identified in terms of their characteristic carbon content and the TEM and EBSD data presented above. For more quantitative analyses, one-dimensional

compositional profiles of carbon across the martensite–martensite and martensite–austenite interfaces were plotted (along cylinders marked in yellow in the 3-D atom maps).

3.4.1. As-quenched condition

Fig. 8a reveals that in the probed volume carbon is enriched along the martensite–austenite interface. The interface region, shown as composition profile in Fig. 8a, reveals an average carbon concentration of ~1.90 at.% in the austenite with strong local variations and of ~0.98 at.% in the abutting supersaturated martensite. The carbon concentration in the austenite nearly matches the nominal carbon concentration of the alloy. Some carbon clusters occur in both phases. The carbon concentration

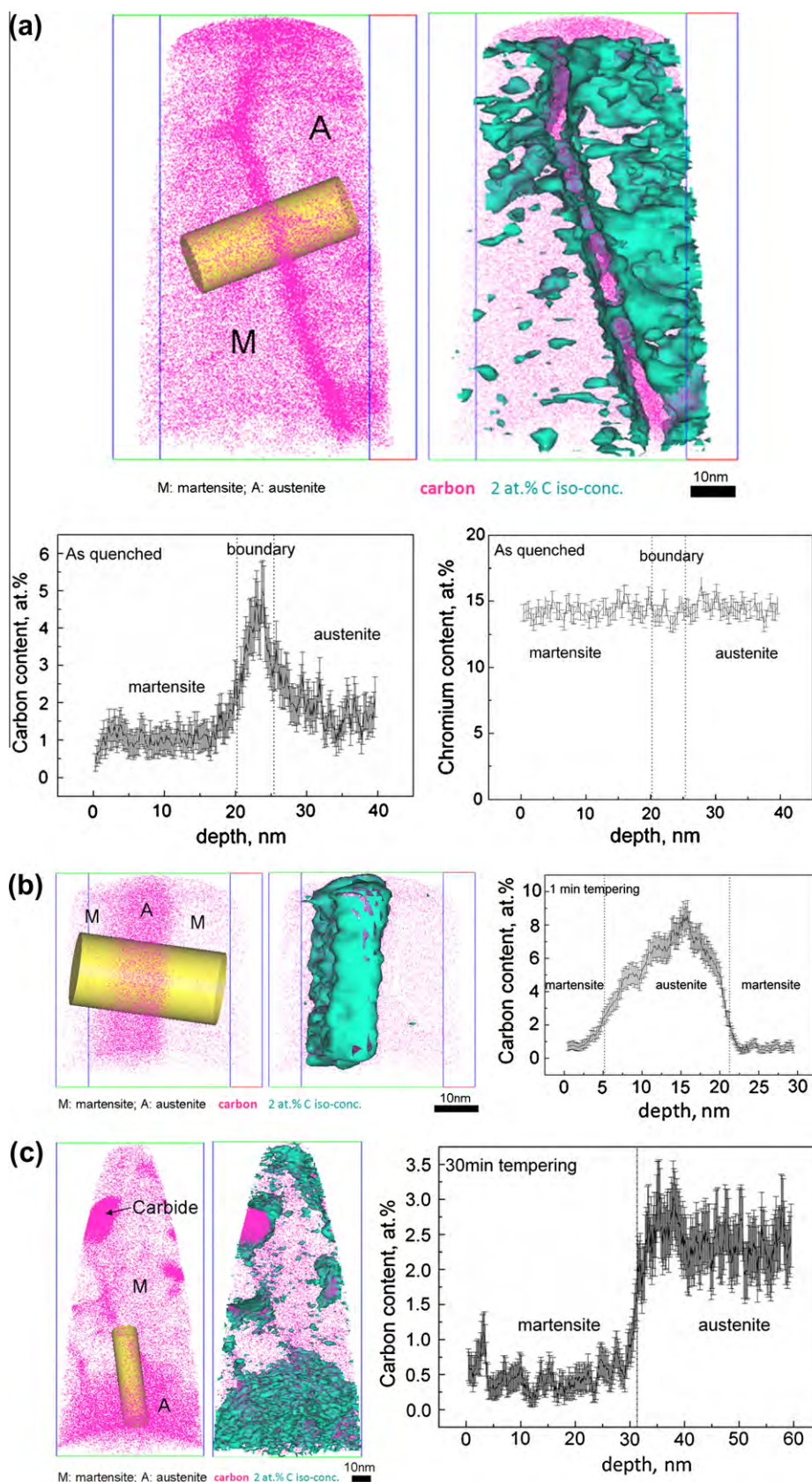


Fig. 8. (a) 3-D reconstructions (frame scale in nm) of sample after water quenching. The data clearly show that carbon redistribution already occurs during quenching. Cr redistribution does not occur. (b) Tempered at 400 °C for 1 min; (c) tempered at 400 °C for 30 min. Carbon atoms are displayed pink. The different phases are marked in the figure. Carbon iso-concentration surface (2 at.%, corresponding to 0.44 wt.%, green) and concentration profiles across the phase boundaries along the yellow cylinder) are also shown.

Table 2

Change of the carbon content observed in each phase via atom probe tomography during annealing, quenching and austenite reversion. The carbon partitioning to the different phases is quantified in terms of the enrichment factor $\varepsilon = (\text{at.\% C tempered})/(\text{at.\% C as-quenched})$, which allows us to compare the chemical composition in the phases before and after tempering.

State of samples	Retained austenite (at.%)	Martensite (at.%)	Interface (at.%)	Reverted austenite (at.%)
Nominal composition (annealing at 1150 °C)	1.97%	–	–	–
As-quenched	1.90%	0.98%	4.52%	–
Quenched plus tempering (400 °C/1 min)	–	0.82% ($\varepsilon = 0.84$)	–	6.86% ($\varepsilon = 3.61$)
Quenched plus tempering (400 °C/30 min)	2.42% ($\varepsilon = 1.27$)	0.48% ($\varepsilon = 0.49$)	–	–

in these clusters is ~ 3 at.%, i.e. they are not carbides. In a thin interface layer of only ~ 5 nm, the carbon content is very high and reaches a level of 4–6 at.%. In contrast to the variation in the carbon distribution, the chromium content is the same in the martensite, the interface and the austenite, Fig. 8a.

3.4.2. 400 °C tempered condition after quenching

After 1 min tempering at 400 °C, a carbon-enriched austenite layer (15–20 nm width) is observed between two abutting martensite regions (Fig. 8b). The thin austenite zone contains on average ~ 6.86 at.% carbon while the martensite matrix contains only ~ 0.82 at.% carbon. The identification of the phases in these diagrams follows their characteristic carbon content.

After 30 min tempering (Fig. 8c), different carbon-enriched areas appear. They correspond to individual phases. The analyzed volume can be divided into two zones. The top region with low carbon content corresponds to martensite. The bottom zone with higher carbon content corresponds to austenite. Inside the martensitic region there are areas with very high carbon content (see arrow in Fig. 8c). The carbon content is 25.1 at.% in this particle, indicating M_3C cementite stoichiometry. In the martensitic matrix surrounding the precipitate the carbon content amounts to only 0.48 at.%. Carbon partitioning to the different phases can be quantified in terms of an enrichment factor $\varepsilon = (\text{at.\% C tempered})/(\text{at.\% C as-quenched})$ to compare the compositions in the phases before and after tempering. The observed values of ε for each state are listed in Table 2. The carbon content in the martensite decreases continuously during tempering, which can be ascribed to carbon partitioning from the supersaturated martensite to the austenite and to carbide formation [39–50].

4. Discussion

4.1. Mechanisms of partitioning and austenite reversion

The microstructure observed by EBSD and TEM allows us to monitor the austenite development at the mesoscopic scale: during the initial high temperature solution annealing in the austenitic regime (1150 °C for 5 min), all carbides were dissolved (Fig. 3c). The high content of solute carbon that is present in the austenite after carbide dissolution decreases the M_s and the M_f temperatures of the austenite

below room temperature. Hence, 8–20 vol.% retained austenite exists after quenching the solution-annealed material to room temperature, Fig. 4. The differences in retained austenite are due to the individual precision of the different characterization methods. EBSD provides a direct method and hence is assumed to give a realistic value within its statistical limits.

After tempering at 400 °C for 30 min the area fraction of austenite increases to $\sim 40\%$. This change documents that strong austenite reversion takes place even at this low temperature. The local variations in the austenite dispersion after short tempering were larger compared to longer tempering times. We attribute this heterogeneity in the re-austenitization kinetics and topology to the mean diffusion range of the carbon and to the distribution of the carbon sources. Using the data of Speer et al. [40] for the diffusion coefficients in ferrite $D_\alpha = 2 \times 10^{-12} \text{ m}^2 \text{ s}^{-1}$ and in austenite $D_\gamma = 5 \times 10^{-17} \text{ m}^2 \text{ s}^{-1}$ we obtain a mean free path for carbon of $1.5 \times 10^{-4} \text{ m}$ in ferrite and $7.4 \times 10^{-7} \text{ m}$ in austenite at 400 °C and 30 min.

This means that austenite reversion starts at decorated defects (e.g. internal interfaces) where the local carbon concentration is high enough and the nucleation energy low enough to promote the formation of this phase. Fig. 7e confirms this assumption. The TEM analysis also suggests that austenite reversion proceeds via a Kurdjumov–Sachs orientation relationship. Shtansky et al. [38] found the same crystallographic relationship during reverse transformation in an Fe–17Cr–0.5C tempered martensite (wt.%).

An important aspect of the pronounced austenite reversion in the current case is that the competing formation of $M_{23}C_6$ carbides is suppressed at 400 °C. This means that more carbon is available to stabilize and promote austenite formation [38,45–47].

We used Thermo-Calc predictions [33,34] to estimate the driving force for austenite reversion for the current alloy and the employed tempering conditions, Fig. 9b. The results reveal that if the carbon concentration in the bulk martensite (α') exceeds 1.21 wt.% (5.45 at.%), austenite (γ) will form at 400 °C, provided that the nucleation barrier is overcome. This result confirms our suggestion made above, namely that no bulk austenitization can occur at this temperature since the average carbon content of the matrix is too low. Instead we assume that only certain lattice defects (interfaces) that experience very high elastic distortions and carbon segregation can provide the nucleation

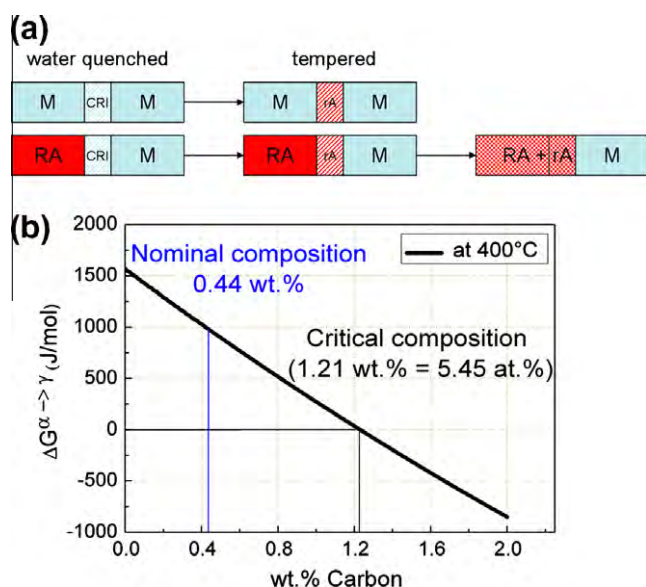


Fig. 9. (a) Schematic illustration of austenite reversion. M: martensite; CRI: carbon-rich interface; RA: retained austenite as obtained after quenching with equilibrium austenite carbon content; rA: reverted austenite formed during 300–500 °C tempering at interfaces owing to the higher local carbon content. After sufficient long diffusion time the carbon content in both types of austenite becomes similar. (b) Calculated driving force for austenite reversion at 400 °C (Thermo-Calc TCFe5).

conditions and a sufficiently high carbon concentration for local austenite formation, Figs. 7e–g and 8. This leads to an increase in the overall austenite fraction. Fig. 6a shows that a 2 min heat treatment at 400 °C leads to an increase in the austenite content from 18.9 to 29.7 vol.%.

Thermo-Calc predictions show that in the current alloy carbon provides the required driving force for this low-temperature austenite reversion. Substitutional atoms, particularly Cr, do not participate in reversion in the current alloy owing to their limited mobility at 400 °C, i.e. the driving force for transformation is here provided exclusively by the high carbon enrichment rather than by substitutional depletion of the austenite, Fig. 8a [39].

Based on these thermodynamic boundary conditions the APT results allow us now to monitor and evaluate the kinetics of carbon at different stages of tempering in more detail (Fig. 8). Fig. 8a shows the as-quenched state: during solution annealing where the material is completely austenitic the elements distribute homogeneously within that phase.

At the onset of water quenching, the majority of the austenite starts to transform into martensite without at first changing its chemical composition. However, as the solubility of carbon in the quenched-in martensite is very small, carbon starts to leave the martensite during and after the $\gamma \rightarrow \alpha'$ transformation and enriches at the $\gamma\text{--}\alpha'$ interfaces, Fig. 8a [45–50]. This process can happen extremely fast: Speer et al. [40,41] showed that carbon partitioning between martensite and austenite in a 0.19C–1.59Mn–1.63Si (wt.%) steel required at 400 °C less than 0.1 s owing to the relatively high diffusion rate of carbon in martensite. In contrast, the further distribution of the newly acquired

carbon within the austenite is nearly three orders of magnitude slower [40–50]. This means that in this case the escape rate of carbon from the newly forming lath martensite is much higher than the carbon equilibration within the austenite [48–50].

In the present quenching process, carbon segregation takes place even faster than in the study quoted above [40,41]. In the current case the carbon has already started to partition and segregate at the martensite–austenite interfaces during the early stages of water quenching immediately after the first martensite has formed [45–50]. The fast kinetics is due to the high mobility of carbon in martensite, Table 3. Such pronounced carbon segregation at the martensite–austenite interfaces is clearly observed in the as-quenched state (Fig. 8a). In the interface area the carbon content reaches up to 4–6 at.% within a narrow layer of ~ 5 nm. This value is clearly above the nominal composition that purely retained austenite would have [45–50]. Owing to the high escape rate of carbon from the martensite this zone is interpreted as a portion of initially retained austenite which has been enriched in carbon during quenching [45–50].

As explained above this high level of carbon segregation in the present case is a consequence of two effects: the rapid carbon escape from the newly formed martensite, and the low mobility of carbon within the retained austenite. According to Table 3 at 400 °C in 1 min carbon can diffuse 27,000 nm in the martensite and only 130 nm in the austenite [40]. Other sources suggest a 10–20% smaller mean free path of carbon in the martensite [43,44].

Hence, the carbon segregation observed after quenching (Fig. 8a) is due to a partitioning step and a kinetic freezing step (limited mobility of carbon once it arrives in the austenite). From comparing this experimentally observed frozen-in value of 4–6 at.% carbon at the martensite–austenite interface (Fig. 8a) with the value that is predicted by Thermo-Calc as a driving force required for austenite reversion at 400 °C (5.45 at.%), we conclude that austenite reversion will occur under the current conditions at this interface upon heat treatment.

After 1 min tempering at 400 °C, a carbon-enriched austenite layer is observed between two martensite regions (Fig. 8b). In principle this thin austenite layer could originate either from a very thin layer of retained austenite that was enriched with carbon due to partitioning from the

Table 3

Diffusion data for carbon in ferrite and austenite taken from Ref. [40]. For the current heat treatment case of 400 °C (673 K) the diffusion coefficient in ferrite is $D_\alpha = 2 \times 10^{-12} \text{ m}^2 \text{ s}^{-1}$ and in austenite $D_\gamma = 5 \times 10^{-17} \text{ m}^2 \text{ s}^{-1}$. The table gives the mean free path for the different tempering stages. The diffusion of carbon on the ferrite can be regarded as a lower bound. The corresponding value for martensite is likely to be higher owing to the high defect density of the martensite.

Time (min)	Austenite (m)	Ferrite (m)
1	1.3×10^{-7}	2.7×10^{-5}
2	1.9×10^{-7}	3.8×10^{-5}
30	7.4×10^{-7}	1.5×10^{-4}

abutting lath martensite or from austenite reversion without any preceding retained austenite. If the carbon-rich zone would be retained austenite the carbon profile in the austenite region would assume a V type distribution. This type of concentration profile would be characterized by a high content at the two martensite–austenite interfaces and a low content in the center of the austenite layer (hence “V”). Also, retained austenite would have the nominal composition, i.e. in the center of the retained austenite zone the carbon content should be 2 at.% or slightly above, as in Fig. 8a. This type of carbon distribution is not observed though. Instead, Fig. 8b shows that the carbon profile assumes a Λ shape within the austenite layer with a maximum carbon concentration above 8 at.%. It is hence plausible to assume that this profile is due to carbon segregation on a former martensite–martensite grain boundary according to the Gibbs adsorption isotherm. This means that during water quenching the carbon that is segregated at the martensite grain boundary has come from both sides. Therefore, the maximum carbon concentration revealed in Fig. 8b, which highly exceeds the equilibrium concentration that it would have been in the austenite, is in the center of the enrichment layer rather than at its rims. This means that during tempering austenite reversion starts in the center of this carbon-enriched area, i.e. at the former martensite–martensite grain boundary. The resulting average carbon concentration in this reverted austenite grain is very high, namely, 6.86 at.% (with a maximum above 8 at.%). The fact that the pronounced Λ shape of the carbon is preserved (frozen in) inside the austenite is due to the low mobility of carbon in austenite, Table 3. These observations suggest that the carbon-rich zone in Fig. 8b is a newly formed austenite layer. If the carbon-enriched area had been located between a martensite and an austenite grain, such as at the positions observed in Fig. 8a and c, the carbon atoms would have arrived only from one side, namely, from the martensite side (Fig. 9). The thickness of the newly formed reverted austenite layer in Fig. 8b is ~ 15 nm. With increasing tempering time, more reverted austenite is formed (Figs. 4 and 9).

In summary, the behavior of carbon in the current alloy can be described as follows: during quenching, carbon segregates to martensite–martensite grain boundaries (equilibrium segregation) or to martensite–retained austenite interfaces (partitioning plus kinetic freezing). In the first case (equilibrium segregation between two lath martensite zones) during tempering, these carbon-enriched areas in the martensite revert to austenite when the driving force is high enough, owing to the favorable nucleation barrier at the interfaces. In the second case (partitioning at retained austenite) the carbon enrichment leads to austenite growth according to local equilibrium. If the so-reverted austenite is located at or in the vicinity of the austenite–martensite phase boundary, carbon can diffuse from the reverted austenite further into the retained austenite provided that the tempering time is long enough. This carbon enrichment stabilizes the retained austenite. Also, this effect makes it

generally difficult to distinguish reverted austenite from retained austenite (Fig. 9). After 1 min tempering, the reverted austenite has a high carbon content of 6.86 at.% (enrichment factor $\varepsilon = 3.61$). With increasing tempering time, the diffusion of carbon from reverted austenite into retained austenite leads to an increase in the carbon concentration of the retained austenite. After 30 min tempering, the carbon concentration in the retained austenite increases to an average value of 2.42 at.% (Fig. 8c). If the diffusion distance to the nearest phase boundary is too far, e.g. inside the bulk martensite, the high concentration of carbon leads to the formation of carbides inside the martensite.

After 30 min tempering time, the carbon content in the carbides is 25.1 at.%, as measured by APT. This value agrees with the stoichiometric content of carbon in M_3C (25 at.%). Due to the carbon partitioning to austenite, austenite reversion and the competing formation of carbides, the carbon content of the martensite continuously decreases during tempering. The amount of carbon in each phase before and after tempering is listed in Table 2 for the different stages. The other elements, for example chromium, have nearly the same content in both austenite and martensite. This means that during 400 °C tempering, medium range diffusion of carbon can be observed, but the substitutional elements only experience short distance diffusion. For all tempering conditions analyzed above we observe that not the nominal (global) but the local chemical potential of carbon directly at the martensite–austenite and martensite–martensite interfaces and the smaller nucleation energy at the interfaces determine the kinetics of austenite reversion. Similar trends were observed in maraging steels during aging [28,51,52].

In a thought experiment, assuming infinite mobility of the carbon when entering from martensite into austenite, the reversion would proceed more slowly owing to the smaller chemical driving force at the interface when carbon is distributed more homogeneously inside the austenite. In the current situations, however, carbon becomes trapped and highly enriched at the martensite–austenite interface owing to the partitioning and its low mobility within the austenite. This provides a much higher local driving force for austenite reversion. We refer to this mechanism as low temperature partitioning and kinetic freezing effect because the carbon is fast inside the martensite when leaving it but slow (and, hence, frozen) when entering the austenite. A similar effect was recently observed in Fe–Mn steels [28].

4.2. Transformation induced plasticity (TRIP) effect

During tensile testing, the volume fraction of austenite decreases not only in the quenched samples but also in the tempered samples (Fig. 6). When the brittle as-quenched sample failed at an early stage of loading (Fig. 2a, green curve), the amount of retained austenite had decreased from 18.9 to 10.8 vol.%. At failure most of the quenched-in martensite was still in the elastic regime. This means that stress-induced austenite-to-martensite

transformation prevailed since the material took nearly no plastic strain until fracture. After 400 °C austenite-reversion tempering, the ductility of the material improves drastically (Fig. 2). The EBSD results reveal that nearly all of the austenite transformed into martensite during tensile testing, especially in the near-fracture zones (Fig. 6a and b). This observation suggests that strain-induced austenite-to-martensite transformation (rather than stress-induced transformation) prevails in the tempered samples containing reverted nano-sized austenite.

The difference in the displacive deformation behavior between the as-quenched and tempered samples is due to the fact that directly after water quenching, the retained austenite is unstable due to its relatively low carbon content. In the as-quenched state (i.e. without tempering) the carbon content of the retained austenite is equal to the nominal composition after solution treatment. A relatively weak load is, hence, required to transform this retained and rather unstable austenite into martensite at the onset of the tensile test. Transforming a large amount of austenite at the same time, namely, at the beginning of deformation, promotes crack formation and premature failure. In contrast to this as-quenched and rather unstable austenite, subsequent tempering enriches the retained austenite with carbon due to partitioning. The higher carbon content stabilizes the retained and the reverted austenite so that austenite portions with different carbon content undergo the TRIP effect at different stages of deformation. These differences in carbon content of different austenite portions in the same sample are due to the fact that only the local chemical potential of the carbon at the hetero-interfaces determines the partitioning and reversing rates and, hence, also the exact carbon content of the abutting austenite. This means that retained and reverted austenite zones that are carbon-enriched through partitioning have a kinetically determined composition which is subject to local variations in the chemical potential (of carbon). This context explains the more continuous displacive transformation sequence in the tempered material and hence the observed ductility improvement.

Another aspect of the TRIP effect in this material is that austenite reversion, obtained from tempering, does not only stabilize the austenite via a higher carbon content but also increases its overall volume fraction at least after sufficient tempering time. Fig. 6a reveals that the austenite fraction increases from 18.9 vol.% after quenching to 29.7 vol.% after 2 min at 400 °C. Interestingly, after 1 min at 400 °C the austenite fraction did not change much. This means that for the short-annealing case (1 min) the austenite stability and its more sequential transformation as outlined above are more important for the ductilization than its mere volume fraction.

4.3. Precipitation development

The TEM and APT observations confirm that the carbides formed during tempering have are of M_3C type

(instead of $M_{23}C_6$). The formation of M_3C is associated with a smaller loss of chromium from the matrix (into carbides) compared to $M_{23}C_6$ -type carbides, which can have a high chromium content. Some authors found a sequence of carbide formation in Fe–Cr–C systems during tempering according to $MC \rightarrow M_3C \rightarrow M_7C_3 + M_{23}C_6 + M_6C$ [53]. In our study M_3C carbides prevailed up to 30 min annealing time. Samples taken from the as-quenched state show the highest hardness due to carbon in solid solution. The hardness decrease observed during tempering is related to carbide formation because carbon has a higher strengthening effect in solid solution than in the form of carbides. However, the small carbides (Fig. 8c) also contribute to the strength as observed with TEM (see Fig. 7b). The strain hardening rate decreases with increasing tempering time. This might be due to the coarsening of the carbides and due to the increase in the average carbide spacing (from ~40 nm after 1 min to ~80 nm after 30 min tempering at 400 °C). Further, we observe that the yield stress increases during tempering. This might be due to the change in the internal stress state of the martensite matrix. After water quenching, high elastic stresses prevail in the martensite. These lead to early microplastic yielding of the material prior to percolative bulk plastic yielding. During tempering, the internal stress state of the martensite is relaxed due to the escape of carbon. This leads to a delay in the yielding of the tempered samples.

4.4. Relationship between nanostructure and stress–strain behavior

In the preceding sections we presented experimental evidence of grain boundary segregation, hetero-interface partitioning, kinetic freezing, carbide precipitation, retained austenite formation and stabilization, austenite reversion, and the TRIP effect.

In this part we discuss the joint influence of these phenomena on the excellent strength–ductility profile of this steel (Fig. 2a and d).

We differentiate between mechanisms that provide higher strength and those promoting ductility: the most relevant phase responsible for the high strength of the steel after heat treatment is the relaxed martensite. The quenched-in martensite with an extrapolated tensile strength of more than 2300 MPa (approximated from hardness data) is very brittle. Already a very modest heat treatment of 1 min at 400 °C though (Fig. 2a) provides sufficient carbon mobility. This leads to carbon redistribution (carbide formation, grain boundary segregation, dislocation decoration, martensite–austenite interface segregation, austenite solution) and thus to a reduction in the internal stresses of the martensite. The reduced carbon content renders the martensite into a phase that can be plastically deformed without immediate fracture. The second contribution to the increase in strength are the nanoscaled carbides which provide Orowan strengthening, Figs. 7 (TEM) and Fig. 8c (APT). Their average spacing increases

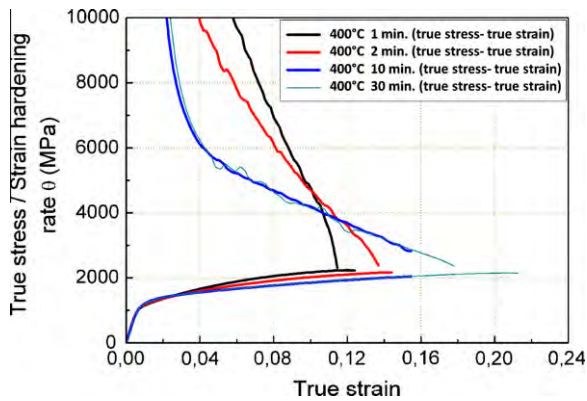


Fig. 10. True stress–true strain curves and corresponding strain hardening curves for the steel after 400 °C heat treatment at different times. The data reveal that the tempering, associated with the increase in the austenite content via austenite reversion, yields higher strain hardening reserves at the later stages of deformation due to the TRIP effect.

from ~ 50 nm (1 min at 400 °C) to ~ 80 nm (30 min at 400 °C), Fig. 8b. These two effects, i.e. conventional martensite strength (via high dislocation density, high internal interface density, internal stresses, solid solution strengthening) and Orowan strengthening explain the high strength of the material, but they do not explain its high ductility.

In this context the TRIP effect, i.e. the displacive transformation of retained and reverted austenite, becomes relevant: Fig. 6a reveals a drop in the austenite content from 29.7 to ~ 2.7 vol.% during deformation for the sample heat treated at 400 °C for 2 min. Fig. 10 shows the true stress–true strain curves and their corresponding derivatives (strain hardening) after 400 °C heat treatment at different times. The data reveal that the tempering, which increases the austenite content via reversion, leads indeed to higher strain hardening reserves at the later stages of deformation due to the TRIP effect, Fig. 6b. Since longer heat treatments lead to higher volume fractions of reverted austenite the TRIP-related strain hardening assumes a higher level for these samples (Fig. 10).

Another important effect that might promote ductility in this context is the wide distribution of the austenite dispersion and stability (carbon content) which are both characteristic for this material. As revealed in Fig. 8 we can differentiate three types of austenite, Fig. 9a. The first type is the as-quenched retained austenite with the nominal carbon content and relatively low stability. The second one is retained austenite, which assumes an increased carbon content due to partitioning during quenching and particularly during heat treatment and has thus higher stability against

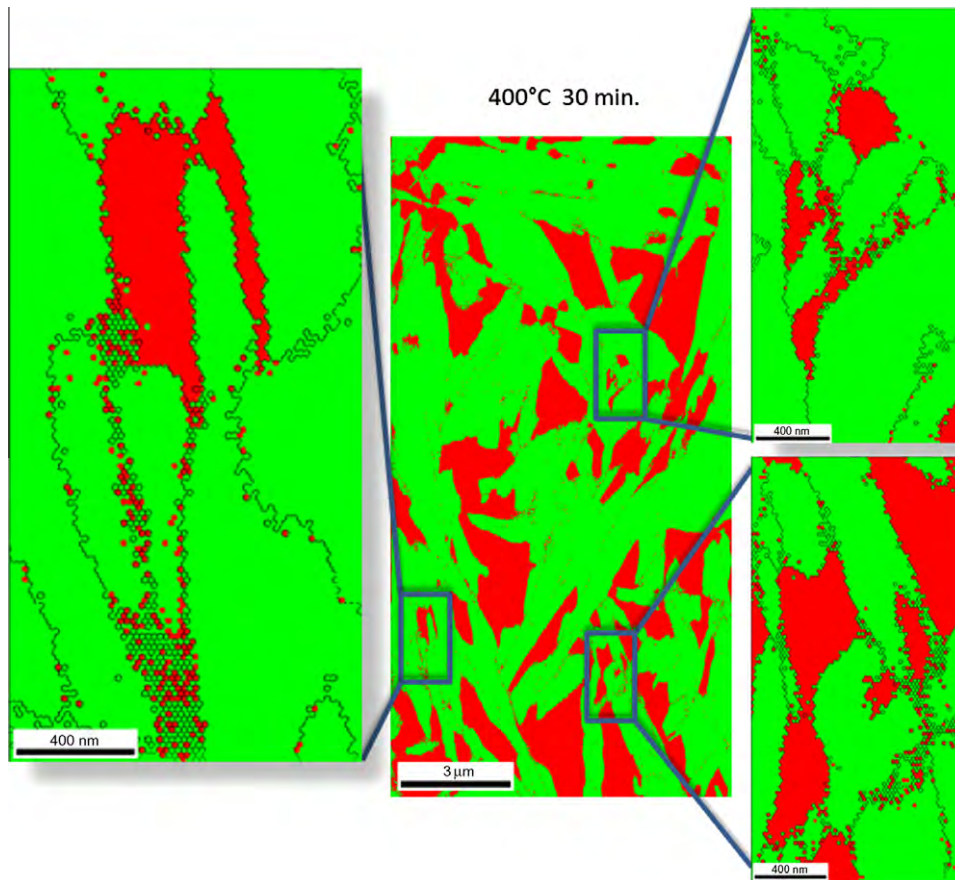


Fig. 11. High-resolution EBSD map (20 nm step size) of the sample tempered at 400 °C for 30 min. The map shows that on some martensite grain boundaries a very thin reverted austenite layer exists. This thin austenite seam can act as a compliance or respectively repair layer against damage percolation entering from the martensite grain. Austenite: red; martensite: green.

displacive transformation. The third type of austenite is the reverted one. These three types of austenite have different carbon concentration, volume fraction and size. Both carbon content and size affect austenite stability. This means that the displacive transformation during tensile testing and the associated accommodation plasticity occur more gradually upon loading compared to a TRIP effect that affects a more homogeneous austenite. We refer to this mechanism as a heterogeneous TRIP effect.

Another important aspect is the composite-like architecture of the reverted austenite, which is located at the martensite–martensite and at the martensite–austenite interfaces in the form of nanoscaled seams (see Figs. 8 and 11). Such a topology might act as a soft barrier against incoming cracks or stress–strain localizations from the martensite. We hence speculate that the austenite seam is a compliance or respectively repair layer that can immobilize defects through its high formability and prevent cracks from percolating from one martensite grain into another (Fig. 11). In this context it is important to note that conventional martensite–martensite interfaces often have a small-angle grain boundary between them which facilitates crack penetration from one lath to another. Here, a compliant austenite seam between the laths might hence be very efficient in stopping cracks.

We emphasize this point since the increase in macroscopic ductility can generally be promoted by both an increase in strain hardening at the later stages of deformation and mechanisms that prevent premature damage initiation.

5. Conclusions

We studied carbon partitioning, retained austenite, austenite stabilization, nanoscale austenite reversion, carbide formation and kinetic freezing of carbon during heat treatment of a martensitic stainless steel Fe–13.6Cr–0.44C (wt.%). The main results are as follows:

1. Austenite formation in carbon-enriched martensite–austenite interface areas is confirmed by XRD, EBSD, TEM and APT. Both the formation of retained austenite and austenite reversion during low-temperature partitioning is discussed. The enrichment of carbon at martensite–martensite grain boundaries and martensite-retained austenite phase boundaries provides the driving force for austenite reversion. The reverted austenite zones have nanoscopic size (~15–20 nm). The driving forces for austenite reversion are determined by local and not by global chemical equilibrium.
2. Martensite-to-austenite reversion proceeds fast. This applies to both the formation of reversed austenite at retained austenite layers and austenite reversion among martensite laths. The volume fraction of austenite has nearly doubled after 2 min at 400 °C.
3. The carbides formed during tempering have M_3C structure. With increasing tempering time the dispersion of the carbides decreases due to the Gibbs–Thomson effect.
4. During tempering between 300 °C and 500 °C carbon redistributes in three different ways. During quenching, in the vicinity of martensite–austenite interfaces, carbon segregates from the supersaturated martensite to both the hetero-interfaces and homophase grain boundaries. During tempering, carbon continuously partitions to martensite–austenite interfaces, driving the carbon-enriched areas towards austenite reversion (irrespective of whether the nucleation zones were initially retained or reversed austenite). Carbon inside martensite, far away from any interfaces, tends to form M_3C carbides. This means that carbon segregates to martensite grain boundaries, to martensite–austenite interfaces, and forms carbides.
5. We differentiate between three different types of austenite, namely, first, as-quenched retained austenite with nominal carbon content and low stability; second, retained austenite with increased carbon content and higher stability due to partitioning according to the local chemical potential of carbon; and third, reverted austenite.
6. The nanoscale structural changes lead to drastic improvements in the mechanical properties. A sample after 1 min tempering at 400 °C has 2 GPa tensile strength with 14% total elongation. The strength increase is attributed to the high carbon content of the martensite and the interaction between dislocations and nano-sized carbides. The TRIP effect of the austenite during deformation, including the reverted nanoscale austenite, contributes to a strain-hardening capacity and, hence, promotes the ductility. Also, the topology of the reverted austenite is important: we suggest that the nanoscaled seam topology of the austenite surrounding the martensite acts as a soft barrier which has compliance and repair function. This might immobilize defects and prevent cracks from growth and inter-grain percolation.
7. We attribute the fast nanoscale austenite reversion to an effect that we refer to as kinetic freezing of carbon. This means that the carbon is fast inside the martensite when leaving it but slow (and hence frozen) when entering the austenite. This means that carbon becomes trapped and highly enriched at the martensite–austenite interfaces owing to its low mobility within the austenite during low-temperature partitioning. This provides a much higher local driving force for austenite reversion. This means that the formation of nanoscaled reverted austenite depends mainly on the local but not on the global chemical potential of carbon at internal interfaces.

Acknowledgement

The authors are grateful for discussions on carbon partitioning and martensite tempering with Professor George D.W. Smith from Oxford University.

References

- [1] Zou D, Han Y, Zhang W, Fang X. *J Iron Steel Res Int* 2010;17(8):50.
- [2] Rodrigues CAD, Lorenzo PLD, Sokolowski A, Barbosa CA, Rollo JMDA. *Mater Sci Eng A* 2007;460–461:149.
- [3] Karlsen M, Grong O, Soefferud M, Hjelen J, Roervik G, Chiron R. *Metall Mater Trans* 2009;40A:310.
- [4] Pieta G, Leite R, Kwietniewski C, Clarke T, Strohaecker T. *J Mater Eng Perform* 2010;19(9):1318.
- [5] Kurdjumov GV. Twelfth Hatfield Memorial Lecture; 1959.
- [6] Clarke AJ, Speer JG, Miller MK, Hackenberg RE, Edmonds DV, Matlock DK, et al. *Acta Mater* 2008;56:16.
- [7] Malakondaiah G, Srinivas M, Rao PR. *Prog Mater Sci* 1997;42:209.
- [8] Speer JG, Matlock DK, Cooman BCD, Schroth JG. *Acta Mater* 2003;51:2611.
- [9] Edmonds DV, Hea K, Rizzo FC, Cooman BCD, Matlock DK, Speer JG. *Mater Sci Eng A* 2006;438–440:25.
- [10] Tomimura K, Takaki S, Tanimoto S, Tokunaga Y. *ISIJ Int* 1991;31:721.
- [11] Tomimura K, Takaki S, Tokunaga Y. *ISIJ Int* 1991;31:1431.
- [12] Takaki S, Tomimura K, Ueda S. *ISIJ Int* 1994;34:522.
- [13] Nakada N, Tsuchiyama T, Takaki S, Hashizume S. *ISIJ Int* 2007;47:1527.
- [14] Furuhashi T, Kikumoto K, Saito H, Sekine T, Ogawa T, Morito S, et al. *ISIJ Int* 2008;48:1038.
- [15] Nakada N, Tsuchiyama T, Takaki S, Miyano N. *ISIJ Int* 2011;51:299.
- [16] Nayak SS, Anumolu R, Misra RDK, Kim KH, Lee DL. *Mater Sci Eng* 2008;A498:442.
- [17] Cerezo A, Godfrey TJ, Smith GDW. *Rev Sci Instrum* 1988;59:862.
- [18] Blavette D, Deconihout B, Bostel A, Sarrau JM, Bouet M, Menand A. *Rev Sci Instrum* 1993;64:2911.
- [19] Miller MK, Cerezo A, Hetherington MG, Smith GDW. *Atom probe field ion microscopy*. Oxford: Oxford University Press; 1996.
- [20] Thuvander M, Miller MK, Stiller K. *Mater Sci Eng* 1999;A270:38.
- [21] Miller MK. *Atom probe tomography analysis at the atomic scale*. New York: Kluwer Academic/Plenum; 2000.
- [22] Kelly TF, Miller MK. *Rev Sci Instrum* 2007;78:031101.
- [23] Seidman D. *Annu Rev Mater Sci* 2007;37:127.
- [24] Miller MK, Forbes RG. *Mater Charact* 2009;60:461.
- [25] Marquis EA, Miller MK, Blavette D, Ringer SP, Sudbrack CK, Smith GDW. *MRS Bull* 2009;34:725.
- [26] Pereloma EV, Stohr RA, Miller MK, Ringer SP. *Metall Mater Trans* 2009;40A:3069.
- [27] Sauvage X, Lefebvre W, Genevois C, Ohsaki S, Hono K. *Scripta Mater* 2009;60:1056.
- [28] Dmitrieva O, Ponge D, Inden G, Millán J, Choi P, Sietsma J, et al. *Acta Mater* 2011;59:364.
- [29] Gerezo A, Godfrey TJ, Smith GDW. *Rev Sci Instrum* 1988;59:862.
- [30] Raabe D, Choi PP, Li YJ, Kostka A, Sauvage X, Lecouturier F, et al. *MRS Bull* 2010;35:982.
- [31] Ohsaki S, Raabe D, Hono K. *Acta Mater* 2009;57:5254.
- [32] Choi P, da Silva M, Klement U, Al-Kassab T, Kirchheim R. *Acta Mater* 2005;53:4473.
- [33] Thermo-Calc User's Guide, Version R. Stockholm: Thermo-Calc software AB and foundation of computational thermodynamics; 1995–2006.
- [34] Thermodynamic database TCFE5-TCS steels/Fe-alloys database, version 5, Thermo-Calc software. <<http://www.Thermocalc.com>>.
- [35] Sato H, Zaeferrer S. *Acta Mater* 2009;57:1931.
- [36] Jiménez JA, Carsí M, Frommeyer G, Knippscher S, Wittig J, Ruano OA. *Intermetallics* 2005;13:1021.
- [37] Rühle M. *Metallography and microstructures*. In: *Transmission electron microscopy*. ASM Handbook, vol. 9. Materials Park (OH): ASM International; 1995.
- [38] Shtansky DV, Nakai K, Ohmori Y. *Acta Mater* 2000;48:1679.
- [39] Miyamoto G, Usuki H, Li ZD, Furuhashi T. *Acta Mater* 2010;58:4492.
- [40] Speer JG, Edmonds DV, Rizzo FC, Matlock DK. *Curr Opin Solid State Mater Sci* 2004;8:219.
- [41] Streicher AM, Speer JG, Matlock DK, De Cooman BC. In: *Proceedings of the international conference on advanced high strength sheet steels for automotive applications*, vol. 51; 2004.
- [42] Zhong N, Wang XD, Wang L, Rong YH. *Mater Sci Eng* 2009;A506:111.
- [43] McLellan RB, Wasz ML. *J Phys Chem Solids* 1993;54:583.
- [44] Haasen P. *Physikalische Metallkunde*. Berlin: Springer-Verlag; 1974. p. 173.
- [45] Zhu C, Xiong XY, Cerezo A, Hardwicke R, Krauss G, Smith GDW. *Ultramicroscopy: IFES 2006, proceedings of the 50th international field emission symposium/19th IVNC 107; 2007*. p. 808–12.
- [46] Sarikaya M, Thomas G, Steeds JW, Barnard SJ, Smith GDW. *Proc solid–solid phase transformations conf. Pittsburgh (PA), Warrendale (PA): The Metallurgical Society of the AIME; 1981*.
- [47] Barnard SJ, Smith GDW, Sarikaya M, Thomas G. *Scripta Metall* 1981;15:387.
- [48] Bhadeshia HKDH. *Met Sci* 1983;17:151.
- [49] Bhadeshia HKDH. *Met Sci* 1981;15:175.
- [50] Thomas G, Sarikaya M, Smith GDW, Barnard SJ. *Advances in the physical metallurgy and applications of steels*. London: The Metals Society; 1983. p. 259–65.
- [51] Höring S, Abou-Ras D, Wanderka N, Leitner H, Clemens H, Banhart J. *Steel Res Int* 2009;80:84.
- [52] Schnitzer R, Radis R, Nöhner M, Schober M, Hochfellner R, Zinner S, et al. *Mater Chem Phys* 2010;122:138.
- [53] Yan F, Shi H, Fan J, Xu Z. *Mater Charact* 2008;59:883.

Deformation and fracture mechanisms in fine- and ultrafine-grained ferrite/martensite dual-phase steels and the effect of aging

Marion Calcagnotto^a, Yoshitaka Adachi^b, Dirk Ponge^a, Dierk Raabe^{a,*}

^a Max-Planck-Institut für Eisenforschung GmbH, Max-Planck-Straße 1, 40237 Düsseldorf, Germany

^b National Institute for Materials Science, 1-2-1 Sengen, Tsukuba, Ibaraki 305-0047, Japan

Received 23 August 2010; received in revised form 29 September 2010; accepted 1 October 2010

Available online 30 October 2010

Abstract

Three ferrite/martensite dual-phase steels varying in the ferrite grain size (12.4, 2.4 and 1.2 μm) but with the same martensite content (~ 30 vol.%) were produced by large-strain warm deformation at different deformation temperatures, followed by intercritical annealing. Their mechanical properties were compared, and the response of the ultrafine-grained steel (1.2 μm) to aging at 170 °C was investigated. The deformation and fracture mechanisms were studied based on microstructure observations using scanning electron microscopy and electron backscatter diffraction. Grain refinement leads to an increase in both yield strength and tensile strength, whereas uniform elongation and total elongation are less affected. This can be partly explained by the increase in the initial strain-hardening rate. Moreover, the stress/strain partitioning characteristics between ferrite and martensite change due to grain refinement, leading to enhanced martensite plasticity and better interface cohesion. Grain refinement further promotes ductile fracture mechanisms, which is a result of the improved fracture toughness of martensite. The aging treatment leads to a strong increase in yield strength and improves the uniform and total elongation. These effects are attributed to dislocation locking due to the formation of Cottrell atmospheres and relaxation of internal stresses, as well as to the reduction in the interstitial carbon content in ferrite and tempering effects in martensite.

© 2010 Acta Materialia Inc. Published by Elsevier Ltd. All rights reserved.

Keywords: Ultrafine grains; Dual-phase steel; Aging; Deformation mechanisms; Fracture mechanisms

1. Introduction

Grain refinement of metals is essential as it is the only strengthening mechanism that simultaneously enhances the toughness of a material. In recent years, a variety of methods have been developed to produce ultrafine-grained (UFG) materials with a ferrite grain size of around 1 μm [1,2]. These methods can be divided into advanced thermo-mechanical processing (ATMP) routes, which aim at improving conventional processing routes in commercial large-scale rolling mills, and severe plastic deformation (SPD) techniques, which are essentially confined to labora-

tory-scale sample dimensions. The ATMP methods cover deformation-induced ferrite transformation (DIFT) [3], large-strain warm deformation [4], intercritical hot rolling [5], multi-directional rolling [6] and cold-rolling plus annealing of martensitic steel [7]. The most important SPD techniques are equal-channel angular pressing (ECAP) [8], accumulative roll bonding [9] and high-pressure torsion [10].

It was consistently found that yield strength and tensile strength are drastically increased due to grain refinement, whereas uniform and total elongation are decreased. Also, Lüders straining becomes more pronounced. Furthermore, UFG steels exhibit a very low strain-hardening rate [11], which marks the main limitation with respect to commercial applications. In terms of toughness, a significant reduction in the ductile-to-brittle transition temperature

* Corresponding author. Tel.: +49 211 6792 340; fax: +49 211 6792 333.
E-mail address: d.raabe@mpie.de (D. Raabe).

has been repeatedly reported [12,13]. For these reasons, it is of ongoing interest to overcome the restricted ductility of UFG materials without sacrificing strength and toughness. Among the possible ways to restore the strain hardenability of UFG materials are the fabrication of a bimodal grain size distribution [14] and the introduction of nano-sized cementite particles into the microstructure [6]. Another aspect that might improve the applicability of UFG materials is their ability to show superplasticity [15]. Shin and Park [16] showed that replacing cementite as a second phase by martensite through an intercritical annealing treatment leads to a substantial increase in strain-hardening rate, causing a higher ultimate tensile strength with only slightly reduced uniform and total elongation. In this way, a UFG ferrite/martensite dual-phase (DP) steel was designed which shows superior mechanical properties compared to coarser grained conventional DP steels. The term “dual-phase steel” refers to a group of steels consisting of a soft ferrite matrix and 3–30 vol.% of hard martensite islands. These steels are widely used for automotive applications. DP steels have a number of unique properties, which include a low elastic limit, high initial strain-hardening rate, continuous yielding, high tensile strength and high uniform and total elongation. Moreover, DP steels exhibit a bake-hardening (BH) effect, i.e. the yield strength increases upon aging at paint-baking temperatures (~ 170 °C) after forming, giving rise to improved dent and crush resistance. The austenite-to-martensite phase transformation bears the main influence on the mechanical properties of dual-phase steels [17,18]. This phase transformation involves a volume expansion of 2–4% [19], causing an elastically and plastically deformed zone in the ferrite adjacent to martensite [20]. The deformed zone contains a high number of unpinned dislocations [21], giving rise to dislocation heterogeneities in the ferrite. The low elastic limit is thus suggested to be generated by the combined effects of the present elastic stresses that facilitate plastic flow and the additional dislocation, which is assumed to be partly mobile during early stages of yielding [22]. Dislocation–dislocation interactions, dislocation pile-ups at ferrite/martensite interfaces and the corresponding long-range elastic back stresses contribute to rapid strain hardening.

Previous studies on grain refinement in DP steels consistently revealed that, unlike in other metallic materials, the increases in yield strength and tensile strength are not counteracted by a significant reduction in the uniform and total elongation [23–28]. This can partly be explained by the enhanced strain-hardening rate due to grain refinement as a result of the higher number of geometrically necessary dislocations (GNDs) along the ferrite–martensite boundaries [25]. Ultrafine-grained DP steels have been produced by applying a two-step processing route consisting of (1) a deformation treatment to produce UFG ferrite and finely dispersed cementite or pearlite and (2) a short intercritical annealing in the ferrite/austenite two-phase field followed by quenching to transform all austenite to

martensite. Grain refinement in step (1) was achieved by ECAP [27], cold rolling [28], cold swaging [24] and large-strain warm deformation [29]. A single-pass processing route based on DIFT was proposed by Mukherjee et al. [26,30].

As the number of investigations on this topic is very limited, more research is required to understand the mechanical response of DP steels to ferrite grain sizes close to or below 1 μm . Furthermore, as the microstructures described in the previous studies often differ in the martensite volume fraction, it has not been possible to interpret the grain size effect on the mechanical properties independently so far. Therefore, in this study we compare the deformation and fracture mechanisms of a coarse-grained (CG), a fine-grained (FG) and a UFG-DP steel, having about the same martensite volume fractions. In addition, the aging (BH) response of the UFG-DP steel is investigated, which has not been addressed so far. In conjunction with the mechanical data, the microstructure evolution during tensile straining and the fracture mechanisms are studied by using scanning electron microscopy (SEM) and high-resolution electron backscatter diffraction (EBSD). Furthermore, slip-band evolution during deformation was investigated by performing tensile tests which were interrupted at strain levels between 1% and 4%.

2. Experimental procedures

2.1. Materials processing

A plain carbon manganese steel of composition (in wt.%) 0.17 C, 1.49 Mn, 0.22 Si, 0.033 Al, 0.0033 N, 0.0017 P and 0.0031 S was produced by vacuum induction melting. A lean composition was selected in order to show that a stable ferrite grain size of around 1 μm can be achieved via thermomechanical processing without microalloying. Carbon enhances both grain refinement and grain size stability [31]. At the same time, the carbon content has to be low enough to ensure good weldability, which is fulfilled for carbon contents below 0.2%. Mn was also shown to be highly beneficial for the grain refinement process [32]. Furthermore, it increases the hardenability and lowers the A_{r3} temperature [29]. However, too high a Mn content will promote segregation and undesired banded microstructures. Samples ($50 \times 40 \times 60$ mm³) for thermomechanical processing were machined directly from the cast ingot. The thermomechanical processing was realized by use of a large-scale 2.5 MN hot deformation simulator [4,33,34]. This computer-controlled servohydraulic press allows the simulation of industrial hot-rolling processing routes by performing multi-step flat compression tests. The processing schedules to obtain three different grain sizes are outlined in Fig. 1.

The first step is identical for all processing schedules. It consists of 3 min of re-austenitization at 912 °C and a single-pass deformation at 860 °C applying a logarithmic strain of $\varepsilon = 0.3$ at a strain rate of 10 s^{-1} above the recrystallization temperature. In the CG route (Fig. 1a),

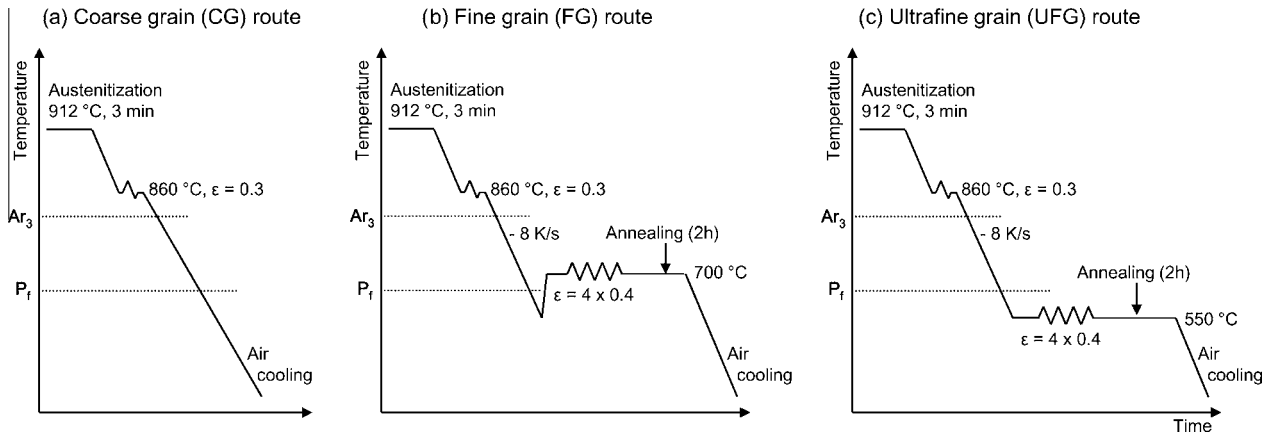


Fig. 1. Thermomechanical processing routes to produce different grain sizes in a hot deformation simulator. All treatments are followed by an intercritical annealing at 730 °C for 3 min and subsequent quenching to obtain the final ferrite/martensite dual-phase microstructure. Ar_3 : non-equilibrium transformation start temperature; P_f : pearlite transformation finish temperature; ϵ : logarithmic strain.

the sample is then air cooled to room temperature to obtain a conventional ferrite–pearlite starting microstructure. Grain refinement is achieved by subsequent large-strain warm deformation at 700 °C (the FG route, Fig. 1b) and at 550 °C (the UFG route, Fig. 1c), respectively. A total strain of 1.6 is realized by a four-step flat compression series, each step exerting a strain of 0.4 at a strain rate of 10 s^{-1} . The deformation temperature controls the degree of grain refinement. At 700 °C, a fine polygonal ferrite matrix with globular cementite and fine pearlite colonies is formed. At 550 °C, continuous grain subdivision and pronounced recovery lead to slightly elongated ferrite grains with a grain size of around $1 \mu\text{m}$ [4]. The cementite lamellae of the pearlite colonies undergo continuous fragmentation and spheroidization. This results in a fine distribution of spheroidized cementite particles which mainly cover the ferrite grain boundaries. After warm deformation, specimens were annealed for 2 h at the respective deformation temperature to simulate coiling at elevated temperatures, and then air cooled to room temperature.

To obtain the final ferrite/martensite dual-phase microstructure, all specimens were subjected to intercritical annealing in the ferrite/austenite two-phase region followed by quenching in order to transform all austenite into martensite. This treatment was carried out in a salt bath furnace. The temperature was controlled electronically and held constant at 730 °C. The reheating time was 2 min, as was predetermined using a thermocouple embedded in a test specimen. Samples were annealed for 3 min (including reheating time) in the salt bath, before being quenched in water. The intercritical annealing parameters were established by performing dilatometer tests [29].

Three of the UFG samples were additionally aged at 170 °C for 20 min in a vacuum furnace to simulate the BH process, which is active during paint baking in automotive manufacturing. Generally, the increase in yield strength after prestraining between 2% and 12% plus aging at $\sim 170 \text{ °C}$ for 20–30 min is determined to assess the

bake-hardenability of a steel grade. Here, only the BH_0 (no prestrain) value for the UFG-DP steel is reported.

2.2. Microstructure characterization

Samples for SEM and EBSD were prepared by standard mechanical grinding and polishing procedures, finishing with 3 min colloidal silica polishing. To reveal the microstructure for SEM observations, the samples were additionally etched in 1% Nital for 3 s. For high-resolution EBSD measurements, the sample surface has to be extremely clean and free of roughness and deformation in order to obtain high-quality Kikuchi patterns. Therefore, they were electropolished using Struers electrolyte A2 at room temperature (voltage: 30 V; flow rate: 12 s^{-1} ; polishing time: 10 s).

The martensite volume fraction and the ferrite grain size were determined on the basis of three SEM micrographs taken at a magnification of $\times 3000$ for the UFG and FG steel and of $\times 500$ for the CG steel. A point-counting method was used to determine the second phase fraction. As it is not possible to differentiate between martensite and austenite on etched specimens in the scanning electron microscope, the second phase fraction was determined as the fraction of martensite plus retained austenite. The retained austenite volume fraction was determined to range between 1 and 3 vol.% based on EBSD measurements. The ferrite mean linear intercept length was determined both in the compression direction and in the rolling direction. The average value determines the ferrite grain size.

EBSD maps were taken on a JEOL JSM 6500F high-resolution, high-intensity scanning electron microscope equipped with a field emission gun (FEG SEM) and for energy-dispersive X-ray analysis. The small beam diameter and its high brightness yield high-contrast Kikuchi patterns with a large signal to noise ratio. In this way, information about small orientation deviations can be obtained, even in deformed areas with high dislocation densities like phase or

grain boundaries [35,36]. A high-speed DigiView CCD camera was used for pattern acquisition. Data was recorded and analyzed using the EDAX/TSL OIM software package [37]. The lateral resolution of orientation microscopy using the FEG SEM was shown to be of the order of a few tens of nanometers, depending on the material investigated and the microscope, camera and software parameters used [37]. By choosing the highest possible image resolution for pattern acquisition and by optimizing the parameters of the Hough transformation, an angular resolution of about 0.3° can be obtained [37,38]. The step size was 50 nm for the UFG and FG steels and 200 nm for the CG steel. An acceleration voltage of 15 kV and an emission current of around $80 \mu\text{A}$ were used for all scans. Martensite was indexed as body-centered cubic ferrite. Due to its higher dislocation density, it can be easily distinguished from ferrite by its significantly lower image quality (IQ) and confidence index. In the present work, the minimum misorientation angle that defines a grain boundary was set to 2° . Misorientation angles between 2° and 15° are called low-angle grain boundaries (LAGBs). Misorientation angles larger than 15° are designated high-angle grain boundaries.

Slip-band evolution was studied on the basis of interrupted tensile tests using flat specimens ($5 \times 60 \times 3 \text{ mm}^3$). Sections containing rolling and normal directions were prepared by mechanical grinding and polishing. Two microhardness indents were placed within the center region of the specimen as a reference to measure the plastic strain after each tensile step. Micrographs and EBSD maps were taken within this distance. The scan position was easily recognized after each straining step due to the slight surface contamination.

2.3. Tensile testing

Cylindrical tensile test specimens with a diameter of 4 mm and a gage length of 20 mm were machined according to the German Industry Norm DIN 50125-B. Tensile tests were conducted at room temperature with a constant cross-head speed of 0.5 mm min^{-1} and an initial strain rate of $0.5 \times 10^{-3} \text{ s}^{-1}$. Due to the continuous yielding behavior of the DP steels, the yield strength is given as the 0.2% offset yield strength. In the case of the UFG as-received material, the lower yield strength is reported. The uniform elongation was determined as the strain at which the true strain equals the strain-hardening rate (Considère criterion). The strain-hardening exponent, n , was determined as an approximation to the Hollomon equation ($\sigma_t = k\varepsilon_t^n$, where σ_t is the true stress, ε_t is the true strain and k is an empirical constant) between 2% and uniform elongation for the DP steels and between the onset of continuous yielding and uniform elongation for the UFG as-received material. The reduction in area was determined by measuring the area of the fracture surface related to the initial cross section.

3. Results

3.1. Microstructures

The microstructure obtained after hot deformation and air cooling followed by intercritical annealing (CG route) consists of a ferrite matrix with a grain size of $12.4 \mu\text{m}$ and 31.3 vol.% martensite (Table 1), the latter occurring partly as isolated islands, partly as aligned bands.

By applying multi-pass warm deformation at 700°C (FG route) and at 550°C (UFG route) between hot deformation and intercritical annealing, the ferrite grain size is reduced to 2.4 and $1.2 \mu\text{m}$, respectively. The martensite fraction is 30.1 vol.% in the FG steel and 29.8 vol.% in the UFG steel. Exemplary micrographs are shown in Fig. 2. Note that the magnification is the same in all images. Upon BH, the microstructure does not change visibly in the scanning electron microscope, the ferrite grain size being $1.2 \mu\text{m}$ and the martensite volume fraction 28.2%.

As neither the chemical composition nor the intercritical annealing temperature or holding time was changed, all three steels contain similar martensite fractions with presumably similar martensite carbon contents. Using a mass balance calculation, the martensite carbon content C_m can be estimated from the equation:

$$C_m = \frac{C_c - C_f(1 - f_m)}{f_m} \quad (1)$$

where C_c is the carbon content of the composite, C_f is the carbon content of ferrite and f_m is the martensite volume fraction. The ferrite carbon content was estimated using thermo-calc [39]. It was assumed that, upon water quenching, the ferrite keeps the carbon content that is present at the temperature at which the austenite fraction is 30 vol.%. Thus, ferrite is supersaturated in carbon, the carbon content being 0.01 wt.%. Inserting this value in Eq. (1) yields a martensite carbon content of 0.54 wt.%, assuming that no cementite is present in the microstructure.

Other authors conducting similar investigations [24,27] found that phase transformation kinetics is enhanced upon grain refinement. Hence, they report a higher martensite volume fraction in their UFG materials after the same intercritical annealing treatment. The reason why the martensite volume fraction is nearly the same for all grain sizes in the present case is probably the different processing route applied. Due to the pronounced recovery during large-strain warm deformation, the stored energy in the initial microstructure might be lower than in the materials processed by ECAP or cold swaging. Hence, the driving force for phase transformation is not profoundly enhanced in the present case. This leads to the advantageous situation that in this study the differences in the mechanical properties can be solely attributed to the different grain size and these effects are not overlaid by differences in martensite volume fraction. However, it will be shown in the

Table 1
Microstructure parameters obtained from SEM micrographs and tensile tests presented as average value of three tensile specimens for each material.

Steel	MVF (%)	d_f (μm)	YS (MPa)	UTS (MPa)	UE (%)	TE (%)	RA (%)	Yield ratio	n -value
CG	31.3	12.4	445 \pm 17	870 \pm 25	7.2 \pm 0.7	7.7 \pm 1.0	13.0 \pm 4.4	0.51 \pm 0.01	0.21 \pm 0.01
FG	30.1	2.4	483 \pm 7	964 \pm 4	7.4 \pm 0.4	8.9 \pm 0.8	18.7 \pm 2.6	0.50 \pm 0.01	0.18 \pm 0.01
UFG	29.8	1.2	525 \pm 8	1037 \pm 15	7.1 \pm 0.5	7.3 \pm 0.4	15.3 \pm 4.0	0.51 \pm 0.01	0.18 \pm 0.01
UFG-BH	28.2	1.2	619 \pm 6	1005 \pm 5	8.6 \pm 0.2	11.4 \pm 1.5	37.5 \pm 0.9	0.62 \pm 0.003	0.16 \pm 0.004
UFG as-received	–	0.8	578 \pm 12	633 \pm 6	7.3 \pm 0.1	13.3 \pm 1.2	61.9 \pm 4.6	0.91 \pm 0.03	0.06 \pm 0.001

Standard deviations are given in brackets. MVF: martensite volume fraction; d_f : ferrite grain size (mean linear intercept length); YS: 0.2% offset yield strength; UTS: ultimate tensile strength; UE: uniform elongation; TE: total elongation; RA: reduction in area.

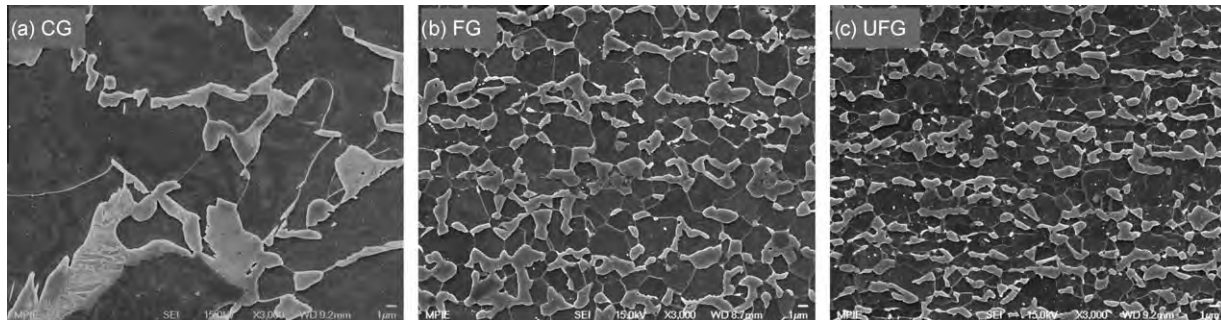


Fig. 2. Microstructures of the (a) CG material (12.4 μm ferrite grain size), (b) FG material (2.4 μm ferrite grain size) and (c) UFG material (1.2 μm ferrite grain size) produced by the processing routes illustrated in Fig. 1 plus intercritical annealing for 3 min at 730 $^{\circ}\text{C}$ in a salt bath, followed by water quenching. As the microstructure does not change visibly upon aging, this microstructure is not shown here.

following that the martensite distribution does have an influence on the mechanical behavior.

3.2. Tensile properties

Fig. 3 shows the engineering stress–strain curves of the CG, FG, UFG and UFG-BH steel. For each material, the result of only one of the three tensile tests is shown, because the variations within each series are rather small (see the standard deviations in Table 1). The CG, FG

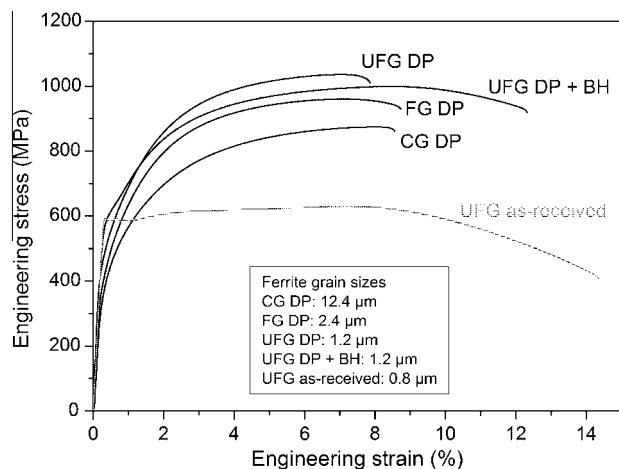


Fig. 3. Exemplary engineering stress–strain curves of the steels with CG, FG and UFG ferrite matrix and of the aged (BH) UFG steel. The UFG ferrite/cementite starting material is also shown. Initial strain rate: $0.5 \times 10^{-3} \text{ s}^{-1}$. DP refers to the term “dual-phase”.

and UFG steels show the typical characteristics of as-quenched ferrite/martensite dual-phase steels: low elastic limit, absence of a distinct yield point, continuous yielding and high initial strain-hardening rate. With decreasing grain size, the yield strength and the tensile strength are increased remarkably whereas uniform elongation and total elongation are only slightly affected. The BH process affects the mechanical properties in two ways: first, it promotes the reoccurrence of a yield point (though the transition between elastic and plastic deformation is still rather smooth); and second, it enhances the ductility considerably in terms of uniform elongation, total elongation and reduction in area. The tensile strength is slightly reduced due to BH. For comparison, the stress–strain curve of the as-received UFG material is also shown. While the yield strength is slightly higher than in the UFG-DP steel, the strain-hardening rate is much lower, resulting in a relatively low tensile strength. The onset of plastic deformation is characterized by pronounced Lüders straining. The uniform elongation is the same as in the UFG-DP steel, but lower than in the bake-hardened UFG-DP steel. The total elongation is higher than in the other investigated steels; this is ascribed to the large post-uniform plasticity.

Table 1 lists the average values of each steel obtained from three separate tensile tests. The yield strength (0.2% offset yield strength) and tensile strength increase linearly with the inverse square root of the ferrite grain size, i.e. the Hall–Petch relation is obeyed. The grain size dependence (Hall–Petch slope) is $4.0 \text{ MPa}/d^{-1/2}$ for the yield strength (with d being the grain diameter in mm), and $8.39 \text{ MPa}/d^{-1/2}$ for the tensile strength. As yield and tensile

strength are increased by nearly the same factor due to grain refinement, the yield ratio is nearly constant. The bake-hardened UFG steel does not coincide with these trends. The 0.2% offset yield strength is increased by 94 MPa compared to the as-quenched UFG steel and the tensile strength is decreased by 32 MPa, resulting in a change in the yield ratio from 0.51 to 0.62. As the yield point after BH is more pronounced yet still not sharp, it is reasonable to specify the 0.2% offset yield strength rather than the lower yield strength.

The effect of grain refinement on ductility is more complex than its effect on strength. The uniform elongation (Table 1) is nearly constant around 7% for the CG, FG and UFG steels. Bake-hardening increases uniform elongation to around 8.6%. Regarding only the as-quenched materials, both total elongation and reduction in area are highest in the FG steel. The UFG steel has a lower total elongation than the CG steel but a higher reduction in area. However, the differences are rather small. The BH treatment improves the total elongation by 2.5% and – more significantly – the reduction in area by 22.2%.

The analysis of the strain-hardening rate (Fig. 4) reveals that the initial strain-hardening rate is increased by grain refinement but is nearly the same for the FG and UFG steels. At higher strain levels, the two curves converge with the curve of the CG steel, i.e. the effect of grain refinement continuously decreases. The bake-hardened steel starts with lower strain-hardening rates in the range of the CG steel (for $\epsilon_t > 0.01$). The curve shows a minimum in the initial stage due to the more pronounced yield point. At higher strain levels, it intersects the other curves, achieving a higher uniform strain. The n -value, calculated at strain levels between 2% and uniform elongation (Table 1), drops off slightly from 0.21 for the CG steel to 0.18 for the FG and UFG steels and becomes 0.16 for the bake-hardened steel. The n -value of all DP steels is considerably larger than in the UFG ferrite/cementite starting material.

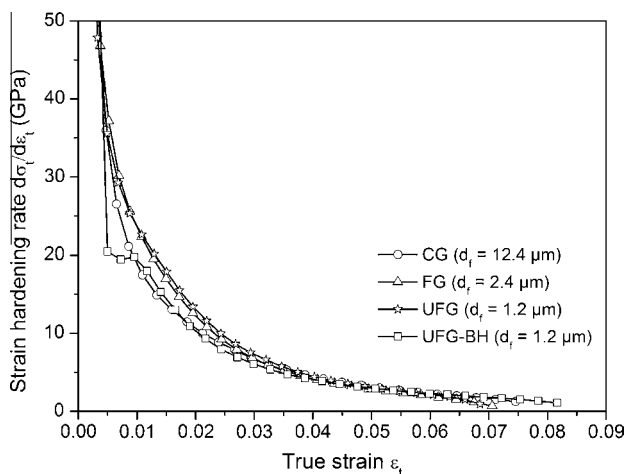


Fig. 4. Strain-hardening rate as a function of true strain. Grain refinement increases the initial strain-hardening rate, whereas BH decreases it. CG, FG, UFG and UFG-BH are as defined in the text.

Fig. 5 shows the tensile specimens after failure. The degree of necking (post-uniform elongation) increases with decreasing grain size and is strongest for the bake-hardened specimens. The micrographs reveal the respective fracture modes of the steels. In the case of the CG steel, it is mainly brittle, which is documented by well-defined facets and cleavage steps on these facets (Fig. 5a). Only some small areas consist of dimples. The latter are located in the martensitic area, whereas the ferrite exhibits cleavage planes, as was observed previously [40,41]. The dominant fracture mode of the FG steel is ductile, although smaller parts of the specimen have undergone brittle fracture (Fig. 5b). The UFG steel shows dimples throughout the specimens, in both the as-quenched (Fig. 5c) and bake-hardened conditions (Fig. 5d). This suggests a failure process of void nucleation and growth, and hence entirely ductile fracture. Some dimples are formed around inclusions.

In order to identify the preferred void nucleation sites, surfaces perpendicular to the fracture surface were also analyzed. In the CG steel, the main fracture mechanism is martensite cracking. The cracks form mostly in the banded areas perpendicular to the applied tensile strain (Fig. 6a). Most of the cracks stop at the ferrite/martensite interface, but some penetrate into a minor fraction of the adjacent ferrite grain. Martensite fracture was observed at strains as low as 3.4% plastic strain (see below). Void nucleation and growth along ferrite/martensite interfaces occur to a lesser extent within the areas of isolated martensite islands. In the FG and UFG steels, the voids form primarily at ferrite/martensite interfaces and are distributed more homogeneously (Fig. 6b). Martensite cracking takes place less frequently in martensite islands that are of larger than average size and occurs only after necking has started.

3.3. Microstructure evolution during tensile straining

The microstructure evolution during deformation is illustrated for the CG, UFG and UFG-BH steels. The FG steel shows an intermediate deformation behavior. Fig. 7 shows EBSD scans taken perpendicular to the fracture surface of the tensile specimen. In the left column, the IQ maps of areas within the uniform elongation (~7%) are illustrated. The center and right columns show the IQ and inverse pole figure (IPF) maps of areas close to the neck. Martensite is easily identified by its lower IQ and its subdivision into blocks or packets. In all images, the tensile direction (=rolling direction) is horizontal and the normal direction is vertical.

Upon straining to uniform elongation (UE), strain localization in ferrite was observed in the CG steel, as indicated by arrows 1 in Fig. 7a. Locally, a dislocation substructure with vague boundaries has developed (arrow 2). Martensite cracking occurred in some areas (arrow 3). In contrast, the UFG steel shows a less pronounced substructure formation in ferrite. Instead, martensite has undergone considerable deformation and is rotated towards the tensile direction together with the ferrite (arrows in Fig. 7d). The

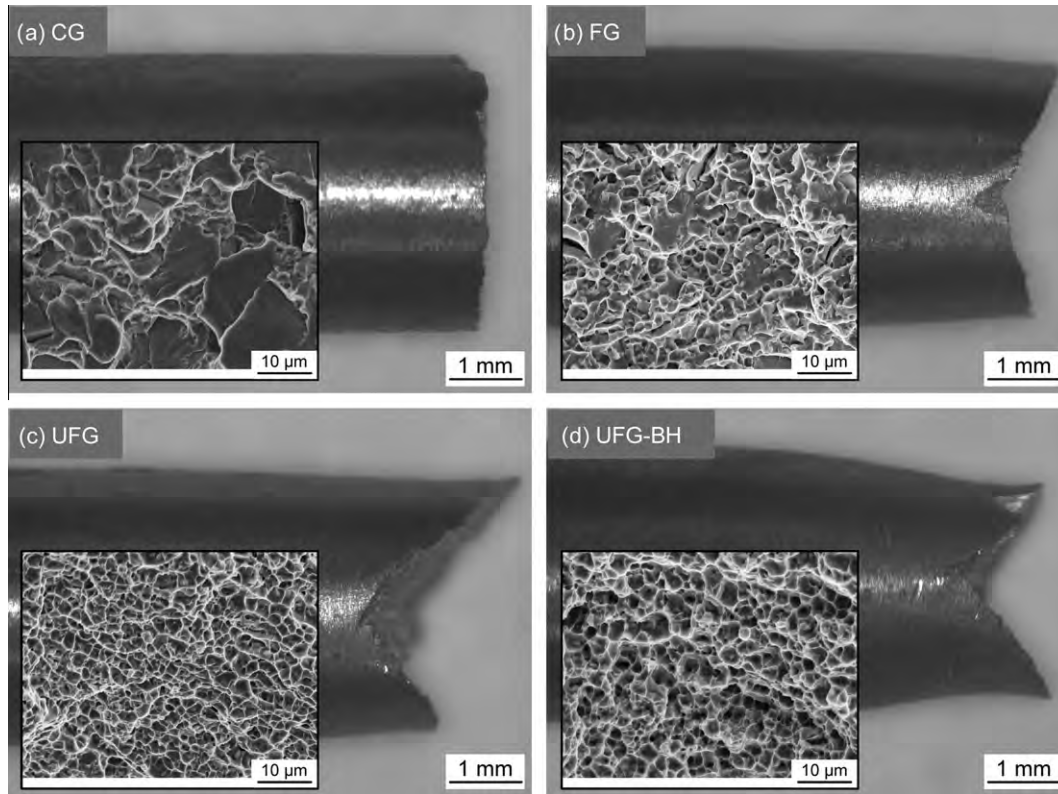


Fig. 5. Tensile specimen after failure showing the increase in post-uniform elongation with decreasing grain size and the promotion of ductile fracture mechanism (a–c). The aging treatment (BH, BH) enhances this trend (d). CG, FG, UFG and UFG-BH are defined in the text.

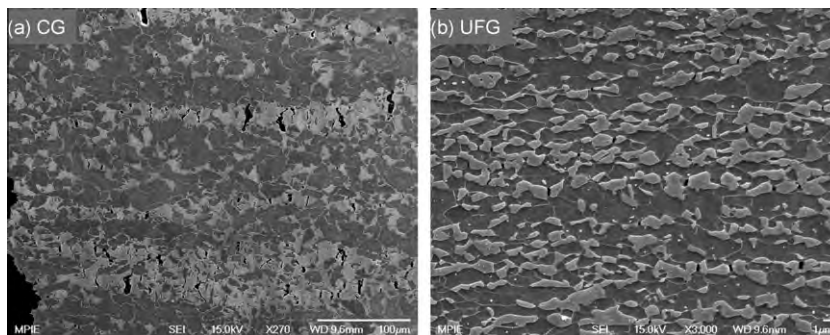


Fig. 6. Observation of the planes perpendicular to the fractured tensile specimen surfaces reveals (a) martensite cracking as the main fracture mechanism in the CG specimen and (b) void nucleation and growth in the UFG specimen. Note the different magnification of the images. The tensile direction is horizontal; the normal direction is vertical.

same is true for the UFG-BH steel. Nevertheless, the martensite is even more deformed compared to the non-bake-hardened state, as is revealed by the more elongated shape of the martensite islands (Fig. 7g).

After failure, strain localization and substructure formation of the CG ferrite is intense, particularly close to ferrite/martensite interfaces. Martensite cracking and interface decohesion are commonplace in this state (arrows in Fig. 7b), while plastic deformation of martensite is not obvious. In the UFG steel (Fig. 7e), it can be easily seen that the martensite is extensively deformed and elongated

in the tensile direction. Compared to the CG steel, the deformation substructure in the ferrite is less well developed. Moreover, the distribution of the deformation substructure within the ferrite grains is more homogeneous than in the CG structure. Thus, it seems that strain localization and dynamic recovery are less active in the UFG steel than in the CG steel. On the other hand, the plastic deformation of martensite is more intense. Voids form mainly along the ferrite/martensite interface (arrows in Fig. 7e) and are also elongated in the tensile direction. In the bake-hardened condition, martensite plasticity is

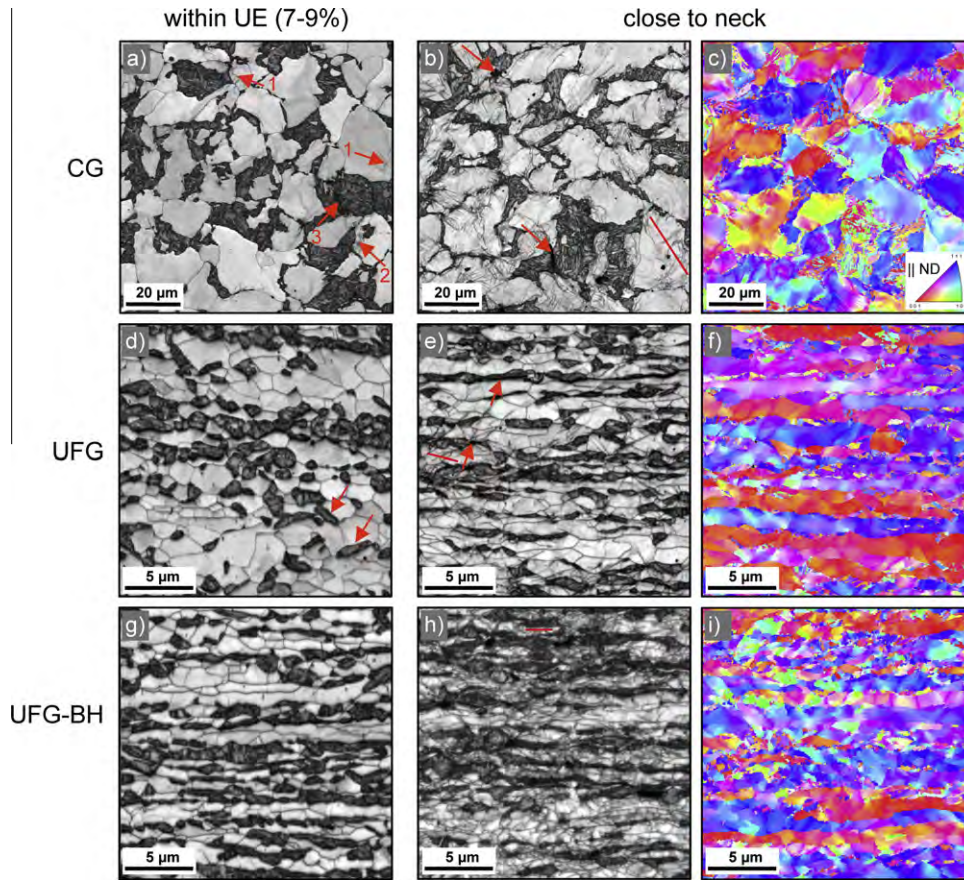


Fig. 7. EBSD maps taken perpendicular to the fracture surface of the CG specimen (a–c), the UFG specimen (d–f) and the UFG-BH specimen (g–i). (a, d, g) IQ maps of areas within the area of UE. IQ maps taken close to the neck (b, e, h) and the respective IPF maps (c, f, i) show the microstructure evolution during straining. The tensile direction is horizontal and equals the rolling direction; the normal direction is vertical.

further enhanced. As indicated by the much higher reduction in area compared to the CG and UFG steels, a subgrain structure is widely developed in the UFG-BH steel.

The IPF maps reflect the different types of strain accommodation in ferrite. The substructure formation in the CG steel results in pronounced orientation gradients which are randomly distributed within the ferrite grains (Fig. 7c), whereas the deformation of the UFG steel results in more planar arrays of crystal orientations in an angle around 40° to the tensile direction (Fig. 7f). The IPF map of the UFG-BH looks similar, yet the subgrain formation is reflected by a finer subdivision of the ferrite grains.

In Fig. 8, typical misorientation profiles of the different ferrite substructures after failure are presented. Their positions are indicated on the respective IQ maps (red¹ lines in Fig. 7b, e and h). From these profiles, it is evident that the UFG-BH sample is the only one which exhibits full development of subgrains that are separated by LAGBs. This is revealed by the stepwise increase in the misorientation angle. The presence of fully developed subgrains indicates that dynamic recovery was active in the necked area of

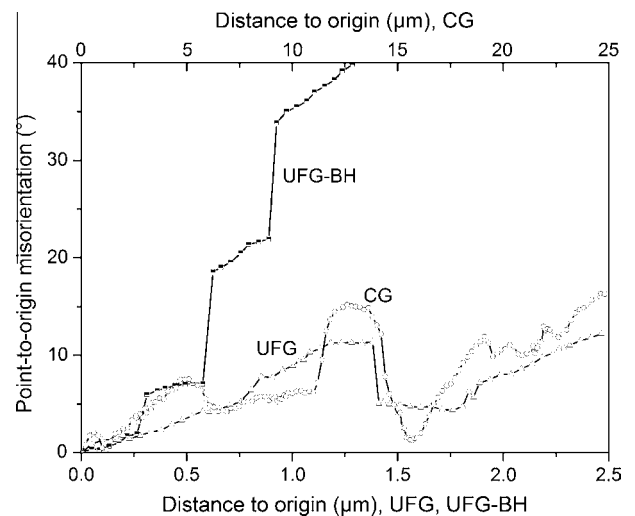


Fig. 8. Point-to-origin misorientation profiles for the UFG and the UFG-BH samples (lower x-axis) compared to CG sample (upper x-axis), taken from EBSD maps close to the neck. Subgrain formation is completed only in the UFG-BH sample.

¹ For interpretation of color in Fig. 7, the reader is referred to the web version of this article.

the bake-hardened sample. In the other two specimens, plastic deformation leads to pronounced orientation gradients and to a less extent to well-defined subgrains. This

gives rise to more gradually increasing misorientation profiles. Note the different scaling for the CG sample, which indicates a larger size of the subgrains to be formed. The subgrain size of the UFG-BH steel is around 0.3 μm .

The microstructure evolution during deformation was studied in more detail by interrupted tensile tests. The UFG-BH was excluded from this part of the investigation because the tempered state of the microstructure obviously alters the deformation mechanisms and therefore it is not comparable to the untempered state. Although the EBSD scans revealed important information about the deformation substructure, single slip bands cannot be distinguished. Therefore, the evolution of slip bands was studied on polished samples subjected to different strain levels. The CG ferrite exhibits wavy and strongly intersecting slip bands without preferred orientation after 3.4% plastic strain (Fig. 9a). In contrast, the UFG ferrite basically shows two sets of nearly planar slip bands which are oriented around 40° to the tensile direction, as was observed in the IPF maps (Fig. 9b). This suggests that less pronounced orientation gradients are developed in the UFG steel at this strain than in the CG steel, as was observed in the IPF

maps in Fig. 7. This assumption was further tested by analyzing the evolution of local misorientations at small strains. For this purpose, the kernel average misorientation (KAM) was used which can be directly retrieved from the EBSD data.

The KAM is defined as the average misorientation angle between an EBSD measurement point and all its neighbors at a certain distance. Given that the KAM angle is strongly dependent on the distance selected, the nearest neighbor used for the calculation was determined based on the following considerations: the distance has to be sufficiently small to ensure that detailed information about local misorientation changes is not ignored and that influences stemming from neighboring grains are not taken into account. At the same time, the distance must allow for averaging out scatter due to the spatial resolution limits of EBSD and for performing the calculations with misorientations above the angular EBSD resolution limit [44]. Hence, for both samples, the CG and the UFG material, neighboring points located at a distance of 200 nm spacing were selected. Misorientation angles above 5° were excluded from the calculation. This angle is large enough to still

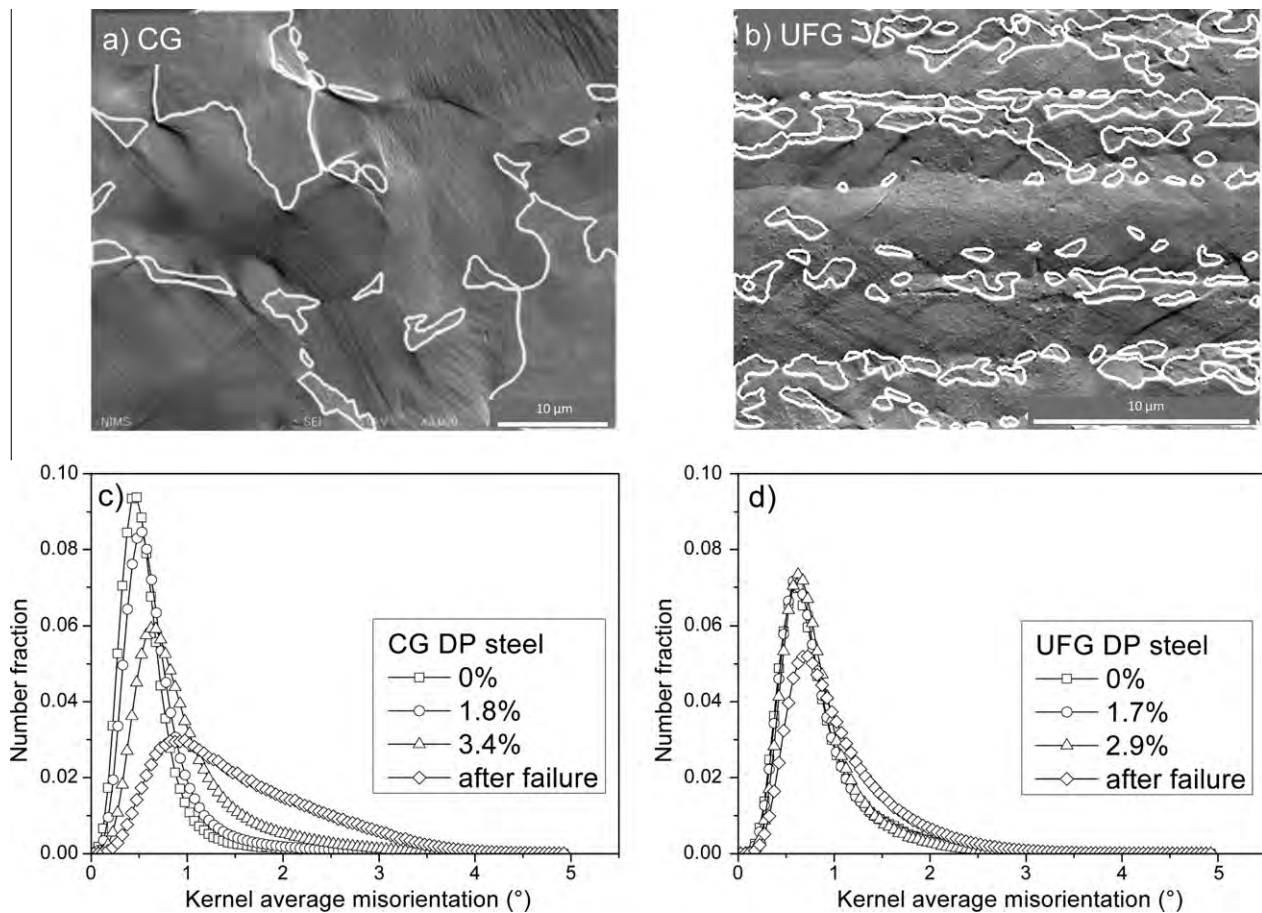


Fig. 9. The CG steel exhibits wavy slip bands (a), whereas slip-band formation in the UFG sample follows a more planar mode (b). The tensile direction is horizontal. The distribution of the KAM values (calculated using neighboring EBSD points at a distance of 200 nm and up to a maximum deviation angle of 5°) at different strain levels in the same sample area shows that lattice rotations take place early during tensile straining in the CG steel (c), whereas they appear delayed in the UFG specimen (d) due to the more constrained plastic deformation in ferrite. The rolling direction is horizontal; the normal direction is vertical.

include in the analysis the subgrains that evolve during plastic deformation, yet is small enough to exclude neighboring grains from the calculation.

The calculation was done at different strain levels on the same sample area. Only the ferrite fraction was taken into account. The results are shown in Fig. 9c and d. In the CG steel, a uniform shift of the peak KAM value to higher misorientation angles and a gradual increase in the fraction of higher misorientation angles are observed. The flattening of the curve indicates that strain is distributed inhomogeneously throughout the ferrite grains. A larger fraction of high misorientation points to the increasing number of dislocation walls or subgrains. The peak value of the KAM at 0% strain is lower in the UFG steel than in the CG steel due to the larger fraction of dislocations at grain boundaries. Up to 3% plastic strain, the KAM distribution remains unchanged. Only after failure was a considerable decrease in the peak value found, accompanied by an increased fraction of high misorientation angles. Hence, the planar slip mode in the UFG steel correlates with restricted lattice rotations and thus delayed subgrain formation. In contrast, non-planar glide, including the intense lattice rotations and earlier formation of a substructure, prevail in the CG steel.

4. Discussion

For the sake of clarity, the discussion of the deformation and fracture mechanisms will focus on the as-quenched specimens only. The effect of BH on deformation and fracture behavior will be addressed in a separate section.

4.1. Deformation mechanisms

In general, the enhancement of strength due to grain refinement is accompanied by a deterioration of ductility. However, it was shown in previous studies [23–28] that this does not apply to DP steels. Instead, it was found that uniform and total elongation are only slightly affected by decreasing ferrite grain size – as was also observed in the present study. This is partly a consequence of the increase in the initial strain-hardening rate with decreasing grain size [25,27,42,43]. In a recent paper [44], the enhancement of the initial strain-hardening rate was explained in terms of reductions in the martensite island size and ferrite grain size. These effects were suggested to enhance the number of dislocation sources and give rise to rapid dislocation interactions. The higher ferrite/martensite phase boundary fraction results in a larger number of GNDs, which are generated during plastic deformation due to the strain incompatibility of the two phases. Furthermore, the back stresses exerted by (i) martensite islands and (ii) ultrafine ferrite grains below $1\ \mu\text{m}^3$, which are characterized by a more uniform dislocation distribution than larger grains, contribute to the rapid stress increment. It is assumed that the deformation-induced transformation of small amounts of retained austenite plays a secondary role.

When focusing on low strain levels (<2%), it must be stated that the increase in yield strength due to ferrite grain refinement contributes to the high initial strain-hardening rate. Due to the absence of a distinct yield point, it is not possible to clearly distinguish between the effect of grain size on strain-hardening rate and that on yield strength. This becomes clear when looking at the strain-hardening rate of the UFG-BH steel, which is nearly equal to the strain-hardening rate of the CG steel. To establish a consistent comparison of the strain-hardening capacity of UFG ferrite/cementite and UFG ferrite/martensite steels, it is thus necessary to analyze UFG ferrite/martensite steels after strain aging, which exhibit a distinct yield point.

The aspect that shall be treated in more detail in the present study is the plasticity of martensite, which is considerably enhanced due to grain refinement. In general, plastic yielding starts in the soft ferrite, with the hard martensite remaining in the elastic state. During the plastic deformation of the ferrite, stress is transferred to the martensite. Internal stresses at the ferrite/martensite interface are built up due to the plastic strain incompatibility. At this stage, the strain-hardening rate is very high as a consequence of rapid dislocation multiplication and the back stresses resulting from the strain incompatibility. When the transferred stress is large enough to reach the elastic limit of the martensite, it starts to deform plastically. Due to the high initial strain hardening of the martensite, the stress increment in the composite is still very high. Only after the martensite flow curve levels off, its contribution to the strain-hardening rate of the composite declines [45]. From these general considerations, it is clear that martensite plasticity is an important factor controlling the overall deformation behavior of DP steels. Generally, the ability of martensite to deform increases with a decay in hardness, which can be reduced by lowering the carbon content or by applying tempering. In view of a composite, a lower strength difference between martensite and ferrite promotes plastic deformation of martensite [46]. Although some studies have reported that plastic deformation of martensite occurs only after uniform elongation (e.g. [42,47]), considerable martensite deformation at lower strains was shown by in situ SEM studies [48,49] and by analyzing the two-stage deformation behavior derived from the strain-hardening rate [25]. In the present materials, both types of behavior have been observed. The martensite in the CG steel seems to remain in the elastic state even in the necked area of the tensile specimen. On the other hand, the FG and UFG steels clearly show considerable martensite deformation before the onset of necking. According to the model developed by Jiang et al. [25], the increase in the yield strength and the strain-hardening rate of the ferrite matrix due to grain refinement results in rapid stress transfer to martensite. Thus, the yield stress of martensite is reached at lower strains than in coarser-grained microstructures. However, it must be assumed that the yield strength of martensite also increases with grain refinement due to the finer packet size. This, in turn, would delay martensite plastic deformation.

In order to identify the reason for the enhanced martensite plasticity due to grain refinement, one has to consider how stress and strain are partitioned between ferrite and martensite. In this respect, the slip-band evolution reveals important information about plastic strain accommodation. In the CG steel, the slip bands appear wavy (Fig. 9a), whereas in UFG steel a more planar slip-band formation is active (Fig. 9b). Planar and wavy slip modes in DP steels were reported by Tomota [50]. Tomota explains the occurrence of planar slip with the restricted operation of plastic relaxation of strain incompatibility while the wavy slip mode is associated with active plastic relaxation. Plastic relaxation can be realized by (i) additional plastic flow in the softer phase, (ii) onset of plastic flow in the harder phase, (iii) fracture of the harder phase or (iv) decohesion at the interface. In the CG steel, plastic relaxation can take place by strain localization and substructure formation in ferrite and by martensite cracking (Fig. 7a and b). Therefore, slip bands develop in a wavy mode (Fig. 9a). This deformation mechanism is accompanied by intense lattice rotations, which are reflected by the gradual increase in local misorientations (Fig. 9c). The finer the ferrite grain size is, the more difficult the plastic deformation of ferrite becomes due to the restricted formation of dislocation pile-ups. The restricted ferrite plasticity is reflected by the planar slip mode (Fig. 9b) and only a few lattice rotations (Fig. 9d). Due to the nearly spherical shape and the resulting high toughness of the martensite islands, both interface decohesion and cracking are impeded at low strains. At later stages of plastic deformation (more than 3%), plastic relaxation in the UFG steel occurs by the onset of martensite plastic flow and by interface decohesion (Fig. 7e). Hence, the plasticity of martensite is strongly dependent on the plastic constraints in the ferrite. The plastic constraint imposed on UFG ferrite is balanced by the more spherical morphology of UFG martensite compared to the CG martensite, the latter often covering ferrite grain boundaries. At a constant martensite volume fraction, the spherical shape toughens martensite and increases the ductility of the composite. Therefore, the UFG steel shows ductility comparable to that of the CG steel at much higher strength levels due to the advantageous morphology and distribution of martensite and the ability of martensite to deform plastically as a response to the restricted plasticity in ferrite.

It is evident from these observations that stress/strain partitioning, which is essential in this type of composite structure, changes significantly upon grain refinement. In the CG steel, stress/strain partitioning is extensive in the sense that martensite carries the major part of the stress and ferrite carries the major part of the strain. This leads to strain localization in ferrite and to early cracking of martensite. Upon grain refinement, ferrite is strengthened more than martensite, as the yield strength of martensite is mainly a function of its carbon content, which is supposed to be nearly constant in all investigated materials. In partic-

ular, ferrite grains below $1\ \mu\text{m}^3$ will act as a load-carrying phase. Using three-dimensional EBSD measurements, these grains were shown to be often entirely prestrained by the volume expansion accompanying the austenite-to-martensite phase transformation [44]. Thus, the hardness difference between ferrite and martensite is presumably decreased due to grain refinement. In this situation, the hard phase (martensite) is forced to undergo plastic deformation at lower strains [45]. Thus, stress and strain are partitioned more evenly between martensite and ferrite in the UFG material. This leads to less severe strain incompatibility at the ferrite/martensite interface, resulting in better interface cohesion, and therefore to delayed void formation and an improved post-uniform elongation (Fig. 5).

More research is needed to fully understand the deformation mechanisms in this UFG composite structure. In this respect, digital image correlation is a suitable technique to quantify the strains accommodated by ferrite and martensite [48,51], and will be applied in the future. Furthermore, the hardness difference between ferrite and martensite in the different materials shall be quantified using nanoindentation.

4.2. Fracture mechanisms

Grain refinement promotes ductile fracture mechanisms (Fig. 5). In the CG material, brittle fracture behavior is favored due to martensite banding, a large martensite island size and unfavorable distribution along ferrite grain boundaries. Voids and cracks are distributed mainly around martensite bands (Fig. 6), where local stresses concentrate. As stress is transferred to martensite during tensile straining of DP steels, the fracture stress in martensite is reached much earlier than in ferrite. Therefore, fracture of martensite is initiated. Martensite cracking is facilitated by (i) the low toughness of the martensite islands and (ii) the presence of former austenite–austenite grain boundaries, which are known to be brittle due to their high susceptibility to segregations [52]. The initiated microcracks impose a high shear stress on the neighboring ferrite, which increases with the martensite effective grain size. Hence, failure of coarse martensite islands leads to cleavage fracture of ferrite [53]. As a consequence, premature martensite cracking controls both tensile strength and uniform elongation in the CG steel.

In the FG and UFG steels, martensite cracking is less frequent as a result of the enhanced martensite plasticity and the better interface cohesion as described above. By deforming, martensite releases part of the local stress concentrations and retards void formation, which results in higher fracture strains. Moreover, it is known that the plastic strain needed for the failure of a particle (or grain) increases with decreasing particle size. This is explained by the smaller number of dislocations piling-up at grain and phase boundaries, which result in lower shear stresses [41]. If martensite failure occurs, the produced cracks are not large enough to initiate cleavage fracture of the adjacent

ferrite. This is because the length of the crack, which determines the peak stress at the crack tip, is restricted by the grain size. Thus, grain refinement increases the cleavage fracture stress and promotes ductile fracture mechanisms at room temperature.

These findings are similar to the results of Kim and Thomas [54], who found that coarse DP structures fracture predominantly by cleavage, while both fine fibrous and fine globular structures fracture in a ductile manner. They attribute this behavior to the constrained possibility of deformation localization in the fine structures, which reduces the probability of cleavage crack nucleation in ferrite. Indeed, the observed strain localization in the CG material is likely to induce cleavage fracture in ferrite. As less excess strain is generated in UFG ferrite, less excess stress is exerted on the martensite phase. Thus, the more even stress and strain partitioning promotes the void nucleation and growth process that is characteristic of ductile fracture behavior. In the CG steel, more stress is transferred to martensite, leading to premature local fracture of martensite and mainly brittle fracture behavior with nearly absent post-uniform elongation.

4.3. Aging response of the UFG material

The BH (aging) process induces static strain aging phenomena in the ferrite and tempering phenomena in the martensite [55]. Carbon atoms in solid solution form Cottrell atmospheres around dislocations and grain boundaries or precipitate as transition carbides in ferrite and/or martensite [56]. The diffusion of carbon includes a volume decrease in martensite, which reduces the internal stresses in ferrite. The formation of Cottrell atmospheres around dislocations causes (partial) pinning of these dislocations. In addition to the reduction in internal stresses, this leads to the reoccurrence of a more distinct yield point and to an increase in the yield strength. In the present case, no sharp yield point was regenerated after BH, but the 0.2% offset yield strength increases by nearly 100 MPa. The dislocation pinning and release of internal stresses successfully suppressed the early onset of plastic deformation of ferrite. The strengthening effect of carbon precipitation is accompanied by a loss in hardness due to the removal of supersaturated carbon in solid solution. This effect might be the reason for the reduction in tensile strength by 32 MPa after BH. Similar findings were proposed by Tanaka et al. [57], who attribute the decrease in tensile strength to the reduction in the amount of excessively dissolved carbon in ferrite. This was experimentally confirmed by Nakaoka et al. [58]. The combined effects of the increase in yield strength and decrease in tensile strength are assumed to be the reason for the lower strain-hardening rate compared to the non-bake-hardened steel (Fig. 4).

The effect of BH on yield strength is more pronounced than on tensile strength, which is consistent with the findings on CG DP steels [59]. The common explanation is that aging phenomena, including the formation of Cottrell

atmospheres around dislocations, mainly affect the onset of yielding by restricting the dislocation motion, thereby increasing the yield strength. As soon as the dislocations tear off the Cottrell atmospheres, yielding and strain hardening are controlled by dislocation motion and multiplication, as well as by the hardness difference between the phases. Hence, aging phenomena play a minor role in the strain range of the tensile strength.

The most remarkable effect of BH is the increase in total elongation and reduction in area. One reason for the increased ductility might be the above-mentioned decrease in ferrite hardness due to a loss of dissolved carbon, as was suggested by Koo and Thomas [60]. The other reason is the decrease in martensite hardness due to tempering effects. Decreasing the hardness of martensite increases the critical strain required for interface decohesion or martensite cracking. As a consequence, extensive deformation of martensite was found in the necked area of the tensile specimen (Fig. 7h). As the martensite plasticity retards the formation of voids, plastic deformation of ferrite can continue. Therefore, a rather homogeneous subgrain structure in the ferrite is formed close to the necking zone of the UFG-BH sample (Figs. 7h and 8). The beneficial effect of tempering on decreasing the strength of martensite and, therefore, promoting its plastic deformation was documented for coarser-grained microstructures by Kang et al. [48] and Mazinani and Poole [61].

5. Conclusions

Three low-carbon dual-phase steels with nearly constant martensite fraction around 30 vol.% martensite and different ferrite grain sizes (1.2, 2.4 and 12.4 μm) were produced by applying hot deformation and large-strain warm deformation at different deformation temperatures, followed by intercritical annealing. Their deformation and fracture mechanisms were studied based on tensile test data and microstructure observations. The BH response was investigated for the UFG steel. The main conclusions are:

- Grain refinement leads to an increase in both yield strength and tensile strength following a linear relationship of the Hall–Petch type. Uniform elongation and total elongation are hardly affected. The initial strain-hardening rate and the reduction in area increase as the grain size decreases.
- The increase in the initial strain-hardening rate due to grain refinement is attributed to early dislocation interactions, the high number of dislocation sources and the back stresses exerted by (i) martensite islands and (ii) very small ferrite grains below 1 μm^3 .
- Aging at 170 °C (bake-hardening) of the UFG steel leads to a strong increase in yield strength and a small decrease in tensile strength. Ductility is enhanced in terms of uniform and total elongation. Reduction in area is improved by 22% (from 15.3% to 37.5%). These effects are attributed to dislocation locking, relaxation of

internal stresses, reduction in supersaturated interstitial carbon content in ferrite and tempering effects in martensite.

- Grain refinement leads to plastic constraints in the ferrite matrix, which is reflected by homogeneous planar slip-band arrays. Strain localization in CG ferrite is accomplished by wavy slip bands. The wavy slip mode leads to pronounced lattice rotations and early formation of a substructure in CG ferrite, whereas the planar slip mode provokes less lattice rotations. The plastic constraints in FG and UFG ferrite force martensite to deform plastically earlier during tensile straining, whereas strain localization and subgrain formation are impeded.
- The increase in strength at improved ductility due to grain refinement is attributed to the combined effect of strengthened ferrite and enhanced toughness of martensite. This leads to less severe stress/strain partitioning and better interface cohesion.
- Grain refinement promotes ductile fracture mechanisms. Besides the beneficial effects of less excess strain in ferrite and less excess stress in martensite, the formation of martensite cracks and cleavage fracture in ferrite is suppressed in the FG and UFG steels due to the small size, the more homogeneous distribution and the more spherical shape of martensite islands.

References

- [1] Howe AA, et al. ECSC contract 7210.PR/167. Luxembourg: EC; 2000.
- [2] Song R, Ponge D, Raabe D, Speer JG, Matlock DK. *Mater Sci Eng A* 2006;441:1.
- [3] Hodgson PD, Hickson MR, Gibbs RK. *Mater Sci Forum* 1998;284–302:63.
- [4] Song R, Ponge D, Raabe D, Kaspar R. *Acta Mater* 2005;53:845.
- [5] Yada H, Matsumura Y, Nakajima K. US patent 4466,842. Tokyo, Japan: Nippon Steel Corporation; 1984.
- [6] Ohmori A, Torizuka S, Nagai K. *ISIJ Int* 2004;44:1063.
- [7] Ueji R, Tsuji N, Minamino Y, Koizumi Y. *Acta Mater* 2002;50:4177.
- [8] Valiev RZ, Langdon TG. *Prog Mater Sci* 2006;51:881.
- [9] Saito Y, Utsunomiya H, Tsuji N, Sakai T. *Acta Mater* 1999;47:579.
- [10] Ivanisenko Y, Lojkowski W, Valiev RZ, Fecht HJ. *Acta Mater* 2003;51:5555.
- [11] Park KT, Shin DH. *Metall Mater Trans A* 2002;33:705.
- [12] Hanamura T, Yin F, Nagai K. *ISIJ Int* 2004;44:610.
- [13] Song R, Ponge D, Raabe D. *Acta Mater* 2005;53:4881.
- [14] Azizi-Alizamini H, Militzer M, Poole WJ. *Scr Mater* 2007;57:1065.
- [15] Zhang ZL, Liu YN, Zhu JW, Guang YU. *Mater Sci Forum* 2007;551–552:199.
- [16] Shin DH, Park K-T. *Mat Sci Eng A* 2005;410–411:299.
- [17] Hayami S, Furukawa T. In: Korchynsky M, editor. *Microalloying 75 proceedings of an international symposium on high-strength, low-alloy steels*. New York: Union Carbide Corporation; 1977. p. 311.
- [18] Speich GR, Miller RL. In: Kot RA, Morris JW, editors. *Structure and properties of dual-phase steels*. New York: The Metallurgical Society of AIME; 1979. p. 145.
- [19] Moyer JM, Ansell GS. *Metall Trans A* 1975;6:1785.
- [20] Bourell DL, Rizk A. *Acta Metall* 1983;31:609.
- [21] Davies RG. *Metall Trans A* 1978;9:41.
- [22] Rigsbee JM, Vander Arend PJ. In: Davenport AD, editor. *Formable HSLA and dual-phase steels*. New York: The Metallurgical Society of AIME; 1979. p. 58.
- [23] Chang PH, Preban AG. *Acta Metall* 1985;33:897.
- [24] Delincé M, Brechet Y, Embury JD, Geers MGD, Jacques PJ, Pardoën T. *Acta Mater* 2007;55:2337.
- [25] Jiang ZH, Guan ZZ, Lian JS. *Mater Sci Eng A* 1995;190:55.
- [26] Mukherjee K, Hazra SS, Militzer M. *Metall Mater Trans A* 2009;40A:2145.
- [27] Son YI, Lee YK, Park KT, Lee CS, Shin DH. *Acta Mater* 2005;53:3125.
- [28] Tsipouridis P, Werner E, Kremaszky C, Tragl E. *Steel Res Int* 2006;77:654.
- [29] Calcagnotto M, Ponge D, Raabe D. *ISIJ Int* 2008;48:1096.
- [30] Mukherjee K, Hazra S, Petkov P, Militzer M. *Mater Manuf Process* 2007;22:511.
- [31] Song R. *Microstructure and mechanical properties of UFG C–Mn steels*. Aachen: Shaker Verlag; 2005.
- [32] Song R, Ponge D, Raabe D. *ISIJ Int* 2005;45:1721.
- [33] Kaspar R, Pawelski O. *Materialprüfung* 1989;31:14.
- [34] Pawelski O, Kaspar R. *Materialprüfung* 1988;30:357.
- [35] Humphreys FJ. *J Mater Sci* 2001;36:3833.
- [36] Schwartz AJ, Kumar M, Adams BL, Field DP. *Electron backscatter diffraction in materials science*. New York: Springer; 2009.
- [37] Dingley D. *J Microsc-Oxford* 2004;213:214.
- [38] Bate PS, Knutsen RD, Brough I, Humphreys FJ. *J Microsc-Oxford* 2005;220:36.
- [39] Jansson B, Schalin M, Selleby M, Sundman B. In: Bale CW, Irons GA, editors. *Computer software in chemical and extractive metallurgy*. Quebec: The Metallurgical Society of CIM; 1993. p. 57.
- [40] Cai XL, Feng J, Owen WS. *Metall Trans A* 1985;16:1405.
- [41] He XJ, Terao N, Berghezan A. *Met Sci* 1984;18:367.
- [42] Balliger NK, Gladman T. *Met Sci* 1981;15:95.
- [43] Calcagnotto M, Ponge D, Raabe D. *Mater Sci Eng A* 2010;527:7832–40. doi:10.1016/j.msea.2010.08.062.
- [44] Calcagnotto M, Ponge D, Demir E, Raabe D. *Mater Sci Eng A* 2010;527:2738.
- [45] Fischmeister H, Karlsson B. *Z Metallkd* 1977;68:311.
- [46] Lian J, Jiang Z, Liu J. *Mater Sci Eng A* 1991;147:55.
- [47] Marder AR. *Metall Trans A* 1982;13:85.
- [48] Kang JD, Ososkov Y, Embury JD, Wilkinson DS. *Scr Mater* 2007;56:999.
- [49] Su YL, Gurland J. *Mater Sci Eng* 1987;95:151.
- [50] Tomota Y. *Mater Sci Technol* 1987;3:415.
- [51] Ghadbeigi H, Pinna C, Celotto S, Yates JR. *Mater Sci Eng A* 2010;527:5026.
- [52] Becker J, Hornbogen E, Stratmann P. *Z Metallkd* 1980;71:27.
- [53] Uggowitzer P, Stüwe HP. *Mater Sci Eng* 1982;55:181.
- [54] Kim NJ, Thomas G. *Metall Trans A* 1981;12:483.
- [55] Waterschoot T, Verbeke K, De Cooman BC. *ISIJ Int* 2006;46:138.
- [56] Speich GR, Miller AB. In: Kot RA, Bramfitt BL, editors. *Fundamentals of dual-phase steels*. New York: The Metallurgical Society of AIME; 1981. p. 279.
- [57] Tanaka T, Nishida M, Hashiguchi K, Kato T. In: Kot RA, Morris JW, editors. *Structure and properties of dual-phase steels*. New York: The Metallurgical Society of AIME; 1979. p. 221.
- [58] Nakaoka K, Hosoya Y, Ohmura M, Nishimoto A. In: Kot RA, Morris JW, editors. *Structure and properties of dual-phase steels*. New York: The Metallurgical Society of AIME; 1979. p. 330.
- [59] Davies RG. *Metall Trans A* 1979;10:1549.
- [60] Koo JY, Thomas G. In: Davenport AD, editor. *Formable HSLA and dual-phase steels*. New York: The Metallurgical Society of AIME; 1979. p. 40.
- [61] Mazinani M, Poole WJ. *Metall Mater Trans A* 2007;38A:328.

Nanoprecipitate-hardened 1.5 GPa steels with unexpected high ductility

D. Raabe,* D. Ponge, O. Dmitrieva and B. Sander

Max-Planck-Institut für Eisenforschung, Max-Planck-Str. 1, 40237 Düsseldorf, Germany

Received 27 January 2009; revised 28 February 2009; accepted 28 February 2009

Available online 9 March 2009

We present mechanical and microstructure results on precipitation-hardened ductile high-strength martensitic and austenitic–martensitic steels (up to 1.5 GPa strength) with good ductility. The alloys have a low-carbon content (0.01 wt.% C), 9–12 wt.% Mn, and minor additions of Ni, Ti and Mo (1–2 wt.%). Hardening is based on transformation-induced plasticity and the formation of intermetallic nanoprecipitates in the martensite during heat treatment (aging). The approach leads to an unexpected simultaneous increase in both strength and total elongation.

© 2009 Acta Materialia Inc. Published by Elsevier Ltd. All rights reserved.

Keywords: Steel; High strength; Aging; Precipitation; Intermetallic

Steels with very high strength above 1 GPa and good ductility (total elongation of 15–20% in tensile testing) are future key materials for lightweight engineering solutions and corresponding CO₂ savings [1–5] (Fig. 1).

We present surprising results on low-alloyed materials that were developed by combining the transformation-induced plasticity (TRIP) effect with the martensite aging (maraging) effect. The TRIP mechanism exploits the deformation-stimulated transformation of unstable austenite into martensite and the resulting plasticity required to accommodate the transformation misfit [3–10]. The maraging effect uses the hardening of the heavily strained martensite through the formation of nanosized intermetallic precipitates. These precipitations act as highly efficient obstacles to dislocation motion thereby enhancing the strength of the material [11–16].

While both types of alloys, i.e. TRIP steels [3–10] and maraging steels [11–16], have been investigated in some depth, the combination of the two mechanisms has not yet received much attention.

The combination of the TRIP and maraging concepts in one alloy is alone sufficient to justify a detailed study as it promises an approach to enhance the strength of conventional steels without the use of large quantities of expensive alloying elements. Unfortunately, the downside of this approach is that the increase in strength is usually accompanied by a drop in ductility

(quantified here in terms of the total elongation) (Fig. 1). However, surprisingly, the opposite trend is observed in the present case: we observed the simultaneous increase in strength and ductility upon formation of nanoscaled precipitates.

The materials studied combine different hardening mechanisms. The first one is the formation of strain-induced martensite (alloys with 0.01 wt.% C and 12 wt.% Mn have retained austenite fractions up to 15 vol.%) and exploits the same hardening principles as TRIP steels [3–10]. The second one is the strain hardening of the ductile low carbon α' - and ϵ -martensite and of the remaining retained austenite. The third one is the formation of nanosized intermetallic precipitates in the martensite during heat treatment (i.e. maraging). These precipitates are highly dispersed owing to the favorable nucleation conditions in the heavily strained martensite matrix in which they form.

The steels show not only excellent mechanical properties but also an unexpected relationship between strength and total elongation as both quantities increase upon aging. In addition to the optimization of yield strength, ultimate tensile strength and elongation to fracture, we also are trying to make a material that is characterized by homogeneous strain hardening.

Here we report results for a 9 wt.% Mn and a 12 wt.% Mn alloy (9Mn: 8.86 wt.% Mn, 0.0065 wt.% C, 2.0 wt.% Ni, 1.07 wt.% Mo, 1.04 wt.% Ti, 0.047 wt.% Si, 0.086 wt.% Al; 12Mn: 11.9 wt.% Mn, 0.0101 wt.% C, 2.06 wt.% Ni, 1.12 wt.% Mo, 1.09 wt.% Ti, 0.057 wt.% Si, 0.116 wt.% Al). Both alloys have a very low-carbon

* Corresponding author. Tel.: +49 211 6792 340; fax: +49 211 6792 279; e-mail: d.raabe@mpie.de

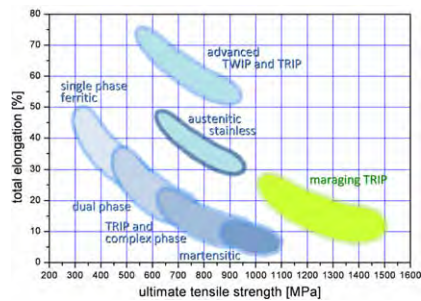


Figure 1. Typical strength–ductility profiles of steels. The data represent regimes such as published in the references given below. TRIP: transformation-induced plasticity; TWIP: twinning-induced plasticity; maraging TRIP: steel concept which uses hardening mechanisms based on transformation-induced plasticity and the formation of intermetallic nanoprecipitates in the martensite during heat treatment (aging).

content and minor additions of Ni, Ti and Mo which are required to form the nanoprecipitates. The difference among the samples consists in their Mn content (~9 wt.%, ~12 wt.%), and hence in the amount of retained austenite.

The alloys were melted and cast to round billets of 1 kg in a vacuum induction furnace. Annealing and swaging was conducted to ensure homogenization and removal of segregation. After annealing at 1150 °C for 1 h, swaging was conducted in eight passes between 1000 and 1150 °C (true strain of 1.39). This was followed by air cooling to 800 °C and a water quench to room temperature. The rods were reheated to 1100 °C for 0.5 h, hot rolled in six passes (true strain of 1.9) and water quenched. These strips were cold rolled to a thickness of 1.5 mm (true strain of 1). The subsequent solution heat treatment was performed at 1050 °C for 0.5 h followed by water quench. Final aging was conducted at different temperatures between 425 and 500 °C at times between 1 min and 48 h. Tensile testing was conducted on a Zwick ZH 100 using strain gage extensometer at a constant cross-head velocity corresponding to an initial strain rate of $8 \times 10^{-4} \text{ s}^{-1}$.

Characterization was conducted using optical and scanning electron microscopy (SEM) in conjunction with energy-dispersive X-ray spectrometry (EDX) and high-resolution electron back scatter diffraction (EBSD). SEM was performed using a JEOL JSM-6500F field emission scanning electron microscope operated at 15 kV. The EBSD scans were carried out in areas of about $100 \times 270 \mu\text{m}^2$ in cross-sections in the middle of the samples at a step size of 500 nm.

Transmission electron microscopy (TEM) images were taken of a solution-treated, quenched plus finally age-hardened sample with 12 wt.% Mn in order to study the size and spatial distribution of the nanoprecipitates which are formed during aging. For TEM sample preparation the material was first thinned to a thickness below 100 μm by mechanical polishing. Standard 3 mm TEM discs were then punched and electropolished into TEM thin foils using a Struers Tenupol twin-jet electropolishing device. The electrolyte consisted of 5% perchloric acid (HClO_4) in 95% ethanol cooled to $-30 \text{ }^\circ\text{C}$. The thinned specimens were investigated in a JEOL

JEM 2200 FS field emission transmission electron microscope operated at 200 kV. The analysis was carried out in scanning TEM mode (STEM) using a bright-field (BF) detector (BF-STEM).

Figure 2a shows the engineering stress–strain curves of the age-hardenable Mn steel with 9 wt.% Mn. The EBSD analysis reveals coarse α' -martensite lamellae of up to 100 μm in length, but no retained austenite appears in the solution-annealed and quenched state. This means that it is not an age-hardenable TRIP steel but a Mn-based maraging steel. Its yield strength (YS) is about 350 MPa, its ultimate tensile strength (UTS) about 810 MPa, and the total elongation (TE) about 6% in the as-quenched state. The properties of the same material after heat treatment (48 h at 450 °C) are surprising. The UTS is above 1 GPa while the TE does not drop upon precipitation strengthening as observed for conventional Ni–Co-based maraging steels [11–15] but it increases from 6% to more than 15%. This means that aging in this martensitic alloy simultaneously increases both strength and ductility. 15% pre-deformation (by cold rolling) of the same sample prior to the same aging procedure (Fig. 2a) yields similar properties as without pre-deformation. This result is plausible as the material did not contain instable austenite, hence no TRIP effect occurs.

A similar observation is made for the 12 wt.% Mn alloy (Fig. 2b). This sample has also an α' -martensite matrix but it contains up to 15 vol.% retained austenite and some ϵ -martensite. Hence, the 12 wt.% Mn alloy represents an age-hardenable TRIP steel (we refer to it as a maraging TRIP steel) as it can undergo hardening via deformation-induced martensite formation and via martensite hardening through precipitates.

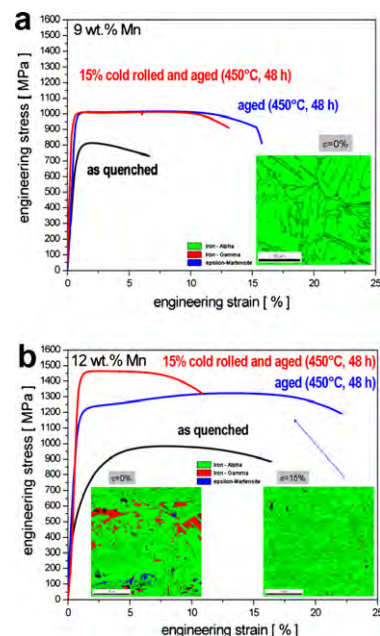


Figure 2. Stress–strain curves for the two Fe–Mn alloys. The 9 wt.% Mn alloy (a) has no retained austenite. The 12 wt.% Mn alloy (b) has up to 15 vol.% retained austenite prior to deformation which is gradually reduced during straining. Both alloys show the unexpected effect that the ultimate tensile strength and the total elongation simultaneously increase upon aging heat treatment (450 °C, 48 h).

The EBSD map shows a finer α' -martensite microstructure than in the 9 wt.% Mn sample. Dilatometry (measurement of thermal expansion) and ferromagnetic data suggest in part a higher austenite fraction of up to 20 vol.%. The differences between dilatometry, ferromagnetic characterization and EBSD can be attributed to the limited statistics provided by EBSD. Also EBSD yields surface information only. The size of the retained austenite islands lies between 1 and 20 μm . The ε -martensite lamellae are below 2 μm and occupy an overall fraction of about 1–2 vol.%.

The sample has a YS of about 325 MPa, UTS of nearly 1 GPa, and TE of about 16% in the as-quenched state. After aging heat treatment (450 °C for 48 h) the UTS increases to more than 1.3 GPa and the TE to 21%. 15% cold rolling prior to aging leads to a strong increase in strength (nearly 1.5 GPa UTS) but also to a drop in TE (about 10%). The increase in strength is attributed to the deformation-stimulated transformation of the retained austenite leading to a TRIP effect and, to a lesser extent, to the assumed higher dispersion of the precipitates formed under improved nucleation conditions in the deformation-induced martensite. The motivation for attributing the additional strain-hardening capacity of the 12 wt.% Mn alloy not only to the precipitates but also to the occurrence of the TRIP effect becomes clear when considering the following observations.

First, comparison of the flow curve of the 9 wt.% Mn sample with that of the 12 wt.% Mn sample for the 15 wt.% pre-rolled state reveals that the 12 wt.% Mn sample (containing retained austenite) shows a strong increase in strength while the 9 wt.% sample (no retained austenite) does not reveal any change in strength upon 15% cold rolling prior to testing (Fig. 2a and b). Second, an additional EBSD analysis conducted after 15% straining for the 12 wt.% Mn sample (EBSD phase map in Fig. 2b) shows that the retained austenite has vanished. This result was confirmed by magnetic measurements. Third, we measured the martensite start temperature for both alloys by dilatometry and also calculated it using the empirical equation of Hossein Nedjad et al. [17]. The dilatometry experiment showed a martensite start temperature of $T_{Ms} = 294$ °C for the 9 wt.% Mn alloy (150 °C according to the equation [17]) and of $T_{Ms} = 70$ °C for the 12 wt.% Mn alloy (25 °C according to the equation [17]).

Regarding the ductility, it is remarkable that both steels show, irrespective of their retained austenite content, the surprising feature of a simultaneous increase in both UTS and total elongation upon aging. While the UTS increases by 25–30% the total elongation increases by more than 150% (from 6% to 15%) for the 9 wt.% Mn sample and by 31% (from 16% to 21%) for the 12 wt.% Mn alloy. This increase of both properties represents a very unusual feature of these materials.

The BF-STEM micrographs that were taken of the age-hardened TRIP steel (12 wt.% Mn) show that the nanoscaled precipitates have a narrow size distribution with an average diameter of 8–12 nm (Fig. 3a–c). Local EDX analysis conducted in convergent beam mode shows an increased content in Ni, Ti and Al in these precipitates when compared to the surrounding matrix. This observation raised the possibility that these small

precipitates might be γ' phase, $\text{Ni}_3(\text{Ti,Al})$ according to results on Ni–Co-based maraging steels alloyed with Ti and Mo [12,13,18]. The area density of the nanoprecipitates was about $300 \mu\text{m}^{-2}$. The volume density is estimated as $5 \times 10^3 \mu\text{m}^{-3}$ (about 2–3 vol.%). Slightly elongated nanoprecipitates are located at the interfaces between the lamellae. These precipitates are about twice as long as those inside the grains (Fig. 3b). Besides these tiny precipitates, larger ones were also observed in the 12 wt.% Mn sample. They had an average size of 1–2 μm . EDX revealed that these precipitates contained Ti, Mo, C and Al.

The TEM data hence reveal that the steels, like conventional maraging steels, contain nanosized precipitates that are very highly dispersed, even after long heat treatments. The observation of a high maintained strength and a strong tendency for the nanoscaled precipitates not to coarsen has been reported previously for conventional maraging steels [14]. Using an Orowan line tension approximation for dislocation bow-out between the nanoprecipitates (10 nm diameter) and an average precipitate spacing of about 100 nm suggests an increase in yield strength upon aging of about 350 MPa. This increase in strength roughly matches the change in yield strength observed.

In addition to the nanoprecipitates, the dislocation content in the martensite matrix is also important for the strength. For example, Figure 3c shows that the dislocation density in the martensite was about 10^{15} – 10^{16}m^{-2} . It is noteworthy that the dense dislocation arrangement prevailed even after the aging treatment. The dislocation density could also play an important role in the nucleation of the precipitates and their very high dispersion. Figure 3c shows that many precipitates are located at dislocations. It is also important for the plastic properties that the (nearly) carbon-free martensite matrix is rather ductile.

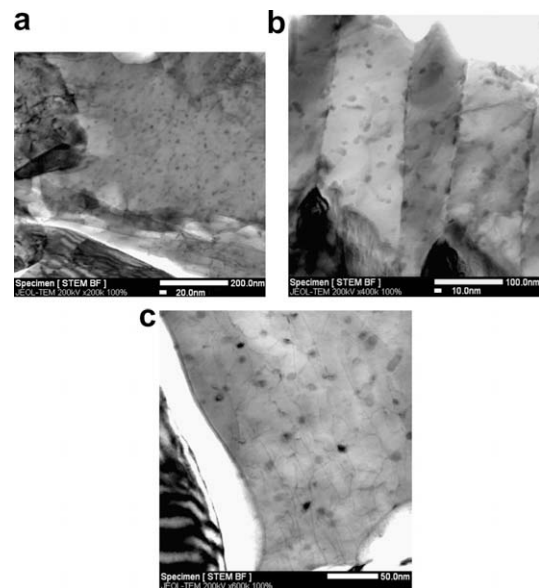


Figure 3. TEM images of nanoprecipitates formed in the aged 12 wt.% Mn alloy (500 °C, 2 h). The precipitates have an average diameter of 8–12 nm. Local EDX analysis shows an increased content in Ni, Ti and Al in the precipitates relative to the matrix. We speculate that they might be γ' phase precipitates, $\text{Ni}_3(\text{Ti,Al})$.

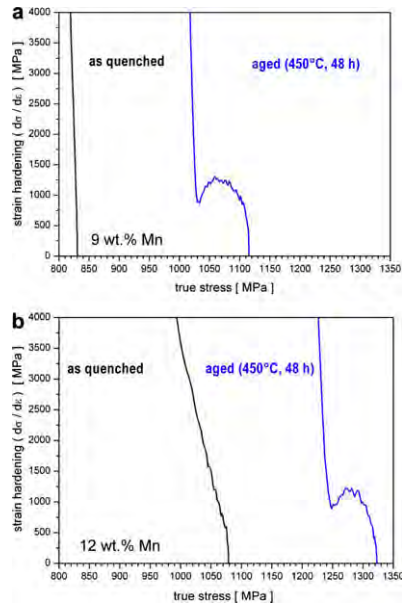


Figure 4. Kocks–Mecking analysis (strain hardening vs. stress curve) of the two alloys. Aging leads to a second hardening level at large stresses which does not appear in the as-quenched specimens. We interpret this effect in terms of Orowan hardening.

tile. Conventional carbon-based martensitic steels typically reveal very poor ductility (Fig. 1).

A central point of the current observations is the unexpected strong increase in the total elongation after aging (Fig. 2). Two effects are conceivable to explain this phenomenon: first, the kinetics associated with delayed austenitization; and second, the kinetics of precipitation.

Regarding austenitization, it has been observed in conventional maraging steels that the heating rate and the holding times both influence the kinetics of retransformation from martensite to austenite [19]. In other words it is conceivable that very long heat treatment times (450 °C, 48 h) entail delayed austenitization. Dilatometry studies at different heating rates confirm this phenomenon. Our data show the first deviation in length expansion from martensite upon reheating at a temperature of about 550 °C for the 12 wt.% Mn sample when using a quite rapid heating rate of 0.86 K s⁻¹. The same experiment conducted at a heating rate of 0.086 K s⁻¹ revealed a lower transformation point from martensite into austenite at around 500 °C. Thermodynamic predictions also suggest a transformation around 480 °C although some of the data underlying such simulations for Mn-containing Fe-based multicomponent systems are not considered as very reliable.

These findings initially seem to indicate that partial retransformation into austenite might play a role in the observed ductilization, at least for the specimen with 12 wt.% Mn. On the other hand, the alloy with only 9 wt.% Mn shows the same ductilization effect although retransformation at 450 °C is thermodynamically most unlikely for this alloy owing to its low austenite-stabilizing Mn content (Fig. 2b).

A more plausible explanation for the ductilization effect can be seen in the Orowan hardening mechanism

that starts to set in at a stress of about 1030 MPa (Fig. 4). The Kocks–Mecking analysis (strain hardening vs. stress curve) shows that this hardening effect is not active at the beginning of the tensile test. The second hardening plateau can also not be attributed to the TRIP effect as this mechanism occurs in both the 9 and 12 wt.% Mn samples after heat treatment.

In addition, the Kocks–Mecking curves for the as-quenched samples (not heat treated, hence no aging) (Fig. 4) do not show a second hardening plateau. A corresponding analysis on conventional Ni–Co-based maraging steel does not show this effect either. This means that the second hardening plateau can be attributed to Orowan hardening. The reason that this mechanism does not occur at the beginning of straining is attributed to the fact that the inter-precipitate spacing is so small (~100 nm) that a higher stress level must be reached before Orowan loops can become active (Fig. 3).

In summary, we present two new Fe–Mn steels with a low-carbon martensitic matrix and elements for the formation of precipitates (Ni, Ti, Al, Mo). One alloy had up to 15 vol.% of retained austenite (12 wt.% Mn, maraging TRIP steel), while the other had no retained austenite after quenching (9 wt.% Mn, maraging steel). Both materials revealed a significant increase in both strength and total elongation after aging heat treatment. The unexpected increase in elongation was attributed to the formation of nanoscaled precipitates leading to an Orowan hardening mechanism at intermediate strains.

- [1] J. Inoue, S. Nambu, Y. Ishimoto, T. Koseki, *Scripta Mater.* 59 (2008) 1055.
- [2] S. Nambu, M. Michiuchi, Y. Ishimoto, K. Asakura, J. Inoue, T. Koseki, *Scripta Mater.* 59 (2008) 1055.
- [3] J.R. Patel, M. Cohen, *Acta Metall.* 1 (1953) 531.
- [4] H.K.D.H. Bhadeshia, D.V. Edmonds, *Metall. Trans.* 10A (1979) 895.
- [5] M. Takahashi, H.K.D.H. Bhadeshia, *Mater. Trans. JIM* 32 (1991) 689–696.
- [6] P.J. Jacques, E. Girault, T. Catlin, N. Geerlofs, T. Kop, S. van der Zwaag, F. Delannay, *Mater. Sci. Eng. A* 273–275 (1999) 475.
- [7] M. De Meyer, D. Vanderschueren, B.C. De Cooman, *ISIJ. Int.* 39 (1999) 813.
- [8] S. Traint, A. Pichler, K. Hauzenberger, P. Stiaszny, E. Werner, *Steel Res. Int.* 73 (2002) 259.
- [9] P.J. Jacques, *Curr. Opin. Solid State Mater. Sc.* 8 (2004) 59.
- [10] S. Zaeferrer, J. Ohlert, W. Bleck, *Acta Mater.* 52 (2004) 2765.
- [11] R.F. Decker, J.T. Eash, A.J. Goldman, *Trans. ASM* 55 (1962) 58.
- [12] R.F. Decker (Ed.), *Source Book on Maraging Steels*, ASM International, Metals Park, OH, 1979.
- [13] W. Sha, A. Cerezo, G.D.W. Smith, *Metall. Trans.* 24A (1993) 1251.
- [14] V.K. Vasudervan, S.J. Kim, C.M. Wayman, *Metall. Trans.* 21A (1990) 2655.
- [15] C. Servant, N. Bouzid, *Acta Metall.* 36 (1988) 2771.
- [16] R. Tewari, S. Majumder, I.S. Batra, G.K. Dey, S. Banerjee, *Acta Mater.* 48 (2000) 1187.
- [17] S. Hossein Nedjad, M.R. Movaghar Garabagh, M. Nili Ahmadabadi, H. Shirazi, *Mater. Sci. Eng. A* 473 (2008) 249.
- [18] G.P. Miller, W.I. Mitchell, *J. Iron Steel Inst.* 20 (1965) 899.
- [19] R. Kapoor, I.S. Batra, *Mater. Sci. Eng. A* 371 (2004) 324.